

Novel Methods for Automatic Analysis on Vascular Images

Yuchun Ding

Thesis submitted to the University of Nottingham
for the degree of Doctor of Philosophy

April 2016

Abstract

Imaging has become an essential component in many fields of medical and clinical research. The availability of medical imaging provides an excellent opportunity for monitoring and diagnosis of diseases. Automatic analysis of medical images can help with these processes. To date, automatic medical image analysis is still a difficult job in the field of computer vision because of factors such as noise and intensity inhomogeneity, which affect the performance of an image analysis framework.

There are many types of medical images available and the analysis of each of these image types requires its own specially designed methods. Blood vessels are implicated in a large number of diseases, including diabetic retinopathy, cardiovascular diseases, and Alzheimer's disease, which cause damage to blood vessels. Because of this, blood vessel analysis is of great importance in medical diagnostic applications. In addition, a type of glial cell called the microglia have the similar appearance to blood vessels, but have a damaging role in a range of brain disorders. Previous research has found that the development of blood vessels and the presence of microglia are strongly correlated. Thus, the analysis of microglial images can also help provide a valuable tool to gain insight into the biology of blood vessels in health and disease.

The primary objective of this Ph.D. thesis is to develop an automatic and reliable image analysis framework for analysing microvasculature data. A typical medical image analysis framework often includes several steps before diagnosing the disease of a patient. Firstly, the representation of an image is typically converted into a form that is easier to analyse, in a process known as segmentation.

Traditional vessel segmentation methods often fail for images that contain high–density microvessels and background noise. The errors occur in the form of missing, undesired broken or incorrectly merged vessels, eventually leading to poor segmentation results. A method for both 2D and 3D vessel segmentation that is suitable for segmenting microvessels has therefore been proposed here. The method incorporates the advantages of a line filter and a Hessian–based vessel filter to enhance vessels, and this has shown to be reliable for noisy and inhomogeneous images. For evaluating the proposed method, three synthetic vessel-like models were created, each with different structural properties that are characteristic of the true vasculature, and varies levels of Gaussian noise were applied to these images to simulate noise present in real MRI data. Experimental results have shown that the proposed method produces good vessel segmentation on synthetic vessel images, with significant ability to deal with high noise levels. For example, the method produced 94.46%, 95.29% and 92.48% of segmentation accuracies on branch, spiral and column models with -80dB noise. In comparison, the line filter and Hessian–based filter failed to provide valid segmentation. Furthermore, the method has been applied to three real brain datasets: Micro-CT rat, monkey and MRI human brains. Since there is no ground truth available for the brain models to obtain quantitative analysis, selected results using the line filter, Hessian–based vessel filter, and the proposed method are compared, to demonstrate the strength of the proposed method. As shown by the testing, the proposed method performed very well and handled the noise better.

After segmentation, essential information can be extracted from the segmented structure for classification. This is known as feature extraction. Traditional vessel analysis methods, such as counting the number of branches or measuring the curvature and diameter of individual vessel, are unsuitable for the analysing

microvasculature. Previous research used fractal analysis for calculating fractal dimensions of blood vessels, but at present, there has been no systematic research extracting discriminant features from the structure for classification. A novel quantitative analysis method, based on multifractal analysis, is performed on the segmented structures and support vector machine for classifying the structure based on their multifractal features is then introduced. Three publicly available retinal vascular image databases (STARE, MESSIDOR, DIARETDB) are used for the experiments. The proposed methods have produced accuracies of 85.5%, 77% and 81.2% for classification of healthy and diabetic retinal vasculatures on each of the datasets respectively. Experiments show that classification with multiple fractal features produces better rates compared with methods using a single fractal dimension value. Also, experiments demonstrate that classification accuracy can be affected by the accuracy of vessel segmentation algorithms.

The use of multifractal analysis for feature extraction can also be applied to analysing microglia morphology and for classification of microglial activation states. However, there is little prior research on the segmentation of microglial images. Common image segmentation methods are not suitable for the microglial histology images used, so an automated method capable of accurately and efficiently segmenting the microglia from histology images is introduced. The method includes the use of the fast split Bregman algorithm for image denoising and segmentation. A set of selected images were used for validation of the proposed automated technique against manual analysis. Experiments show that the proposed segmentation method has produced similar results to those obtained by the manual method, the method also overcomes the common problems that were described in previous research due to the inhomogeneity of the images. The classification method is then applied to a selected microglial cells dataset, and

have produced accuracies of 94.27% for classifying microglial cells in four different activation states. Results have shown that the method is scalable for analysing large microglia datasets.

List of Publications

Some parts of the work presented in the thesis have been published in the following articles:

0.1 Journal Papers

- Y. Ding, W. Ward, W. T, P. Gowland, A. Peters, J. Yang, and L. Bai, "Three-dimensional vessel segmentation using a novel combinatory filter framework," *Physics in Medicine and Biology*, 2014

- Y. Ding, W. Ward, J. Duan, D. Auer, P. Gowland, and L. Bai, "Retinal vasculature classification using novel multifractal features," *Physics in Medicine and Biology*, 2015

- M.-C. Pardon, M. Y. Lopez, D. Yuchun, M. Marjańska, M. Prior, C. Brignell, S. Parhizkar, A. Agostini, L. Bai, D. P. Auer, *et al.*, "Magnetic resonance spectroscopy discriminates the response to microglial stimulation of wild type and alzheimers disease models," *Scientific reports*, vol. 6, 2016

- Y. Ding, H. Faas, M. C. Pardon, W. O. Ward, J. Duan, F. Easton, D. Auer, and L. Bai, "A novel framework for microglia extraction, morphological analysis and classification," *Transactions on Computational Biology and Bioinformatics*, Under Revision

0.2 Conference Papers

- Y. Ding and L. Bai, "Experimental comparison of vasculature segmentation methods," in *9th International Conference on Computer Vision Theory and Applications*, pp. 425–432, 2014

- Y. Ding, W. O. C. Ward, T. Parker, S. Nakagawa, L. Buttery, L. White, and L. Bai, "Segmentation of mouse brain microvasculature from Micro-CT images using Gabor filter and local entropy thresholding," in *11th International Conference on Quantification of Brain Function with PET*, p. 136, 2013

- W. O. Ward, Y. Ding, and L. Bai, "Analysis of three-dimensional vasculature using multifractal theory," in *Computational Intelligence in Healthcare and e-health (CICARE), 2014 IEEE Symposium on*, pp. 64–68, IEEE, 2014

- J. Duan, Y. Ding, Z. Pan, J. Yang, and L. Bai, "Second order Mumford-Shah model for image denoising," in *International Conference on Image Processing*, 2015

- A. Agostini, Y. Ding, L. Bai, and M. C. Pardon, "Unaltered susceptibility to neuroinflammation in pre-symptomatic appswe/ps1e9 mice, focus on genotype and sex differences," in *Meeting of the British Association for Psychopharmacology*, 2015

Acknowledgements

I would like to thank my supervisor, Dr Bai Li, for her valuable suggestions, encouragement and help through the whole course of my research.

I would like to thank the late Terry Parker and S. Nakagawa in Biomedical Sciences; Lee Buttery and Lisa White in Biomolecular Sciences, Henryk Faas, Marie-Christine Pardon, and Alessandra Agostini in Medicine & Health Sciences, at the University of Nottingham, UK for providing the 3D images and the histology images.

I would like to thank my colleagues for their time and support, especially to Wil Ward and Jinming Duan who kindly provided the implementation code for multifractal analysis and Mumford-Shah total variation.

Finally, I would like to express my deepest gratitude to my parents and to my wife who are always there to support me unconditionally.

Contents

0.1 Journal Papers vi

0.2 Conference Papers vii

1 Introduction **1**

1.1 Blood Vessel 2

1.1.1 Motivation and Objective 2

1.1.2 Challenge 2

1.2 Microglia Histology 5

1.2.1 Motivation and Objective 5

1.2.2 Challenge 7

1.3 Major Contributions of the Thesis 8

1.4 Organisation of the Thesis 10

2 Literature Review **12**

2.1 Segmentation 13

2.1.1 Local Entropy Thresholding 14

2.1.2 Multiscale Vesselness Filter 16

2.1.3 Wavelet Transform Modulus Maxima (WTMM) 21

2.1.4 Level Set Methods 23

2.2 Feature Extraction 26

2.2.1 Multifractal Feature Extraction 27
2.2.2 Wavelet Scale Spectra Feature Extraction 28
2.3 Classification 30
2.3.1 Support Vector Machine 31
2.3.2 Cosine Similarity Metric Learning 33

3 Introducing the Proposed Methods 36
3.1 Combinatory Vessel Segmentation Method 37
3.1.1 Methodology 37
3.2 Microglial Segmentation Method 41
3.2.1 Methodology 41
3.2.1.1 Mumford-Shah Total Variation 42
3.3 Fractal Feature Extraction Method 45
3.3.1 Methodology 45
3.4 Summary 49

4 Case Study 1: 3D Vascular Data 50
4.1 Data Acquisition 52
4.2 Segmentation 53
4.2.1 Vessel Scale 55
4.3 Validation with Synthetic Vascular Data 61
4.3.1 Measures of Success 62
4.3.2 Parameters 67
4.4 Fractal Feature Extraction 72
4.5 Summary 74

5 Case Study 2: 2D Retinal Data 75

5.1 Data Acquisition 77
5.1.1 DRIVE 77
5.1.2 STARE 77
5.1.3 MESSIDOR 78
5.1.4 DIARETDB 78
5.2 Segmentation with Retinal Vascular Data 79
5.2.1 Experimental Segmentation Results 79
5.2.1.1 Local Entropy Thresholding 80
5.2.1.2 Multiscale Vesselness Filter 83
5.2.1.3 Wavelet Transform Modulus Maxima (WTMM) . 86
5.2.1.4 Level Set Methods 87
5.2.1.5 Summary of the Results 90
5.2.2 Improving An Existing Retinal Analysis Software 93
5.2.2.1 Original ARIA 95
5.2.2.2 The Improved ARIA Software 97
5.3 Classification with Retinal Vascular Data 99
5.3.1 Validation 100
5.3.1.1 Retinal Databases 100
5.3.1.2 Feature Extraction 100
5.3.1.3 Classification 107
5.3.2 Diabetic Retinopathy Classification 113
5.4 Summary 118

6 Case Study 3: Microglial Histology Data **119**

6.1 Data Acquisition 121
6.2 Segmentation 123

6.2.1 Workflow 123
6.2.2 Validation 124
6.3 Microglia Activation States Analysis 130
6.4 Summary 136

7 Summary and Future Work **140**
7.1 Summary of Contributions 141
7.1.1 Improved Vessel Segmentation Method 141
7.1.2 Novel Fractal Feature Classification Method 141
7.1.3 Automatic Microglia Analysis Framework 141
7.2 Future Works 143
7.2.1 Vascular Analysis on Large Databases 143
7.2.2 Microglia Activation States Classification 143

8 Method Implementation Code **146**
8.1 Local Entropy Thresholding [17] 147
8.2 Gabor Filter [181] 149
8.3 Matched Filter [17] 150
8.4 Multiscale Vesselness Filter [19] 152
8.5 Wavelet Transform Modulus Maxima (WTMM) [91] 155
8.6 Level Set Basic 159
8.7 Line Filter [126] 161
8.8 Microglia Segmentation 162
8.8.1 Mumford-Shah Total Variation [8] 164
8.9 Fractal Feature Based Classification 167
8.9.1 Multifractal Spectrum [32] 170
8.9.2 Fourier Power Spectrum [182] 172

9 Appendix-Publications Preview **177**

List of Figures

1.1 Overview of the anterior cortex of a normal mouse and a diseased mouse (from [24]). 4

1.2 Microglial morphology in adult human CNS (from [47]). 6

2.1 Quadrants of co-occurrence matrix. 15

2.2 Possible models of the (a,d) plate-like, (b,e) tube-like and (c,f) sphere-like objects, the pattern can be known by comparing the value of the eigenvalues λ_1, λ_2 and λ_3 (from [80]). 18

2.3 Zoomed-in vesselness image. 20

2.4 Decomposition to the second level. L: Low frequency. H: High frequency. 29

2.5 SVM concept. 32

2.6 Nonlinear SVM concept (a) original data (b) rearranged data. . . 32

3.1 The directional mask used for the proposed method. An average intensity value of points within $7 \times 7 \times 7$ windows is computed. Average intensity values of all points passing through the centre point in 133 directions are compared and the maximal value is kept. Angular resolution is 15°. 39

3.2 Multifractal analysis of 20 healthy and 20 pathological (background diabetic retinopathy) retinal vasculatures from STARE: (a) $\alpha/f(\alpha)$ spectra of vasculatures automatically segmented by the combinatory vessel filter; (b) Fourier power spectra of vasculature automatically segmented by the combinatory vessel filter. The extracted features are labelled on the plots. 47

4.1 Flowchart of case study 1. 51

4.2 3D rendered images of rat brain microvasculature obtained from imaging resin-cast models using micro-CT scanner segmented with the proposed method. Samples are named (a) C2, (b) F2, (c) L0, and (d) J2. 54

4.3 3D rendered images of monkey brain microvasculature obtained from imaging resin-cast models using a micro-CT scanner segmented with the proposed method. 55

4.4 3D rendered images of human in-vivo brain vasculature obtained through segmenting 7T MRI images with the proposed method. Samples are named: (a) Head 4, (b) Head 5, (c) Head 6, (d)Head 7, (e)Head 8, and (f) Head 9. 56

4.5 Screenshots taken along the x-axis from the segmentation of Head 4 using (a) the line filter, (b) the Hessian–based filter, and (c) the proposed method. 56

4.6 Selected cross-sections of segmentation of Head 4. (first column) The original image, (second column) the line filter, (third column) the Hessian–based filter, and (forth column) the proposed method. 57

4.7 Selected cross-sections of segmentation of Rat F2. (first column) The original image, (second column) the line filter, (third column) the Hessian–based filter, and (forth column) the proposed method. 58

4.8 Screenshots of segmentation of Rat F2 using (a) the line filter, (b) the Hessian–based filter, and (c) the proposed method. 59

4.9 Rat brain F2 vessel separation based on scale values in the proposed method. Each subplot shows vessels segmented using scales (a) $\{1, 3, 5, 9\}$, (b) $\{3, 5, 9\}$, (c) $\{3, 5\}$, and (d) a single scale $\{9\}$. . . . 59

4.10 Vessel thickness visualisation of the segmented rat brain F2 using different scales, corresponding to Figures 4.9(a)-(c), using Fiji plugin in ImageJ. The calibration bar (d) indicates the thickness of the vasculature where 24 is equivalent to 2.4mm based on the scanning resolution. 60

4.11 3D synthetic models created for experiments (a) branch (b) spiral (c) columns. 61

4.12 Plots of (a) sensitivity (b) specificity (c) Jaccard index (d) Cohen's kappa, for the different methods applied to each synthetic model for the full range of tested noise levels. 64

4.13 Segmentation results of the branch model, with -74dB Gaussian noise SNR, using (a) vessel filter (b) line filter, and (c) the proposed method. 65

4.14 Box plot comparison of three methods on each synthetic model. Top row: accuracy for (a) branch model, (b) spiral model, and (c) column model. Bottom row: RMSE for (d) branch model, (e) spiral model, and (f) column model. Black points represent values for models with SNR below -74dB 66

4.15 Top-down view of the spiral model, showing possible pattern detection depending on different size of α and β value. (a) $\beta = 0.01$ and $\alpha = 0.99$. (b) $\beta = 0.99$ and $\alpha = 0.01$ (c) $\beta = 0.5$, $\alpha = 0.5$. . . 68

4.16 ROC curve comparison of the three methods on each synthetic model with two different levels of added noise: SNR -66dB and -74dB. Green points correspond to tests for the proposed method, red for the vesselness filter, and blue for the line filter. Non-linear least squares fitted curves are added, with R^2 values given in legend along with calculated area under the curve. 70

4.17 Multifractal analysis of six human brain vasculature models and four rat brain microvasculature models. (a) multifractal $\mathcal{H}/f(\mathcal{H})$ spectra, (b) symmetry features of each spectrum. The dashed line represents the 1:1 ratio plot. 73

5.1 Flowchart of case study 2. 76

5.2 2D retinal fundus image from DRIVE. (a) original image (b) manual segmentation by an expert. 79

5.3 Result of LET without Gabor filter in 2D. 81

5.4 Result of LET with Gabor Filter in 2D. 82

5.5 Sensitivity/specificity values generated. The red dot represents the results produced using the Gabor filter with the most optimal parameters. 84

5.6 Result of the vesselness filter in 2D. 84

5.7 Result of the combinatory vessel filter in 2D. 85

5.8 Samples of vessel extraction with one scale (a) with and (b) without applying discrete wavelet transform. 86

5.9 Result of WTMM in 2D. 87

5.10 Leaking problem with level set. 88

5.11 Result of phase-based level set. 89

5.12 Result of phase-based level set on matched filtered image. 90

5.13 (a) Original retinal image, where vessel and pathologies are labelled in black and blue respectively. (b) Image after being matched filtered. 91

5.14 (a) Original retinal fundus image, (b) segmented retinal vasculature, (c) centreline of segmented retinal vasculature, (d) highlighted vessel branching point, (d) vasculature skeleton after removing branch points and small vessels, (e) length of a selected vessel branch. . . 94

5.15 (a) Original ARIA interface, (b) improved ARIA interface. 96

5.16 Measuring vessel branch angle. 97

5.17 (a) Select vessel to delete, (b) vessels after deleting. 98

5.18 Example vessel segmentation on images from STARE. (a)-(e) are retinal vascular images of a diabetic patient manually segmented by VK and AH, and automatically segmented using the Hessian–based vessel filter, the line filter, and the combinatory vessel filter respectively. (f)-(i) are retinal vascular images of a healthy patient manually segmented by VK and AH, and automatically segmented by the Hessian–based vessel filter, the line filter, and the combinatory vessel filter respectively. 101

5.19 Example vessel segmentation on images from MESSIDOR. (a)-(c) are retinal vascular images of a patient (macular edema) segmented by the Hessian–based vessel filter, the line filter, and the combinatory vessel filter respectively, (d)-(f) are retinal vascular images of a healthy patient segmented by the Hessian–based vessel filter, the line filter, and the combinatory vessel filter respectively. 102

5.20 Multifractal analysis of a retinal vascular image from STARE manually segmented by VK: (a) multifractal $\alpha/f(\alpha)$ spectra, (b) the vascular image rotated in eight directions. 102

5.21 Multifractal analysis of 20 healthy and 20 pathological (background diabetic retinopathy) retinal vasculatures from STARE: (a)-(c) $\alpha/f(\alpha)$ spectra of vasculatures automatically segmented by the Hessian–based vessel filter, the line filter, and the combinatory vessel filter respectively; (d)-(f) Fourier power spectra of vasculature automatically segmented by the Hessian–based vessel filter, the line filter, and the combinatory vessel filter respectively. 103

5.22 Multifractal analysis of 38 healthy and 38 pathological (muscular edema) retinal vasculature from MESSIDOR: (a)-(c) $\alpha/f(\alpha)$ spectra of vasculature automatically segmented by the Hessian–based vessel filter, the line filter, and the combinatory vessel filter respectively; (d)-(f) Fourier power spectra of vasculatures automatically segmented by Hessian–based vessel filter, the line filter, and the combinatory vessel filter respectively. 104

5.23 Multifractal analysis of 10 healthy and 10 pathological retinal vasculature from STARE: (a)-(c) $\alpha/f(\alpha)$ spectra of vasculature manually segmented by VK and AH, and automatically segmented by the combinatory vessel filter, respectively; (d)-(f) Fourier fractal spectra of vasculatures manually segmented by VK and AH, and automatically segmented by the combinatory vessel filter, respectively. 105

5.24 Multifractal analysis of 20 healthy, 20 pathological (background diabetic retinopathy) and 20 pathological (retinal vein occlusion, arteriosclerotic retinopathy, choroidal neovascularisation) retinal vasculatures from STARE: (a)-(c) $\alpha_0 - \alpha_{\min}/f_0$ plots of vasculatures automatically segmented by the Hessian–based vessel filter, the line filter, and the combinatory vessel filter respectively. 105

5.25 Features extracted from $\alpha/f(\alpha)$ spectra and Fourier power spectra of vasculatures automatically segmented by the combinatory vessel filter: (a) the peak of the multifractal spectrum (f_0); (b) the symmetry features $\alpha_0 - \alpha_{\min}$, and (c) $\alpha_{\max} - \alpha_0$, as well as the Fourier features (d) FFD and (e)-(g) FPS magnitude values at high frequencies. The dataset contains 20 healthy and 20 pathological (P1: background diabetic retinopathy) and another 20 pathological (P2: retinal vein occlusion, arteriosclerotic retinopathy, and choroidal neovascularisation) retinal vasculatures from STARE. 106

5.26 Features extracted from $\alpha/f(\alpha)$ spectra and Fourier power spectra of vasculatures automatically segmented by the combinatory vessel filter: (a) the peak of the multifractal spectrum (f_0), (b) the symmetry features $\alpha_0 - \alpha_{\min}$, and (c) $\alpha_{\max} - \alpha_0$, as well as the Fourier features (d) FFD and (e)- (g) FPS magnitude values at high frequencies. The dataset contains 38 healthy and 38 pathological (muscular edema) retinal vasculature from MESSIDOR. 107

5.27 ROC analysis with area under the curve (AUC) and box plots on the STARE dataset: SVM results using different features for classifying (a)(b) two classes and (c)(d) three classes respectively. The labels refer to the feature combinations in Table 5.3. 111

5.28 ROC analysis with area under the curve (AUC) and box plots on the MESSIDOR dataset: (a)(b) SVM results using different features for classifying two classes. Vasculature segmented by the combinatory vessel filter. (c)(d) SVM results using the combinatory features for classifying two classes. Vasculature segmented by the Hessian–based vessel filter, the line filter, and the combinatory vessel filter. The labels refer to the feature combinations in Table 5.4. 112

5.29 ROC analysis with area under the curve (AUC) and box plots on the STARE dataset segmented by the Hessian–based vessel filter, the line filter, and the combinatory vessel filter. SVM results using the combinatory features for classifying (a)(b) two classes and (c)(d) three classes respectively. 114

5.30 (a) ROC analysis with area under the curve (AUC) and (b) box plots on the STARE dataset manually segmented by VK and AH, and automatically segmented by the combinatory vessel filter, SVM classification results using the combinatory features for classifying two classes. 115

5.31 Example vessel segmentation on images from DIARETDB: (a) retinal image and (b) segmented vascular image of a diabetic patient; (c) retinal image and (d) vascular image of a healthy patient. . . . 116

5.32 Multifractal analysis of 20 healthy and 20 pathological (background diabetic retinopathy) retinal vasculatures from DIARETDB: (a) $\alpha/f(\alpha)$ spectra of vasculatures automatically segmented by the combinatory vessel filter respectively. (b) Fourier power spectra of vasculature automatically segmented by the combinatory vessel filter respectively. 117

6.1 Flowchart of case study 3. 120

6.2 (a) Identification of hippocampal subfields using the Franklin and Paxinos Altlas [177]. 122

6.3 (a) Cropped image, (b) smoothed image ($\alpha = 10$) (c) microglia processes, (d) smoothed image ($\alpha = 150$), (e) microglia soma, (f) combined microglia processes and soma, (g) full microglia, (h) skeleton of microglia. 123

6.4 (a) Cropped microglia image, (b) microglia segmentation using simple thresholding, (c) microglia segmentation using level set, (d) microglia segmentation using the proposed method. 124

6.5 (a) Microglia cluster image, (b) microglia skeleton, (c) microglia soma, (d) microglia skeleton and soma. 124

6.6 Workflow of the proposed segmentation for a sample image: (a) original histology image, (b) smoothed image ($\alpha = 10$), (c) smoothed image ($\alpha = 300$), (d) microglia soma segmentation, (e) microglia soma and processes segmentation, (f) automatically labelled microglia overlaid onto the histological image. 125

6.7 Challenges described in a previous study and overcome using the proposed method [49]: (a) image shows microglial cells with strong and weak intensities, (b) image has a large complex artefact with microglia located partly inside the artefact, (c) image shows two regions that exhibit different visual textures, (d) image displays a complex texture appearance that blurs the distinction between microglial cell and background pixels, (e)-(h) Microglia soma labelled using the proposed method. 126

6.8 Examples of soma area estimation, and estimation of the percentage of the area stained: (a) and (d) Iba-1 positive microglial cells in unprocessed images, (d) freehand delineation of microglial somas and annotation of the soma size calculated by NDP.viewer2 software, (c) soma segmentation by the proposed method, (e) example of manually adjusted threshold level for the estimation of the percentage of area stained by Iba-1, (f) example of automatic estimation of the percentage of area stained by Iba-1. 127

6.9 Comparison of segmentation results using the proposed segmentation method and the manual segmentation method: (a) Microglia soma segmented using the proposed automatic segmentation method; (b) Microglia soma manually segmented by the expert. Analysis results calculated using automatic and manual segmentation methods within the hippocampus; (c) Soma number; (d) Soma area. ***, p¡0.0001. Statistically significant differences between scorers and between some scorers and automated method; (e) Percent area stained. **, p¡0.01. ***, p¡0.0001. Statistically significant differences between scorers and between scorers and automated method. Automatic: results produced by the proposed method. Manual A and Manual B: results produced by the experts. 128

6.10 Artefacts that the proposed method incorrectly detected as microglia. 129

6.11 Multifractal spectra of microglia: (a) segmented microglia rotated in four different directions, (b) multifractal $\alpha/f(\alpha)$ spectra of the microglia, (c) segmented microglia at four common activation stages, (d) multifractal $\alpha/f(\alpha)$ spectra. 131

6.12 (a) Lacunarity plot, (b) Fourier power spectra in log-log scale of the microglia in Figure 6.11 at four common activation stages. . . 132

6.13 Multifractal analysis of microglia at four common activation stages: (a) multifractal $\alpha/f(\alpha)$ spectra, (b) Fourier power spectra in log-log scale, (c) lacunarity/box-size plot, (d) feature of the multifractal spectra in (a) $\alpha_0 - \alpha_{min}$ / $\alpha_{max} - \alpha_0$ /f_0, (e) feature of the multifractal spectra $\alpha_0 - \alpha_{min}$ / $\alpha_{max} - \alpha_0$, (f) feature of the spectra in (a) $\alpha_{max} - \alpha_0$ / f_0. The boundary curve (by SVM classifier) shows a clear difference between the four classes. 134

6.14 Segmentation result of a typical Alzheimer's mouse brain slice (a) the original histology data, the hippocampus being labelled with square boxes; (b)(c) zoomed in hippocampal regions. Microglia are labelled in four different colours. Cyan: activated, Green: slightly ramified, Red: partially ramified. Blue: fully ramified; (d) heat map of the microglial density image and the corresponding colour bar, representing the number of microglia within a square region. 138

6.15 Segmentation result of a typical healthy mouse brain slice: (a) the original histology data, the hippocampus being labelled with square boxes; (b)(c) zoomed in hippocampal regions. Microglia are labelled in four different colours. Cyan: activated, Green: slightly ramified, Red: partially ramified. Blue: fully ramified; (d) heat map of the microglial density image and the corresponding colourbar, representing the number of microglia within a square region. 139

7.1 Examples of morphological types of microglia: ramified (1), hypertrophied (2,7), bushy cells (3,6), and amoeboid (4,5). 144

7.2 Multifractal analysis of microglia at seven activation stages: (a) multifractal $\alpha/f(\alpha)$ spectra (b) feature of the multifractal spectra $\alpha_0 - \alpha_{min}$ / $\alpha_{max} - \alpha_0$ /f_0. The numbers correspond to the activation states in Figure 7.1. 145

List of Tables

2.1 Multiscale vesselness filter can detect plate-like, tube-like and sphere-like objects depending on the value of the eigenvalues λ_1, λ_2 and λ_3 (from[19]). 17

4.1 Branch model: accuracy and root-mean-square error values for the three tested methods. 67

4.2 Spiral model: accuracy and root-mean-square error values for the three tested methods. 68

4.3 Column model: accuracy and root-mean-square error values for the three tested methods. 69

5.1 Performance detail using 2D retinal vessel image, based on literature review in this thesis. 92

5.2 Performance detail using 2D retinal vessel image, based on previous literature review [93]. 92

5.3 Classification accuracy using different methods on the STARE dataset. The best result is highlighted in bold. Number 1-9 use vasculature segmented by the combinatory vessel filter. The last three rows use the manual and automatically segmented vasculature data. 109

5.4 Classification accuracy using different methods on the MESSIDOR dataset. The best result is highlighted in bold. Number 1-9 use vasculature segmented by the combinatory vessel filter. 109

6.1 Classification accuracy with SVM on different features. 135

Chapter 1

Introduction

The primary concern of this thesis is to develop a framework for automatically and reliably analysing microvasculature data. In addition, previous research has shown that microglial cells have the similar appearance to blood vessels; also, the development of blood vessels and the presence of microglia are strongly correlated. Therefore, the same technique for classifying vasculature can be used for classifying microglial cells, to gain insight into the relationship between blood vessels and microglial cells in the future. This chapter gives a brief introduction to the background to this research on both vessels and microglial cells. A summary of the main contributions of the thesis is given and the organisation of the thesis is introduced.

1.1 Blood Vessel

1.1.1 Motivation and Objective

Vascular pathology is present in many human diseases and so there has been intense research in the past on vessel imaging for diagnosis and treatment of vascular diseases [10]. In recent years, the role of vascular dysfunction has been implicated in neurological diseases, including Alzheimer's disease (AD) [11, 12]. A significant finding is that vascular abnormalities could potentially serve as an early imaging biomarker of the disease [13]. A sensible way to validate the theory linking the microvasculature to pathologies on large vascular datasets is to use automated computational methods [14].

The main weakness in vascular research is considered to be the lack of computational tools for quantification of the microvasculature. Traditional vessel analysis methods are unsuitable for analysing the microvasculature as they have mostly been developed for detecting and measuring large vessels for cardiovascular disease using magnetic resonance angiography (MRA) or computed tomography angiography (CTA) images, and these often involve the use of contrast agents [15, 16]. Therefore, the first objective is to develop an advanced framework for better microvasculature analysis. 3D Micro-CT/MRI brain data and 2D retinal data are selected for case studies as those types of data contain high–density microvessels and background noise.

1.1.2 Challenge

Although there are numbers of vessel segmentation methods available, for example, local entropy thresholding (LET) is a method that creates a co-occurrence matrix

to automatically estimate the threshold value based on the entropy of an image. The method works well for vascular images with a simple homogeneous background [17], but is not scale invariant and is unreliable on noisy or inhomogeneous images. An alternative multiscale edge detection algorithm, named as, wavelet transform modulus maxima (WTMM) can detect irregularities (edges) in reasonably noisy and inhomogeneous images [18]. The drawback of this method is that the edges found are often broken, and its performance can be susceptible to errors on significantly noisy images. A level set approach can produce connected components by tracing vessels from seed points. The method is, however, computationally expensive and often fails on images that contain faint and narrow vessels, causing the evolving level set to terminate early and leaving vessels undetected. The Hessian–based vessel filter segments vessels by obtaining a measure of 'vesselness'[19]. The method can produce significantly better segmentation results in terms of accuracy while retaining fast runtime. However, it is still sensitive to noise and does not perform well on images with complex backgrounds. Additionally, segmentation results often contain undesired broken vessels [20].

Another major challenge, is how to analyse the segmented microvasculature, linking its structure to pathology. Achieving automatic analysis of the microvasculature can assist in the implementation of screening programmes for diagnosis based on the delineation of morphological attributes of retinal blood vessels, such as length, width, branching pattern or the complexity of vasculature [21]. Figure 1.1 shows the left anterior cortex of a wild-type (normal) mouse and a mouse with Alzheimers disease. Note that the vasculature appeared much denser and more irregular than in normal mouse. Traditional methods of counting vessel branches [22] or measuring vessel density are simply not good enough [23] and are also unsuitable for analysing the microvasculature.

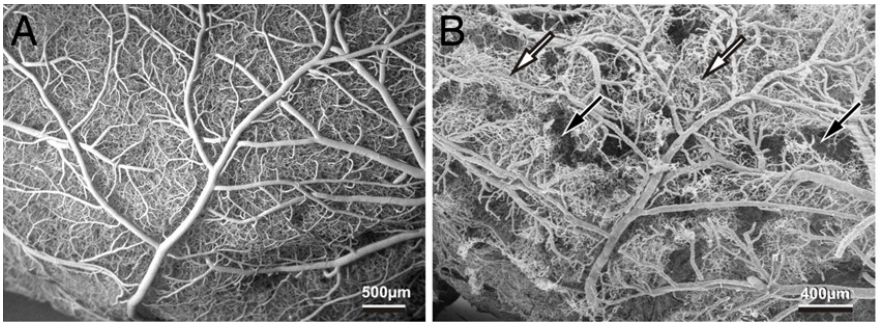


Figure 1.1: Overview of the anterior cortex of a normal mouse and a diseased mouse (from [24]).

One way is to use fractals analysis. Fractals can be described as objects which contain regions that are similar to the object as a whole. In recent years, fractal analysis has attracted much interest from the biomedical imaging and neuroengineering communities [25] and has been used to analyse the retinal vasculature [26, 27], as the vasculature typically exhibits fractal properties or self-similarity at multiple scales. However, these existing methods mostly use monofractal analysis, calculating a single fractal dimension value for the entire vasculature. A single fractal dimension value is insufficient to describe the whole complex vasculature and thus lacks the discriminant power required to distinguish healthy and pathological vasculature [26, 27]. A generalisation of this dimension is the theory of multifractal systems [28], which is a powerful tool for quantitative analysis of complex shapes and forms in nature. The microvasculature is multifractal and can be described by a multifractal spectrum of fractal dimensions and can then be analysed mathematically using the multifractal formalism [29, 30]. Previous research has shown visually that some diseases such as diabetic retinopathy cause damage to the retinal blood vessels, and this is reflected in the multifractal spectrum of the retinal vasculature [31, 32]. But at present, there has been no systematic research extracting discriminant features from the spectrum to diagnose disease.

1.2 Microglia Histology

1.2.1 Motivation and Objective

Microglia are immune cells exclusive to the central nervous system (CNS) and about 1.5 trillion of them reside in the brain and spinal cord [33, 34]. According to [35], blood vessel formation requires an adequate resident microglial population, because the formation can be interrupted by pathology (e.g. diabetic retinopathy), therefore understanding the biology of microglia is also very important for the study of blood vascular pathology.

Microglia present with multiple protective to detrimental phenotypes associated with motility and morphological changes, in response to a variety of signals [36]. In the healthy brain, microglia constantly survey the surrounding tissue with extended processes, clear debris from dead cells, or prune and maintain brain synapses. They are also essential to learning and memory [37, 38] and protect neurones from damage and they mediate pain [39, 40]. In response to an injury or infection, microglia initiate an early, protective response by moving towards the site of the injury, where they release a cascade of chemicals leading to repair of the damaged area. Moreover, microglia activation is a hallmark of chronic neuroinflammation, which is believed to play an important, but incompletely understood, damaging role in a range of brain disorders, including stroke, multiple sclerosis, Parkinson's, Huntington's and Alzheimer's diseases [41, 42, 43], but can also reflect a neuroprotective behaviour in these chronic conditions [36].

The heterogeneity of microglial functions is in part linked to their shape and activation state, and much information can be obtained from their morphological characteristics [44]. Microglial cell shape evolves from resting fully ramified with

extending tortuous processes and smaller soma, to the fully activated amoeboid shape with a larger soma and shorter or no processes by deramifying and reramifies upon deactivation, as shown in Figure 1.2 [45, 46]. To date, microglia activation has been linked to three distinct functions: a classical pro-inflammatory activation state, an alternatively activated anti-inflammatory state, and its overlapping and complementary acquired deactivation state associated with the anti-inflammatory and functional repair phenotype [36].

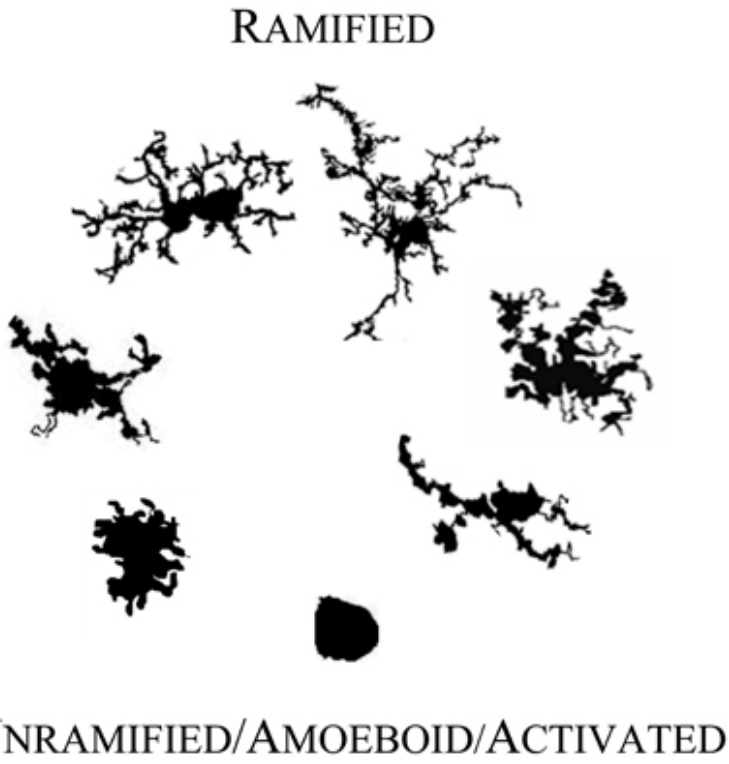


Figure 1.2: Microglial morphology in adult human CNS (from [47]).

The objective is to classify microglia activation states when analysing histological rat brain images. This can help pathologists with disease diagnosis [48], provide essential information for understanding diseases of the central nervous system and other detrimental or beneficial effects of microglia activation [29], and is essential to validating in vivo biomarkers [49] for more effective longitud-

inal monitoring of patients and populations at risk of diseases associated with neuroinflammation [50].

1.2.2 Challenge

One of the major challenges in quantitative microglial analysis from immunohistological images is the development of automated microglial segmentation methods. Manual or semi-automated segmentation methods are time-consuming and require user intervention [51, 52] with an element of subjectivity and inter-observer variability. Image analysis approaches that are commonly used for quantifying histology and that rely on thresholding, such as ImageJ [53], struggle with inhomogeneous immunohistochemistry images, where even staining over a single brain slice and across different slices from subsequent preparations can be challenging.

Another key challenge is the classification of distinct morphological states from resting-ramified to activated amoeboid, particularly the intermediate states, which is intimately linked to the multiple phenotypes of microglia [44]. Fractal analysis methods have the potential to classify microglia morphology across the range of shapes from ramified and activated. Recent work has also considered microglia as monofractals, and used a single fractal dimension value to describe the entire microglial structure [54, 44]. However, fractal dimension alone is not enough to discriminate microglia activation states as it only measures the dimension of the space that the data fills but not how the data fills the space. Moreover, a systematic review has indicated that there is little research into the classification of microglia activation states [44, 54, 55].

1.3 Major Contributions of the Thesis

To overcome some of the challenges mentioned above, two frameworks are developed to deal with blood vessel data and microglial data respectively. The frameworks are demonstrated using three case studies and the contributions made in this thesis can be summarised as follows:

- **3D Micro-CT and MRI Brain Data** A novel framework has been produced for 3D vessel segmentation involving the combined use of line filter and Hessian–based vessel filter that can overcome the critical problems with existing methods. Quantitative evaluation of the performance of the method under varying noise levels was performed. Results show that the vessel filter framework is effective in dealing with high–density vessels, including microvessels, and noise present in images. For example, the method produced 94.46%, 95.29% and 92.48% of segmentation accuracies on three synthetic vessel-like model (branch, spiral and column) with -80dB added Gaussian noise. The framework was then tested on an MRI dataset of 3D human brain vasculature, as well as a micro-CT dataset of rat and monkey brain vasculature - micro-CT can achieve resolutions on the order of several μm, allowing the 3D microvasculature to the imaged down to the capillary level. Multifractal analysis of the morphology of the segmented vasculature was also performed to give an indication of the potential applications of the proposed method.

- **2D Retinal Data** An overview on the methods for retinal vessel segmentation has been presented, which provides some guidance for researchers in this area. 2D retinal vessel images are used to visualise the performance of

the methods. Methods for extracting features from multifractal spectra of vessels and classification of these features to distinguish healthy and pathological vessels are also introduced. The proposed analysis method considers vessels as multifractals, and uses a multifractal spectrum to describe the entire vasculature. It then extracts multiple and discriminant features from the multifractal spectrum at varying scales for effective classification. The methods are tested on three publicly available retinal databases (STARE, MESSIDOR, DIARETDB). Results show that high classification accuracy (85.5%, 77% and 81.2%), using a support vector machine (SVM), can be achieved by combining features extracted from multifractal spectra and those extracted from Fourier power spectra of retinal images.

- **Microglial Histology Data** We have developed a system for neuroscientists to quantitatively analyse microglia histology data. Microglial cells are first segmented using the Mumford-Shah total variation [56, 57, 8] and fast split Bregman methods [58], followed by multifractal analysis of the segmented structures. SVM is then used to classify microglia activation states based on novel fractal features extracted from the microglia. We show that this framework offers advantages over existing image analysis methods by validating against manual analysis of imaging data from wild type mice and a transgenic mouse model of Alzheimer's disease. Experiments show that the proposed segmentation method has produced similar results to those obtained by the manual method, also, it is more robust than existing methods such as thresholding. These properties ensure that the proposed segmentation method is scalable to large datasets, allowing the analysis of microglia morphology in regions of interest as well as across the whole brain.

1.4 Organisation of the Thesis

The remaining chapters of this thesis are organised in the following way:

Chapter 2 reviews traditional methods which are suitable for segmenting vessel images. Brief introductions to feature extraction and classification methods are also given.

Chapter 3 contains three sections to present the proposed methods:

Section 3.1 provides details of a combinatory vessel filter framework that is effective in dealing with high–density vessels and noisy background.

Section 3.2 provides details of a microglia segmentation method that overcomes the common problems that were described in previous research due to the inhomogeneity of the images.

Section 3.3 provides details of novel feature extraction methods. The methods extract features from multifractal spectra of retinal vessels and microglia cells for classification.

Chapter 4-Chapter 6 presents three case studies to demonstrate the scalability of the proposed analysis methods on real medical data:

Chapter 4 first validates the proposed vessel segmentation method using three 3D synthetic vessel-like model (branch, spiral and column) in varies levels Gaussian noise. Then, results of vessel segmentation, vessel size visualisation, and vessel fractal feature extraction on 3D Micro-CT and MRI brain vascular data are presented.

Chapter 5 first compares vessel segmentation results between the proposed method and the existing methods on a publicly available 2D retinal dataset, DRIVE. A well-know retinal vessel analysis software ARIA is then modified using the proposed segmentation method and the improvement made to the software

is demonstrated. Furthermore, experiments results using the proposed fractal feature extraction method for the classification of healthy and diabetic retinal vasculatures on three publicly available 2D retinal datasets are shown. Where STARE and MESSIDOR are used for validation and DIARETDB is used for further testing.

Chapter 6 gives analysis results using immunohistological images, including both segmentation and classification of microglial in four activation states.

Finally, Chapter 7 provides conclusions and some comments for future research work on blood vessel and microglia analysis.

Chapter 2

Literature Review

A typical medical image analysis system consists of several steps, from image segmentation to feature extraction and classification. This chapter gives a literature survey on traditional vessel segmentation methods. Some feature extraction and classification methods are also briefly introduced.

2.1 Segmentation

It is very difficult to visualise vessels in an image due to the complex structures, so segmentation is used as a tool to present vessels as a binary representation (or to extract from, for example, organs) before medical staff browse through it. This section reviews several vessel segmentation methods.

2.1.1 Local Entropy Thresholding

The simplest and the most commonly used technique for image segmentation is thresholding. The method replaces each pixel in an image with a black pixel, or 0, if the image intensity is less than a user selected value, or a white pixel, or 1, if the image intensity is greater than the value. The method is fast and easy to use but it requires user intervention. Therefore, methods such as Otsu thresholding [59, 60] or adaptive thresholding [61, 62] were developed for automatic selection of the thresholding value.

Local entropy thresholding (LET) is one of the methods which automatically select a thresholding value and it has been successfully applied for vessel segmentation [63, 64, 65, 66]. LET is to create a grey level co-occurrence matrix to automatically estimate the threshold value, based on the entropy of an image [67], so that human intervention for selecting a threshold value does not need to be involved. Because a co-occurrence asymmetric matrix is used to indicate the spatial structure of an image, it solved the problem that different images with identical histograms produce the same entropic value [68, 69].

$$t_{ij} = \sum_{l=1}^{P} \sum_{k=1}^{Q} \delta \tag{2.1}$$

$$\text{where} \quad \delta = 1 \quad \text{if} \quad \begin{cases} f(l,k) = i \quad \text{and} \quad f(l,k+1) = j \\ \qquad\qquad or \\ f(l,k) = i \quad \text{and} \quad f(l+1,k) = j \end{cases} \tag{2.2}$$

$$\delta = 0 \quad \text{otherwise} \tag{2.3}$$

Here t_{ij} is the $(i,j)th$ entry of the matrix that gives the number of times the

grey level j follows the grey level i. Let s be the threshold such that $0 \leq s \leq L-1$ (L is the length of the segment). Then the threshold s partitions the co-occurrence matrix into four quadrants, namely A, B, C, and D, as shown in Figure 2.1, where A and C represent grey level transition within the vessel object and background respectively. The grey level transition between the vessel object and background are placed in quadrants B and D.

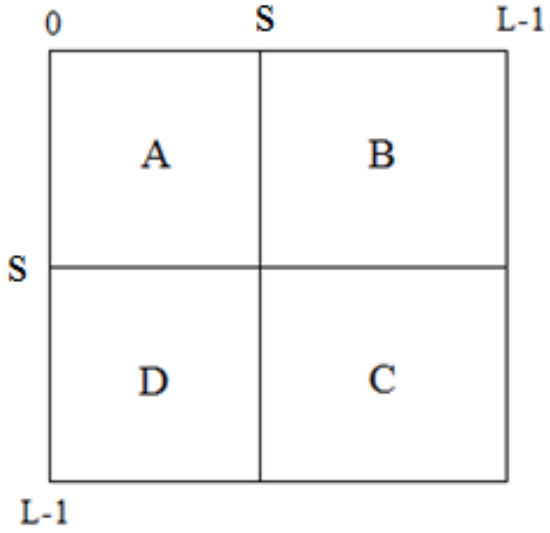


Figure 2.1: Quadrants of co-occurrence matrix.

The normalised probabilities of each quadrant are defined as:

$$P_{i,j}^{A} = \frac{P_{i,j}}{P_A} = \frac{t_{ij}}{\sum_{i=0}^{s}\sum_{j=0}^{s} t_{ij}} \tag{2.4}$$

$$for 0 \leq i \leq s, 0 \leq j \leq s \tag{2.5}$$

$$P_{i,j}^{C} = \frac{P_{i,j}}{P_C} = \frac{t_{ij}}{\sum_{i=s+1}^{L-1}\sum_{j=s+1}^{L-1} t_{ij}} \tag{2.6}$$

$$for\ s+1 \leq i \leq L-1,\ s+1 \leq j \leq L-1 \tag{2.7}$$

Here p_{ij} is the probability of co-occurrence of grey levels i and j, and P^A and P^C are the probabilities of vessel object and background. Hence, the total second-order local entropy of the object and background can be written as:

$$H_T^{(2)}(s) = H_A^{(2)}(s) + H_C^{(2)}(s) \tag{2.8}$$

$$H_A^{(2)}(s) = -\frac{1}{2}\sum_{i=0}^{s}\sum_{j=0}^{s} P_{ij}^A \log_2 P_{ij}^A \tag{2.9}$$

$$H_C^{(2)}(s) = -\frac{1}{2}\sum_{i=s+1}^{L-1}\sum_{j=s+1}^{L-1} P_{ij}^C \log_2 P_{ij}^C \tag{2.10}$$

The value of s which maximises $H_T^{(2)}(s)$ gives the optimal threshold for vessel segmentation.

The disadvantage of this method is that it is not scale invariant and is not reliable using images with noise and without inhomogeneity, so a proper vessel enhancing algorithm is required. For example, the method has been associated with morphological processing for detecting retinal spot lesions [70]. In [17, 63], a matched filter was used to enhance the vessels followed by LET for vessel segmentation.

2.1.2 Multiscale Vesselness Filter

Before segmentation, image enhancement can be used to increase or decrease image contrast. A method which was particularly designed for enhancing vessels

in a image was developed, by considering eigenvalues of the Hessian to determine the likelihood that a vessel is present, based on the computed vesselness measure [71, 72]. The method is not optimal as the range of scale values needs to be given before segmentation [73], and the outputs of this filter are highly sensitive to noise. Therefore, an improved function which interprets geometrically the eigenvalues of the Hessian matrix was then introduced [19, 74]. Until now, many of the vessel segmentation algorithms are based on this vesselness filter [75, 76, 77, 78, 79].

To obtain the vesselness response of an image, the Hessian matrix (second-order partial derivatives) for each point in the image is first computed. Eigenvectors (the directions of principal curvature) of these matrices and their corresponding eigenvalues (the amount of curvature in each direction) are then found. This directly gives the direction of smallest curvature along the vessel. Table 2.1 lists the relations that must hold between the eigenvalues of the Hessian for the detection of different structures, where λ_k is the eigenvalue with the k_{th} smallest magnitude. For an ideal tubular structure in a 3D image, a vessel pixel will have a small λ_1 (or zero), and large λ_2 and λ_3, as illustrated in Figure 5.3. Here the eigenvector of λ_1 indicates the direction along the vessel (the direction of smallest curvature).

Table 2.1: Multiscale vesselness filter can detect plate-like, tube-like and sphere-like objects depending on the value of the eigenvalues λ_1, λ_2 and λ_3 (from[19]).

2D		3D			Structure
λ_1	λ_2	λ_1	λ_2	λ_3	
		Low	Low	High	plate-like structure
Low	High	Low	High	High	tubular structure
High	High	High	High	High	blob-like structure

The eigenvalues obtained are then used to describe the geometric similarity

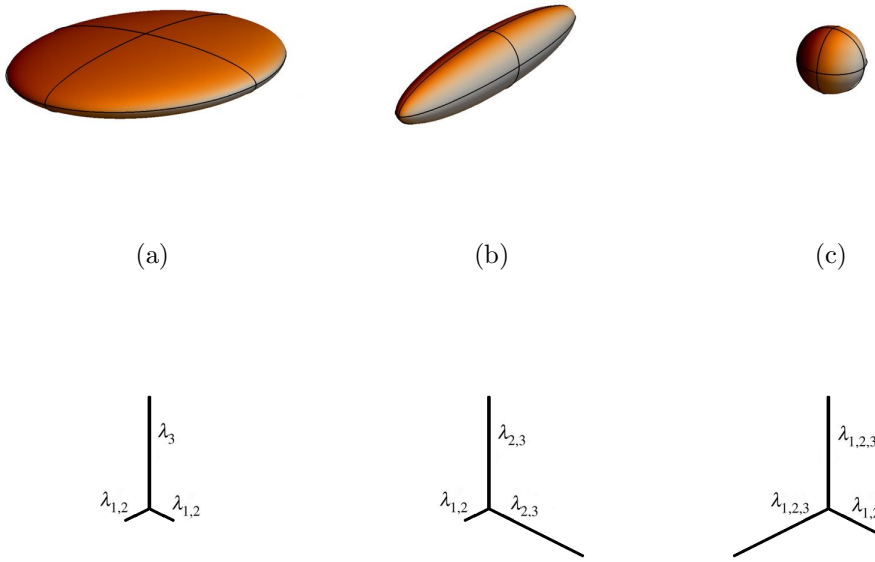


Figure 2.2: Possible models of the (a,d) plate-like, (b,e) tube-like and (c,f) sphere-like objects, the pattern can be known by comparing the value of the eigenvalues λ_1, λ_2 and λ_3 (from [80]).

measures.

$$R_A = \frac{|\lambda_2|}{|\lambda_3|}, R_B = \frac{|\lambda_1|}{\sqrt{|\lambda_2 \lambda_3|}}, S = \sqrt{\sum_{j \leq D} \lambda_j^2} \tag{2.11}$$

R_A distinguishes between plate-like and line-like structures, R_B accounts for the deviation from a blob-like structure and S is defined to control the sensitivity of the vesselness response to background noise. D is the dimension of the image. The vesselness function, V^L, can then be defined according to these measures to obtain probability-like estimates of each voxel, representing the likelihood of a

voxel being a vessel point. If either $\lambda_2 = 0$ or $\lambda_3 = 0$ then $V^L = 0$, otherwise

$$V^L = (1 - G(R_A, \alpha))G(R_B, \beta)(1 - G(S, \gamma)) \tag{2.12}$$
$$G(a, b) = \exp\left(-\frac{a^2}{2b^2}\right)$$

Based on this, V^L is high for regions with high contrast and low for regions where no structure is present. α, β and γ are user-defined thresholds to control the sensitivity of the vesselness measurement to the measures R_A, R_B and S respectively.

The equation for 2D images follows the same reasoning as in 3D, where $R_B = \frac{\lambda_1}{\lambda_2}$

$$V^L = G(R_B, \beta)(1 - G(S, \gamma)) \tag{2.13}$$
$$G(a, b) = \exp\left(-\frac{a^2}{2b^2}\right)$$

A final estimate of vesselness response is then integrated with the responses at different scales L as vessels appearing in varying width. Further discussion regarding vessel scales is explained in Section 4.2.1. Following this, a threshold value is required, to filter out the noise and also for binarisation. There are some ways to implement thresholding. A user-selected threshold value is simple but it is susceptible to error. Local entropy thresholding (Section 2.1.1) is more for suitable for automatic vessel segmentation.

Moreover, centreline detection can be achieved, based on the fact that the middle pixels of vessels always have the highest vesselness measurements [81, 74, 82]. For any point in the vesselness image, two neighbourhoods along the eigenvalue direction (the eigenvector) are compared. If the measurement is the

local maximum, it is retained and considered as a centreline pixel, otherwise, the point is deleted. Figure 2.3 shows part of the vesselness image. Red values are vesselness measurements, while the green line indicates the vessel's centreline. It is believed that there exists a relationship between the centreline and the vesselness measurements along the eigenvector direction. The yellow line is then assumed to be the width of the vessel which will be examined in future work.

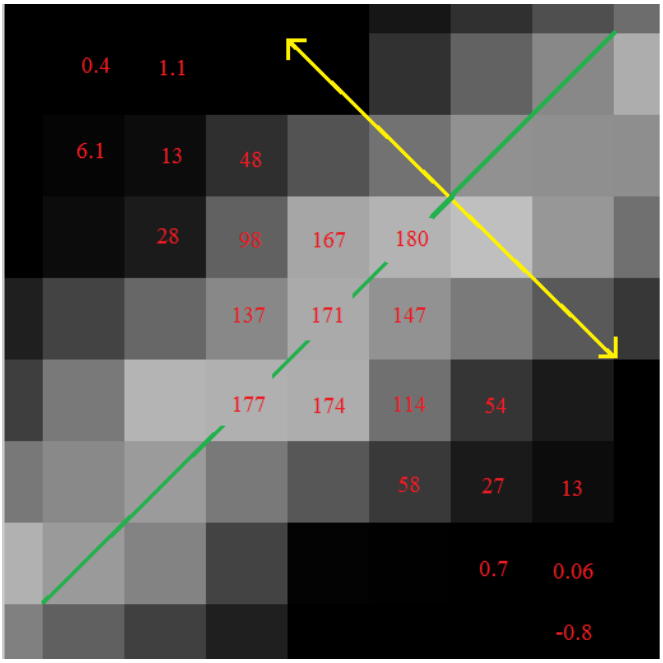


Figure 2.3: Zoomed-in vesselness image.

However, the method suffers from two major drawbacks. (a) It is not scale invariant: user interaction is required for selecting the range of scales, although it is very difficult to adjust the value. (b) It does not perform well on vessel images with large amounts of noise.

Many of the existing vessel segmentation algorithms are based on this vessel enhancement filter by incorporating additional pre-/post-processing methods. For example, in [73], the initialisation of seed pixels for vessel tracking is done using a vessel enhancement filter. In [77], a vessel enhancement filter was used together

with a denoising method, anisotropic diffusion, which is an iterative process that smooths the image while at the same time preserving certain structure of that image [81, 83]. The generalisation of this process is to smooth the image without removing the vascular structures [84]. The method has the potential to deal with noisy vasculature images, but microvasculature may be removed.

2.1.3 Wavelet Transform Modulus Maxima (WTMM)

Blood vessel edge detection is also important for understanding the vasculature in retinal images [85, 86, 87]. Conventional edge detectors often use image gradient for detecting edges, as the large gradient values always become edge pixels. The image gradient is a very commonly used measurement of how the image changes along a direction, the magnitude of gradient tells how this direction changes, while the image gradient direction is the most rapidly changing direction. One simple edge detection method is the Sobel operator [88], which computes gradient values through the convolution of a source image with two kernels (masks). However, the gradient-based method relies upon the first derivative, so it is very susceptible to noise and not capable of detecting edges at different scales [89]. The wavelet transform overcomes these issues by convolving the signal with wavelets rather than simple kernels [90]. A method, which is based on the ideas of gradient and a well-known wavelet transform method, called wavelet transform modulus maxima (WTMM), to extract edges was introduced in [91]. The basic concept of the wavelet transform is to convolve a signal with a small wave to extract information such as edges from that signal. The wavelet transform uses only two components, $W_s^x f\,(x,y)$, $W_s^y f\,(x,y)$ in scales s:

$$\left| \begin{array}{c} W_s^x f(x,y) \\ W_s^y f(x,y) \end{array} \right| = s \left| \begin{array}{c} \frac{\partial (f * \phi_S)(x,y)}{\partial x} \\ \frac{\partial (f * \phi_S)(x,y)}{\partial y} \end{array} \right| \tag{2.14}$$

$$\phi^x(x,y) = \frac{\partial \phi(x,y)}{\partial x}, \phi^y(x,y) = \frac{\partial \phi(x,y)}{\partial y} \tag{2.15}$$

where a 2D wavelet (e.g. Gaussian) can be defined as $\phi^x(x,y)$ and $\phi^y(x,y)$, the $*$ expresses the convolution, and f is the gradient vector. The wavelet transform modulus and gradient direction are defined as:

$$M_s f(x,y) = \sqrt{|{W_s}^x f(x,y)|^2 + |{W_s}^y f(x,y)|^2} \tag{2.16}$$

$${A_s}^x f(x,y) = \arctan\left(\frac{{W_s}^x f(x,y)}{{W_s}^y f(x,y)}\right) \tag{2.17}$$

For any point in the original image, two neighbourhoods along the gradient direction are compared. If the edge intensity $M_s f(x,y)$ is the local maximum, it is retained and considered as an edge pixel, otherwise, the point is deleted. Following this, a threshold value is chosen to filter out the noise, and all the individual maxima are chained to recover the edges. The method can reliably detect the edges in an image with slight noise and without intensity inhomogeneity.

Conventional WTMM is very simple, so a complex method was introduced using B-spline wavelet magnitudes and their local standard deviations to remove the effects of intensity inhomogeneity and noise [92], and this overcomes the limitation of gradient-based and conventional wavelet-based edge detection techniques [18]. According to [18], a quadratic B-spline function is used rather than Gaussian because B-spline is smooth and compactly supported to minimise truncation error in numerical implementation. A B-spline wavelet-based local standard deviation

function was developed to compute the edge strength, proving that the detected edges in regions with different intensity contrasts give the same edge strength, and it is also very useful to deal with the problem of contour leakage or discontinuity during active contour evolution due to the well-defined edges [18]. The function is defined as:

$$G(x) = \frac{|\nabla W_s f(x, y, z)|}{\sigma(|\nabla W_s f(R)|) + \varepsilon'} \tag{2.18}$$

For an edge point x belonging to a local region R, where $W_s f(R)$ is the collection of wavelet magnitudes of all points. Here, σ represents the standard deviation of the wavelet magnitudes. A constant ε' is used to prevent division by zero when local size is zero. The method improves the conventional WTMM by using a different wavelet and an additional edge map function, but it is still susceptible to errors from the user-selected scale value, because blood vessels normally appear in varying width.

2.1.4 Level Set Methods

Because vessels are always connected and, therefore, techniques such as the level set method can follow a whole vasculature without searching the majority of the image that does not contain vessel [93]. The level set method is a powerful computational tool for tracking the evolution of curves/surfaces and there have been many modifications and applications are suggested to deal with vessel segmentation [94, 95, 96]. The basic idea of the method is to represent the curve or surface at a certain time t as the zero level set of a level set function $u(t, x)$. It evolves this curve by applying forces normal to the surface and the contour evolution stops at positions where the values of gradient magnitude are large [97]. The level set equation is as follows:

$$u_t + F(t,x)\,\nabla_x u = 0 \tag{2.19}$$

$$u(0,x) = u_0(x) \tag{2.20}$$

Here $F(t,x)$ is the speed function that defines how to move each point of the interface and $u(0,x)$ determines the initial value [98]. The basic gradient-based level set is fast and simple on smooth and regular image but it often fails at low contrast edges or gaps in the object, as it is highly dependent on image contrast; as a result, the evolving contour simply leaks through the gaps and the object is represented by incomplete contours [99, 100].

A complex level set method was introduced based on local phase [101, 102, 103]. Because vessels appear either as lines or edge pairs with varying widths and contrasts, the method uses local phase as a line or edge detector incorporating multiple scales. The outcome is a 'global' phase that can be used to drive a contour robustly towards the vessel edges. The output from a quadrature filter is a complex valued filter pair consisting of a line filter as the real part and an edge filter as the imaginary part [104]. The filtered signal is strongly 'line-like' when the filter response is purely real, is edge-like when it is purely imaginary. The magnitude of the filter response gives the strength of the structure, while the angle (local phase) of the response indicates whether it is line or edge. The angle is referred to as the local phase.

Because it is independent of signal strength, the local phase as a line/edge detector is invariant to image contrast, making it more powerful when compared to gradient-based edge detectors. Multiscale is also considered by integrating the filter responses of all scales followed by normalisation [105]. Then a level set

method for front propagation is used to relate to the phase-based edge detector (global phase map) [106, 107]. The idea is to use the real part of the phase map as a speed function. However, the method is not suitable for analysing 3D microvasculature due to its high computational cost.

2.2 Feature Extraction

After segmentation, essential information can be extracted from the segmented image. This is known as feature extraction. The existing feature extraction methods on vessel images are commonly used for vessel segmentation, that is, to determine whether a point belongs to a vessel pixel [108, 109]. For our study, this step is used to extract useful features from an image to distinguish healthy and pathological retinal vessels. The output of this is a vector storing information about the identity of the image. Traditional methods extract features directly from an image, such as Gabor feature extraction [110]. These methods, however, are unsuitable for classifying vessel images because the classification can be affected by the orientation of the vasculature and the illumination of the images. New methods are therefore in demand for vascular analysis. The following section will briefly introduce two feature extraction methods based on fractal and wavelet scaling properties.

2.2.1 Multifractal Feature Extraction

In recent years, fractal analysis has attracted much interest from the biomedical imaging and neuroengineering communities [25] and has been used to analyse retinal vasculature [26, 27, 111], because the vasculature typically exhibits fractal properties or self-similarity at multiple scales.

The concept of fractality as a measure of the complexity of a signal was conceived by Benoît Mandelbrot [112] while discussing self-similar objects. The fundamental idea is to investigate the object at different scales of measurement. This lays the foundations for the idea of fractal dimensions, a means to quantify the geometry of irregular objects.

There are different ways to define fractal dimension D depending on the measure with which the scaling law is determined. The simplest is the box-counting dimension, where the measure is the box that contains at least a point of the object, and the scaling law is $N(s) = \lim_{s \to 0} s^{-D}$, where $N(s)$ is the minimum number of boxes needed to cover the object, s is the monotonically decreasing size of the box, and D is the fractal dimension of the object.

Rather than calculating a single fractal dimension, multifractal analysis [32] of a structure gives a set of fractal dimensions, each of which measures the dimension of the set of points on the structure with the same Hölder exponent h. The Hölder exponent of a function f at a point $\mathbf{x}_0$ is the supremum of all $h \in (n, n+1)$ where the following condition holds

$$|f(\mathbf{x}) - P_n(\mathbf{x} - \mathbf{x}_0)| \leq C|\mathbf{x} - \mathbf{x}_0|^h \tag{2.21}$$

where C is a constant, bfx is a point at the neighbourhood of $\mathbf{x}_0$, and P_n is a

polynomial of degree $n < h$. Effectively, the Hölder exponent of a function f at a point characterises the regularity of f at the point.

The set of fractal dimensions forms the multifractal spectrum $D(h)$, a function of h. The Hölder exponent is commonly represented as α, and the corresponding multifractal spectrum as $f(\alpha)$. In general, the wider the fractal spectrum, the richer the signal. If the spectrum reaches maximum at α_0, then $\alpha_{\max} - \alpha_0$ and $\alpha_0 - \alpha_{\min}$ indicate left/right skewed, or symmetry if they are equal. In practice, α and $f(\alpha)$ are approximated based on their relationship with the generalised fractal dimension D_q of measure μ [6], where q can take a range of values. This relationship is analogous to that between the multifractal formalism and statistical thermodynamics, which provides a natural connection between $f(\alpha)$ and $\tau(q)$ [113, 114] through the power law behaviour of the partition function Z:

$$\mathcal{Z}(q, s) = (\sum_i \mu_i^q(s)) \sim s^{\tau(q)} \tag{2.22}$$

$$f(\alpha) = q\alpha(q) - \tau(q) \tag{2.23}$$

where $\tau(q) = (q-1)D_q$, and $\alpha(q) \cong \frac{\mathrm{d}\tau(q)}{\mathrm{d}q}$. The variables q and $\tau(q)$ play the same role as the inverse of temperature and free energy in thermodynamics, and the Legendre transform (2.23) indicates that α and $f(\alpha)$ are the thermodynamic conjugate to q and $\tau(q)$.

2.2.2 Wavelet Scale Spectra Feature Extraction

Another way to estimate fractal dimension of a structure is to through wavelet-scale spectra that produced by discrete wavelet transform [115, 116]. But there is little prior research in the wavelet-scale spectra analysis of medical images.

Discrete wavelet transform consists of decomposition and reconstruction [117]. The input signal is first decomposed into approximation coefficients using a low pass filter (low frequency, such as noise) and detail coefficients using a high pass filter (high frequency, such as edge). The output of each filter is then down-sampled by 2 to discard half the samples because half the frequencies of the signal have been removed. The method then continues by using the same process on the approximation coefficients and produces an approximation and three detail coefficients at the next level. The process continues until a specified level is reached [118]. Figure 2.4 illustrates the scheme of decomposition at the second level. Wavelet scale spectra are obtained by summing the intensity of a truncated set of DWT coefficients at each scale.

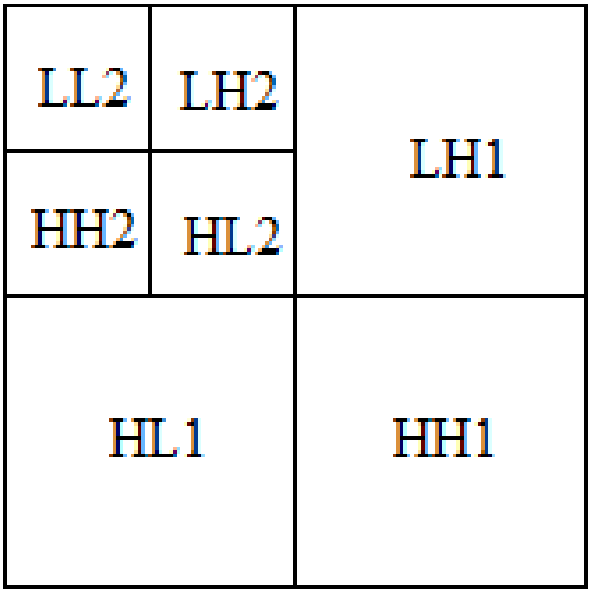


Figure 2.4: Decomposition to the second level. L: Low frequency. H: High frequency.

2.3 Classification

There are some well-known machine learning based classifiers, such as (k)nearest neighbour and decision trees. However, as seen from the previous section, features extracted from vasculatures are mostly nonlinear, so linear classifiers are unsuitable for classifying vasculature. This section introduces two supervised classifiers which have been successfully applied to texture analysis applications and are potentially suitable for our study.

2.3.1 Support Vector Machine

Support vector machine (SVM) has been known as one of the best classification techniques for simple problems [119]. It was originally designed for two-class classification problems and it has been successfully applied to face recognition [119, 120, 121] and computer-aided diagnosis of diseases [109, 122, 123].

Conventional SVM classifies data by finding an optimal hyperplane that separates data points of one class from those of the other class. The position of the hyperplane is defined by a small subset of data that lies closest to the decision surface, and these points are known as support vectors. The best hyperplane for an SVM is the one with the largest margin between the two classes, where margin is the distance from the decision surface to the support vectors [119].

Figure 2.5 illustrates the concept of this method. Hyperplane $w \cdot x + b = 0$ with the largest margin represents the best classifier (sometimes known as the optimal separating hyperplane, OSH), where w is the normal vector to the hyperplane, b is a bias, and margin is defined as the distance from this hyperplane to the nearest training point of either class. To obtain the OSH, two hyperplanes $w \cdot x + b >= 1$ and $w \cdot x + b <= -1$ with the largest distance $2/|w|$ but without any training points falling between them need to be found. The problem, therefore, turns out to be solving the minimisation of $|w|$. Once all the parameters are found, classification can then be done by solving the decision function $f(x) = w \cdot x + b$ for every new point x.

The original OSH algorithm was a linear classifier [124], but it is not found to be suitable for solving complex problems, such as classifying vasculature. A method of creating nonlinear classifiers was suggested by rearranging the original object, using a set of mathematical functions, known as kernels [125], as illustrated

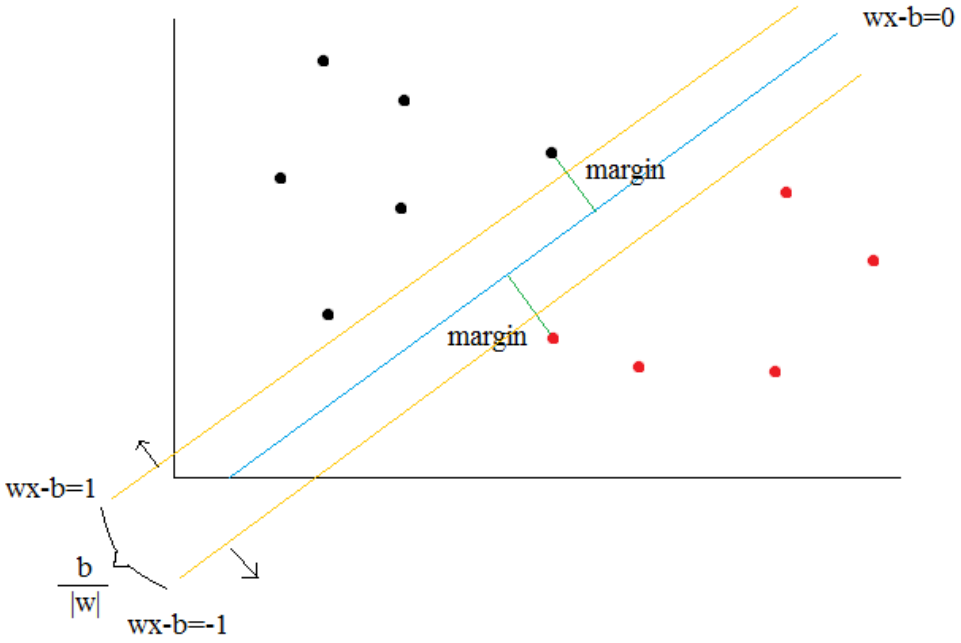
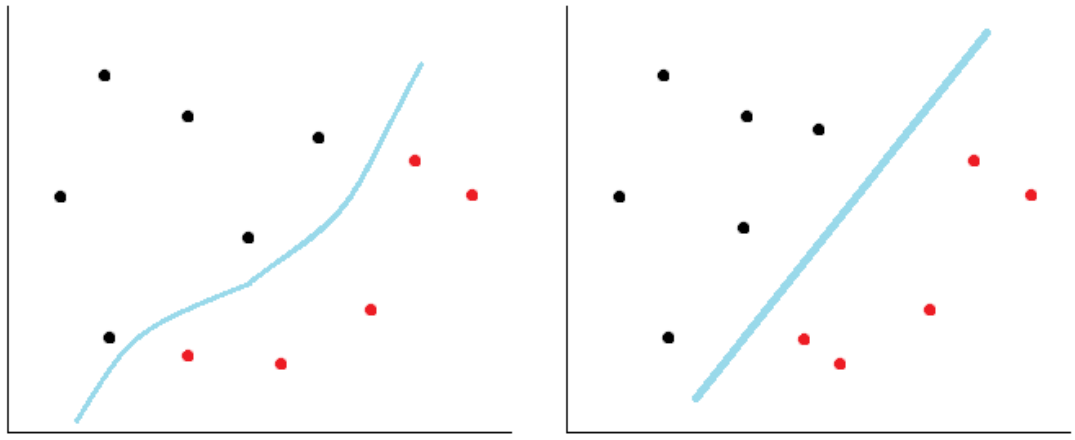


Figure 2.5: SVM concept.



(a) (b)

Figure 2.6: Nonlinear SVM concept (a) original data (b) rearranged data.

in Figure 2.6. It can be seen that the rearranged objects are linearly separable and therefore, the problem becomes simpler: finding an optimal line that can separate two groups of data, instead of constructing the complex curve.

2.3.2 Cosine Similarity Metric Learning

A metric learning method called cosine similarity metric learning (CSML) was introduced in [121]. Although CSML was originally designed for face verification, it has a wide range of applications and can potentially be used for classifying vasculature, using features extracted from the multifractal spectrum, as described in Section 2.2.1.

The idea of CSML is to learn a transformation matrix from the original space of the training data to a subspace which is more discriminant of the classes. CSML makes use of cosine similarity instead of the more popular Euclidean distance. Cosine similarity (CS) is a measure of the similarity of two vectors by the cosine of the angle between them. CS between two vectors (x and y) is defined as,

$$CS\left(x,y\right)=\frac{x^{T}y}{||x||\,\|y\|} \tag{2.24}$$

CS has a special property that makes it suitable for metric learning: the resulting similarity measure is always within the range of -1 and $+1$, which allows the objective function to be simple and effective.

Specifically, let $(x_i,y_i,l_i)_{i=1}^{s}$ denote a training set of s labelled samples with pairs of input vector $x_i,y_i\in R^m$ and binary class labels $l_i\in(1,0)$ which indicates whether x_i and y_i match or not. The goal is to learn a linear transformation $A:R^m\rightarrow R^d\,(d\leq m)$, and CS in this subspace is calculated as:

$$CS\left(x,y,A\right)=\frac{\left(Ax\right)^{T}\left(Ay\right)}{\|Ax\|\,\|Ay\|}=\frac{x^{T}A^{T}Ay}{\sqrt{x^{T}A^{T}Ax}\sqrt{y^{T}A^{T}Ay}} \tag{2.25}$$

An objective function $f\left(A\right)$ is defined so as to minimise the cross validation error:

$$f(A) = g(A) - h(A) \tag{2.26}$$

where Pos and Neg are indices into positive and negative samples and

$$g(A) = \sum_{i \in Pos} CS(x_i, y_i, A) - \sum_{i \in Neg} CS(x_i, y_i, A) \tag{2.27}$$

$$h(A) = \beta ||A - A_0||^2 \tag{2.28}$$

The role of $g(A)$ is to encourage the margin between positive and negative samples to be large. A large margin can help to reduce the training error. $g(A)$ can be seen as a simple voting scheme from each sample. The reason that votes from samples are treated equally is that the cosine similarity function is bounded by 1. Also, because of this simple form of $g(A)$, optimisation of $f(A)$ can be very fast.

The role of $h(A)$ is to regularise matrix A to be as close as possible to a predefined matrix A_0 which can be any matrix. The parameter β plays an important role here. It controls the trade-off between maximising the margin $g(A)$ and maximising ($h(A)$), or the distance from A to A_0.

A suitable β is estimated using cross validation and coarse-to-fine search strategy (meaning the range of searching area decreases over time). A_0 is defined as a rectangular matrix:

$$A_0 = \begin{bmatrix} 1 & 0 & ... & 0 & 0 & 0 \\ 0 & 1 & ... & 0 & 0 & 0 \\ ... & ... & ... & ... & 0 & 0 \\ 0 & 0 & ... & 1 & 0 & 0 \end{bmatrix} \in R^{m \times d}$$

With the objective function set up, $f(A)$ is differentiable with regard to matrix A, so optimisation is done using the conjugate gradient method.

The learnt transformation matrix A is then used to transform feature vectors (x_i, y_i) in the original space to the new subspace, and the CS is calculated and thresholded to determine the similarity of two images, with the threshold value estimated from the training set.

Although CSML has achieved highest accuracy in the literature, the method requires a large amount of training data to perform well. However, it is very difficult to collect such an amount of data in real world applications [121]. Comparably, SVM is more suitable for our study because of its simplicity in implementation, and it only requires a small amount of training data and requires less time to train the model.

Having reviewed the literature thoroughly, we start to present our contributions in the next chapter.

Chapter 3

Introducing the Proposed Methods

This chapter introduces two improved segmentation methods and one novel feature extraction methods, which have addressed major issues when analysing vascular and microglia data. These include a vessel segmentation method that is effective in dealing with high–density vessels in both 2D and 3D; an automated method for segmenting the microglia from 2D histology images; and a feature extraction method for classifying normal retinal vasculature and diabetic retinal vasculature, or for classifying microglial cells in different states. Detail of these methods is given in the following sections.

3.1 Combinatory Vessel Segmentation Method

There are numbers of methods available for vessel segmentation, but the existing methods often fail on images that contain high–density microvessels and background noise. The errors in the form of missing, undesired broken or incorrectly merged vessels eventually lead to poor segmentation results. This chapter addresses the first objective of the thesis by describing a state-of-art method designed for 3D microvessel segmentation. The method involves the combined use of two existing methods, line filter and Hessian–based vessel filter, to overcome the critical problems with these existing methods. The framework is effective in dealing with high–density vessels, including microvessels, and noise present in images. Full details on the implementation can be found in Section 8.4 and Section 8.7.

3.1.1 Methodology

In order to produce an accurate and robust segmentation method, both vessel enhancement and vessel detection should be taken into account. So the proposed method extends the 2D line filter [109] into a 3D line filter for enhancing 3D vessels, and the Hessian–based vessel filter is used for detecting the vessels.

The 2D line filter in [109] calculates, at each point in the image, the average intensity value I^w_{avg} within a neighbourhood of size $w \times w$ centred at the point. Intensity values of w points passing through the centre pixel along each of the $N(= 12)$ directions are summed, and the maximum average value $I^w_{\max}$ is kept. The line response at each pixel is then calculated using the following equation to generate a line response image:

$$R_w = I^w_{\max} - I^w_{avg} \tag{3.1}$$

The line response obtained is large at vessel voxels and low at background voxels.

It was observed that this line filter causes nearby vessels to merge or produce poor segmentation near crossover regions [126]. An improved 2D line filter calculates line response R_{lin} at each point as the average intensity of the original image and line response at different scales ranging from 1 to L, where L is the maximum scale value, I is the original image, and n is the number of scales used [126]. Normalisation is applied to the original image and images of line responses at different scales to improve vessel and background contrast.

$$R_{lin} = \frac{1}{n+1}\left(\sum_{w=1}^{L} R_w + I\right) \tag{3.2}$$

To extend the 2D line filter to 3D, average intensity values in 133 directions are calculated to produce the line response image. A directional mask image is shown in Figure 3.1.

The Hessian–based vessel filter obtains a vesselness measure at each point in the image. The Hessian matrix at the point is computed first. Eigenvectors of these matrices and their corresponding eigenvalues are then found, with λ_k representing the eigenvalue with the k^{th} smallest magnitude. For an ideal tubular structure, $|\lambda_1|$ is low and values for $|\lambda_2|$ and $|\lambda_3|$ are high. Three measures are used to describe the structures in an image:

$$R_A = \frac{|\lambda_2|}{|\lambda_3|}, \quad R_B = \frac{|\lambda_1|}{\sqrt{|\lambda_2\lambda_3|}}, \quad S = \sqrt{\sum_{j\leq 3} \lambda_j^2} \tag{3.3}$$

R_A distinguishes between plate-like and line-like structures, R_B accounts for the

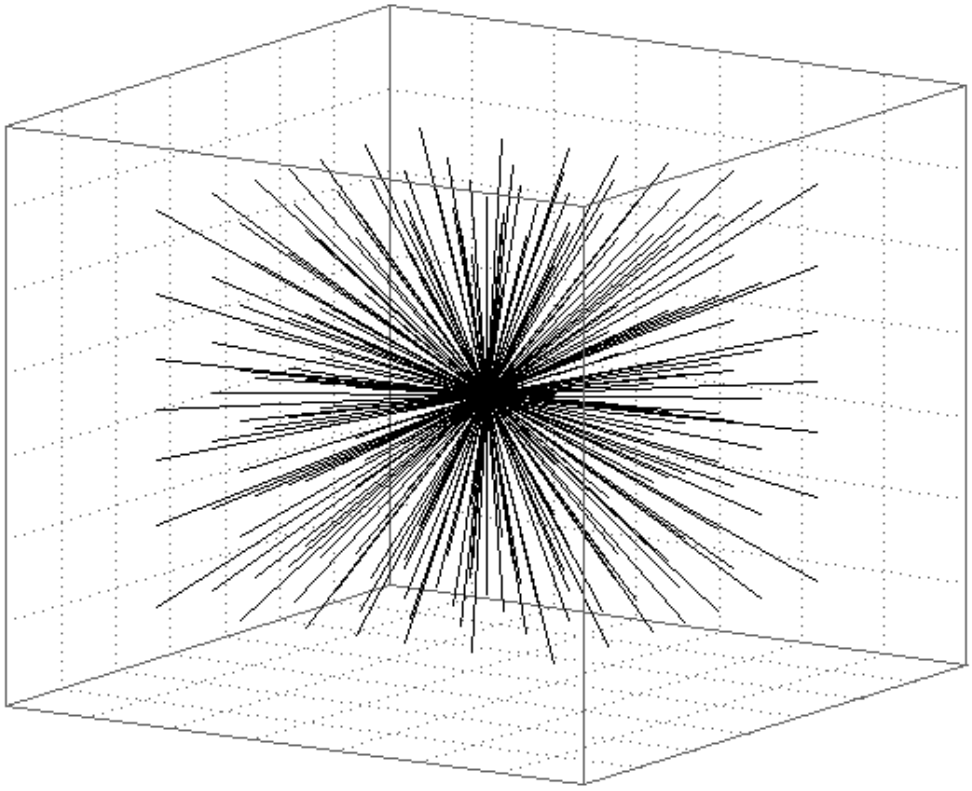


Figure 3.1: The directional mask used for the proposed method. An average intensity value of points within $7 \times 7 \times 7$ windows is computed. Average intensity values of all points passing through the centre point in 133 directions are compared and the maximal value is kept. Angular resolution is 15°.

deviation from a blob-like structure and S is defined to control the sensitivity of vesselness response to background noise. The vesselness function, V^L, can then be defined according to these measures to obtain probability-like estimates of each voxel, representing the likelihood of a voxel being a vessel point. If either $\lambda_2 = 0$ or $\lambda_3 = 0$ then $V^L = 0$, otherwise

$$V^L = (1 - G(R_A, \alpha))G(R_B, \beta)(1 - G(S, \gamma)) \tag{3.4}$$

$$G(a, b) = \exp\left(-\frac{a^2}{2b^2}\right)$$

Based on this, V^L is high for regions with high contrast and low otherwise. α, β, and γ are user-defined parameters to control the sensitivity of the vesselness measure to R_A, R_B, and S respectively. A final estimate of vesselness is then integrated with the responses at different scales L as vessels appear in varying scales. The line response image R_{lin} and vesselness response image V^L are then combined using element-wise multiplication to form the new framework:

$$R_{comb} = V^L \circ R_{lin} \tag{3.5}$$

Hysteresis thresholding is used to filter out noise from R_{comb}. It uses dual thresholding values, such that all voxels with values above the upper threshold value are first marked as vessel points, any neighbourhood voxel above the lower threshold that is connected to each of the first pass points are also classified as vessel. This produces segmentation with fewer isolated points, giving a better result than a simple high-pass threshold.

3.2 Microglial Segmentation Method

This section introduces an automated method for segmenting the microglia from histology images. The method includes the use of the fast split Bregman algorithm for image denoising and segmentation. The proposed method is accurate and scalable to large datasets and provides a useful tool for the study of microglial biology. Full details on the implementation can be found in Section 8.8.

3.2.1 Methodology

Noise is inherent in histology images. Research for quantitative analysis of microglia often relies on thresholding (manual or automatically) [54, 55, 127]. The methods are unrealisable and are not suitable for dealing with inhomogeneous histology images of the microglia. A pre-processing step is therefore needed to remove noise and simultaneously preserve the details of microglia in the images.

As such, a weak smoothing ($\alpha = 10$) and a strong smoothing ($\alpha = 300$) are applied to the greyscale image for microglia processes and soma segmentation respectively. An adaptive thresholding algorithm, which automatically determines threshold values for different parts of the image, is then applied to the denoised images to extract the microglia. Tiny microglia with a soma size smaller than 16.7μm are also removed, as suggested in [54]. In Alzheimer's disease, microglia with the morphological appearance of activated phenotype clusters are found around amyloid plaques [128]. These clusters are detected by their abnormal soma sizes and analysed separately. Finally, the segmented microglia processes are skeletonised and combined with the segmented microglia soma, and the isolated microglial processes that are not connected to any microglia soma are removed.

Having introduced the workflow of the framework, the following section will briefly introduce the smoothing method used in this work.

3.2.1.1 Mumford-Shah Total Variation

Previous study in [49] proposed a method that uses a nonlocal total variational model to denoise the image, and the method performed well and achieved significant segmentation accuracy. However, it has been found that using a nonlocal total variational model for image processing is slow and is not scalable to large datasets [129]. The classical variational Mumford-Shah model that uses a total variation regulariser (called the MSTV model in this thesis) [56, 57] is two times faster and therefore was chosen for the proposed method. The MSTV model works as follows [130]:

$$\begin{aligned} E_\varepsilon(u,v) = \int_\Omega (u-f)^2 dx \\ + \alpha \int_\Omega v^2 \left|\nabla u\right| dx \\ + \beta \int_\Omega \left(\varepsilon |\nabla v|^2 + \frac{(v-1)^2}{4\varepsilon} \right) dx \end{aligned} \quad (3.6)$$

where α, β, and ε are three positive tuning parameters balancing the energy terms, u is a piecewise smooth function to approximate the original image f, and v is a piecewise smooth function to represent object edges in the image (v takes the value 0 on the edge sets and 1 in smooth regions). This energy functional can be used to smooth the image as well as find the edges of objects in the image.

A fast split Bregman algorithm [58] is designed for discretising and solving the MSTV model equations. By introducing an auxiliary vector variable $w = (w_1, w_2)$ and a Bregman iteration parameter $b = (b_1, b_2)$, the minimisation of the MSTV

model can be transformed into optimising following energy functional:

$$E_{\varepsilon}(u,v,w) = \int_{\Omega}(u-f)^2 dx + \alpha\int_{\Omega} v^2|w|\,dx + \frac{\theta}{2}\int_{\Omega}(w-\nabla u-b)^2 dx + \beta\int_{\Omega}\left(\varepsilon|\nabla v|^2 + \frac{(v-1)^2}{4\varepsilon}\right)dx \quad (3.7)$$

where θ is a positive penalty parameter. In practice, each variable u, w, and v in functional (3.7) is solved separately, e.g. variables v and w are fixed first, and the Euler equation of u is solved as follows:

$$u + \theta\Delta u = f + \theta div\left(w^k - b^k\right) \quad (3.8)$$

where div and Δ denote divergence operator and Laplace operator respectively, and k stands for the current number of iterations. This linear system can be efficiently solved using the fast Fourier transform. By applying the discrete Fourier transform to both sides of the equation, the closed-form solution of u is obtained:

$$u = \Re\left(FFT^{-1}\left(\frac{FFT(f) + \theta FFT(div)\,FFT\left(w^k - b^k\right)}{1 + \theta FFT(\Delta)}\right)\right) \quad (3.9)$$

where $FFT(\cdot)$ and $FFT^{-1}(\cdot)$ denotes the discrete Fourier transform and inverse Fourier transform respectively. the $\Re(\cdot)$ is the real part of a complex number, and $'-'$ stands for pointwise division of matrices.

The minimisation with respect to w can be expressed as follows:

$$w^{k+1} = \underset{w \in R^4}{\operatorname{argmin}} \left\{ E(w) = \alpha \int_\Omega v^2 |w| \, dx + \frac{\theta}{2} \int_\Omega (w - \nabla u - b)^2 dx \right\} \quad (3.10)$$

It is easy to check that,

$$w^{k+1} = \max\left(\left| \nabla u^{k+1} + b^k \right| - \frac{\alpha}{\theta} v^2, 0 \right) \frac{\nabla u^{k+1} + b^k}{\left| \nabla u^{k+1} + b^k \right|} \quad (3.11)$$

with the convention that $0/0 = 0$, The above equation is known as the analytical soft thresholding equation or shrinkage. Note that shrinkage (3.8) includes two subshrinkages for each component of vector w.

The solution of the Euler-Lagrange equation of v with the u and w fixed is obtained as follows:

$$2\alpha v \left| w^{k+1} \right| - 2\beta\varepsilon\Delta v + \beta \frac{(v-1)}{2\varepsilon} = 0 \quad (3.12)$$

This equation can be efficiently solved by one iteration of Gauss-Seidel. Finally, the parameter is updated using

$$b^{k+1} = b^k + \nabla u^{k+1} - w^{k+1} \quad (3.13)$$

3.3 Fractal Feature Extraction Method

Recall that in Section 2.2.1 we explained that there has been published research using fractal analysis to calculate fractal dimensions of retinal blood vessels. However, so far there has been no systematic research extracting discriminant features from retinal vessels for classification. This chapter introduces new methods for feature extraction from multifractal spectra of retinal vessels. The method has also been found useful for classification of microglial cells. Full details on the implementation can be found in Section 8.9.

3.3.1 Methodology

Retinal vessels typically exhibit fractal properties in their appearance, displaying self-similarity at multiple scales [30]. Fractal analysis can therefore be used in the analysis of retinal vessel structures. A major concept in fractality is the fractal dimension, D, which describes how the complexity changes over a scale of measurements. The fractal dimension can be defined in a variety of ways, based on how the scaling law is determined. One simple example of this is to use a method called box-counting – a box of some (small) size s is placed over a point on the structure and the number of valid pixels contained within the box is counted, described as the mass $M(s)$. The scaling law between mass and scale is $M(s)/M(L) \sim (s/L)^{-D}$, where D is the non-integer fractal dimension, and L is the dimension of the smallest bounding box that contains the entire structure.

Rather than calculating a single (mono)fractal dimension, multifractal analysis can be used to produce a spectrum of dimensions, $D(h)$. This spectrum represents fractal dimension as a function of the Hölder exponent, a measure of irregularity

for a given point [32]. In the literature, the approximated Hölder exponent is typically denoted by α and the estimated multifractal spectrum $f(\alpha)$. In practice, the relationship of α and $f(\alpha)$ is calculated using the box-counting scaling law and some set of power values Q. To get an approximately complete coverage of the structure, the scaling is estimated across a large number, N, of random box locations:

$$\sum_{i=1}^{N} \left(\frac{M_i(s)}{M(L)} \right)^q \sim \left(\frac{s}{L} \right)^{(q-1)D_q} \tag{3.14}$$

where $q \in Q$ and $M_i(s)$ is the mass in a box of size s, centred in the i^{th} box location. Values for $f(\alpha)$ are calculated using the Legendre transform of $\alpha(q)$ using the following set of equations:

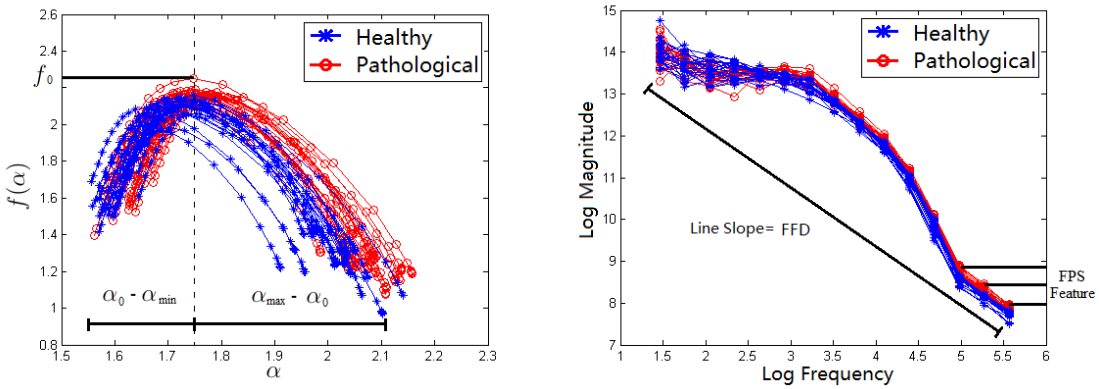
$$\tau(q) = (q-1)D_q \tag{3.15}$$

$$\alpha(q) = \frac{\mathrm{d}\tau}{\mathrm{d}q} \tag{3.16}$$

$$f(\alpha) = q\alpha(q) - \tau(q) \tag{3.17}$$

Orientation invariant is one of the advantages of multifractal analysis, as the same structure may appear in different orientations in images, and image analysis methods should be robust to these orientation variations.

In general, the more complex the structure, the larger the fractal dimensions and the wider the range of Hölder exponents α. This corresponds to a wider multifractal spectrum. The spectrum may be skewed, or exhibit symmetry, based on the relation between $(\max(\alpha) - \alpha(0))$ and $(\alpha(0) - \min(\alpha))$. Where $q = 0$, $f(\alpha)$ represents the box-counting (mono)fractal dimension, which occurs as the peak in a multifractal spectrum. Full details on the implementation and symmetry analysis can be found at [32].



(a) (b)

Figure 3.2: Multifractal analysis of 20 healthy and 20 pathological (background diabetic retinopathy) retinal vasculatures from STARE: (a) $\alpha/f(\alpha)$ spectra of vasculatures automatically segmented by the combinatory vessel filter; (b) Fourier power spectra of vasculature automatically segmented by the combinatory vessel filter. The extracted features are labelled on the plots.

Figure 3.2 shows an example of multifractal spectra of retinal vasculature that has been automatically segmented using the combinatory vessel filter on images from the STATE dataset. The multifractal spectra of vasculature with diabetic retinopathy has previously been found to differ from those of healthy vessels [31, 32], as demonstrated in Figure 3.2a. Certain characteristics cannot be easily discriminated between healthy and pathological spectra, suggesting that the multifractal features alone are not sufficient to completely describe local variations in the vasculature. To improve classification accuracy, further information about the vessels in the images is needed.

Recall that when calculating fractal dimension using the box-counting method, the number of boxes N needed to cover a structure, and the size s of the box to obey the power law; then the fractal dimension is the slope of the log-log plot $log(N)$ on the y-axis against $log(s)$ on the x-axis. A steeper slope means that the structure is more complex. According to [131], the Fourier power spectrum (FPS)

of a greyscale image and spatial frequency (f) also obey the power law. This provides another way to calculate fractal dimension, using the Fourier transform. The Fourier fractal dimension (FFD) can be defined as the slope of the log-log plot of $log(FPS)$ on the y-axis against $log(f)$ on the x-axis. In practice, the Fourier fractal dimension (FFD) is defined as [131]:

$$FFD = \frac{6+\beta}{2} \tag{3.18}$$

where β is the slope of the least square line fitted to the Fourier power spectrum in the log-log scale.

Example plots of $log(FPS)$ of images against $log(f)$ are shown in Figure 3.2b. The power spectrum and slope plots of the two classes become separated at the end of the spectra. It can be seen that the power spectra and the slope plots of the pathological vasculature are also different from those of healthy vasculature. This is because binary vasculature images are used for the experiments and the Fourier power spectra and spatial frequency slightly deviate from the power law. This has also been reported in [132]. However, the plots of healthy and pathological retinal vascular images are still quite distinct, especially at high frequencies.

In summary, within this chapter, the features extracted from the vasculature for classification are the multifractal features (the peak of the multifractal spectrum (f_0) and the symmetry features $\alpha_{\max} - \alpha_0$ and $\alpha_0 - \alpha_{\min}$), as well as the Fourier features (FFD and the FPS magnitude values at high frequencies); the corresponding features are labelled in Figure 3.2 and these features together are called the combinatory feature.

3.4 Summary

In this chapter, a novel method for 3D brain vessel segmentation has first been proposed that combines a line filter and a Hessian–based vessel filter. Then, an automated method is introduced for segmenting the microglia from histology images. In the last section, methods for extract features from multifractal spectra and from Fourier power spectra of an image for classifying was introduced.

The next chapters present three case studies on real medical images, using the proposed methods introduced in this chapter, including 3D vascular images, 2D retinal images, and microglial histology data. The results presented here show that the proposed segmentation methods and fractal feature extraction method can be potentially used as a viable tool for investigating things such as vascular development and pathology to complement conventional clinical assessment, as well as for studying microglial biology.

Chapter 4

Case Study 1: 3D Vascular Data

A main weakness in vascular research is considered to be the lack of computational tools for 3D quantification of microvasculature. Well known vessel segmentations have been mostly developed for detecting large vessels for cardiovascular disease from magnetic resonance angiography (MRA) or computed tomography angiography (CTA) images and those often involve the use of contrast agents [15, 16]. Micro-CT can achieve resolutions on the order of several μm, allowing imaging the 3D microvasculature down to the capillary level. This section demonstrates the strength of the proposed methods by presenting experimental results of vessel segmentation, vessel size visualisation, and vessel fractal feature extraction on both 3D synthetic vascular data and real vascular data, including Micro-CT rat, monkey and MRI human brains. The flowchart of this chapter can be viewed in Figure 4.1.

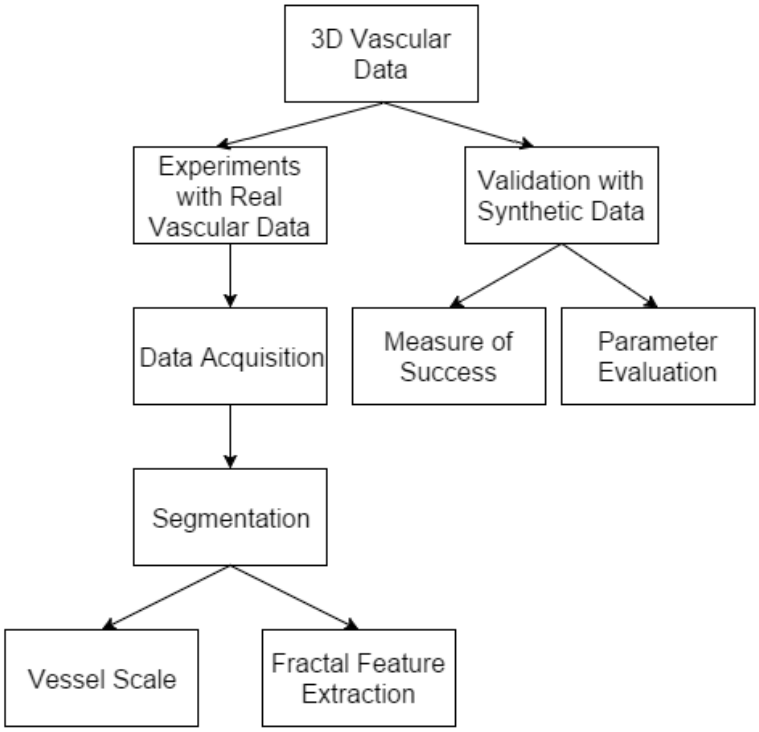


Figure 4.1: Flowchart of case study 1.

4.1 Data Acquisition

The rat brain images named C2, F2, J2, and L0, and the monkey brain image were obtained using micro-CT (CT) imaging of resin-cast models obtained by the following methods [6]. First, the animal was lightly fixated in 4% paraformaldehyde at 120 mmHg transcardiac perfusion. Fluorescent PN4 resin was then delivered via syringe. Brains were removed after 48 hours curing and macerated in a 10% KOH solution for 2 weeks at 37°C. The resin casts were washed in DDH_2O, immersed in 2% Os04 for 3 days and freeze dried. These were then mounted, staged and scanned using in a CT imager at 40kV, with a current of 800A. The voxel resolution was 24μm.

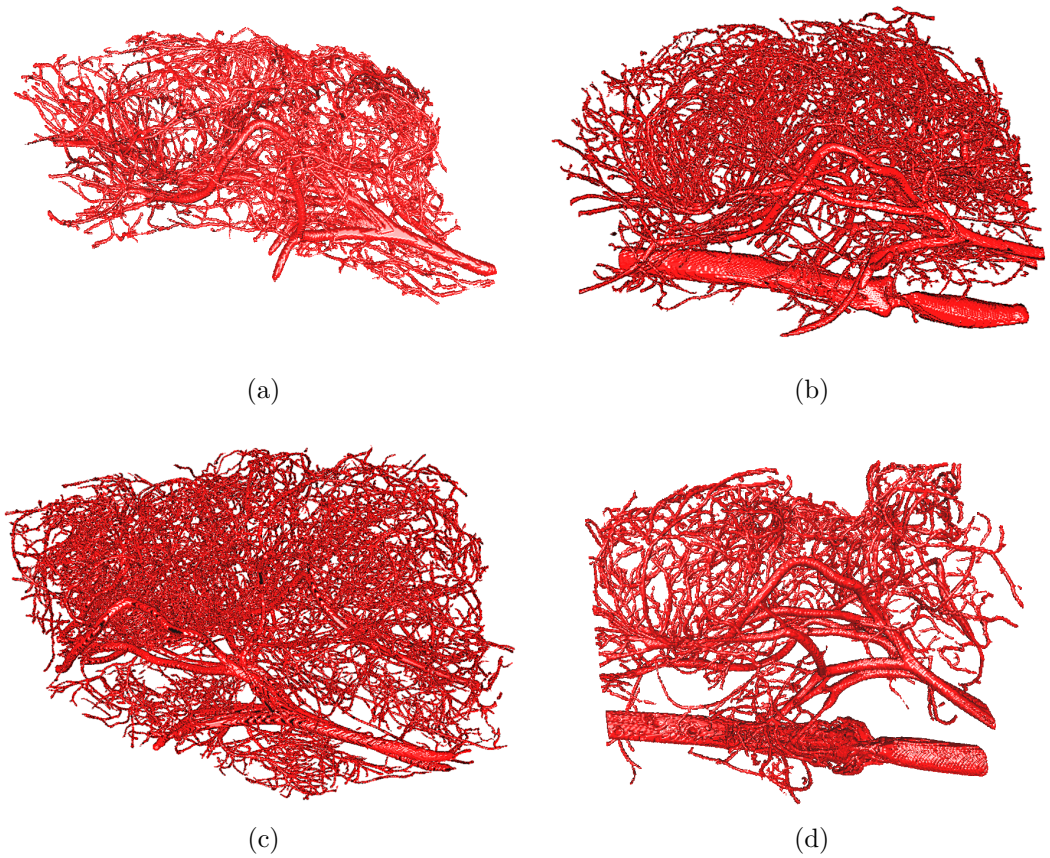
The human brain images, named with the prefix 'Head', and numbered 4–9, were obtained from 7T MRI scans. The images are T2*-ffe (fast field echo) weighted images, which have phase data associated with them [133]. The phase data is turned into susceptibility maps to get QSM (quantitative susceptibility mapping), which is then combined with T2* to get the images used in this chapter. The technique allows for high-resolution visualisation of both cerebral veins and arteries in one sequence without application of contrast agent. Ethics approval for these images was obtained from the ethics committee of the University of Nottingham Medical School, and all subjects gave informed consent.

4.2 Segmentation

The proposed method from Chapter 3.1 was applied to the three brain datasets. The 3D rendered segmentation of rat, monkey, and human brains are shown in Figures 4.2, 4.3, and 4.4 respectively. Since there is no ground truth available for the brain models to obtain quantitative analysis, selected results using the line filter, Hessian–based vessel filter, and the proposed method are compared in Figure 4.5 and 4.8, together with the selected cross section images for each of these two images which are shown in Figure 4.6 and Figure 4.7), to demonstrate the strength of the proposed method. Three corresponding areas are labelled in each segmentation. The green label in Figure 4.5b shows falsely merged vessels, a common issue with the Hessian–based filter. The blue labels show that segmentation noise was produced at vessel bifurcation and crossover regions when using the individual methods, whereas the proposed method gave largely clear vessels. The orange labels show that the methods involving the line filter have correctly revealed small and faint vessels, although the segmentation is noisy, using only the basic line filter. The MR images contain higher noise levels, and as a result, there is a larger amount of structure segmented by original vessel filters, especially in the centre of the images. As shown by the testing, the proposed method handles this noise better. Note that the line filter has segmented areas at the front of the human model (Figure 4.5a), which correspond to skull structure but are misclassified as vessels.

When applied to the brain data, parameter values for the proposed method were set to $\alpha = 0.25$ and $\beta = 0.5$, with γ, which is used to deal with image noise, set to 500, as suggested in [19].

Vessels in micro-CT images are much clearer due to the resin casting process, so



(a) (b)

(c) (d)

Figure 4.2: 3D rendered images of rat brain microvasculature obtained from imaging resin-cast models using micro-CT scanner segmented with the proposed method. Samples are named (a) C2, (b) F2, (c) L0, and (d) J2.

there is little noise in the data. Better vessel detection can be seen for the proposed method over the other two, notably in the identified regions of Figure 4.8. Results show that all the methods perform well on detecting large vessels. However, all three labels show that the line filter produced significant numbers of missing and undesired broken vessels. The vesselness filter detected many more vessels, but slightly less than how much the proposed method has detected.

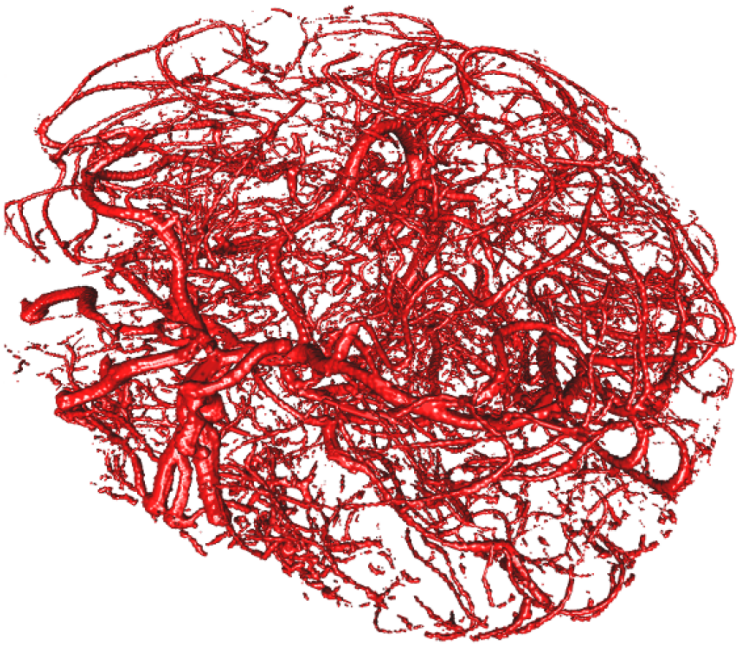
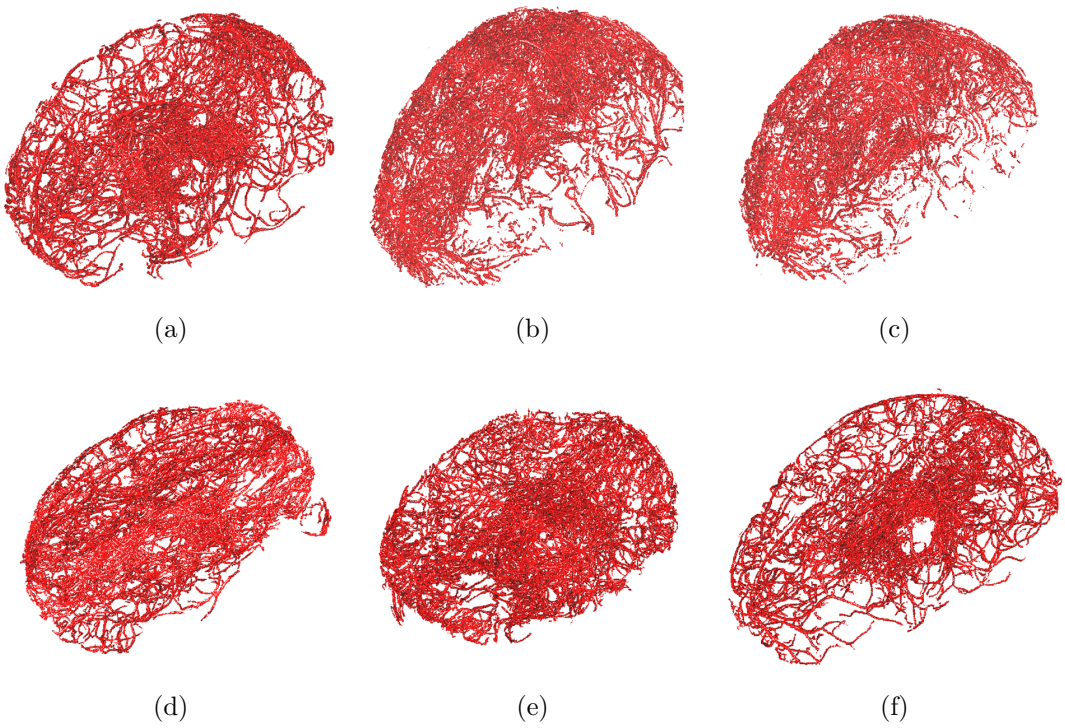


Figure 4.3: 3D rendered images of monkey brain microvasculature obtained from imaging resin-cast models using a micro-CT scanner segmented with the proposed method.

4.2.1 Vessel Scale

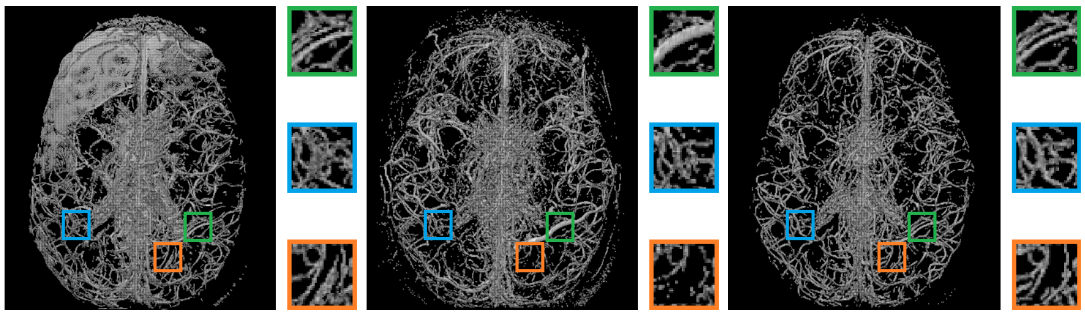
Window size $W = 3$ and scales $L = \{1, 3\}$ were used for segmenting the human brain datasets, and $L = \{1, 3, 5, 9\}$ were selected for the rat brains by visual inspection. The scale parameter L can also be used to separate vessels of different thickness. Figure 4.9a shows the whole segmented rat brain vasculature. Figures 4.9b–d are segmentations using different sets of scales: $L = \{3, 5, 9\}$, $L = \{3, 5\}$, and $L = \{9\}$ respectively. Figure 4.10 shows the vessel thickness corresponding to Figure 4.9a-c, created using Fiji plugin in ImageJ. The colour scheme indicates vessel diameter [134]. Based on the scanning information, the thickest value in the scale 24 is equivalent to 2.4mm.



(a) (b) (c)

(d) (e) (f)

Figure 4.4: 3D rendered images of human in-vivo brain vasculature obtained through segmenting 7T MRI images with the proposed method. Samples are named: (a) Head 4, (b) Head 5, (c) Head 6, (d)Head 7, (e)Head 8, and (f) Head 9.



(a) (b) (c)

Figure 4.5: Screenshots taken along the x-axis from the segmentation of Head 4 using (a) the line filter, (b) the Hessian–based filter, and (c) the proposed method.

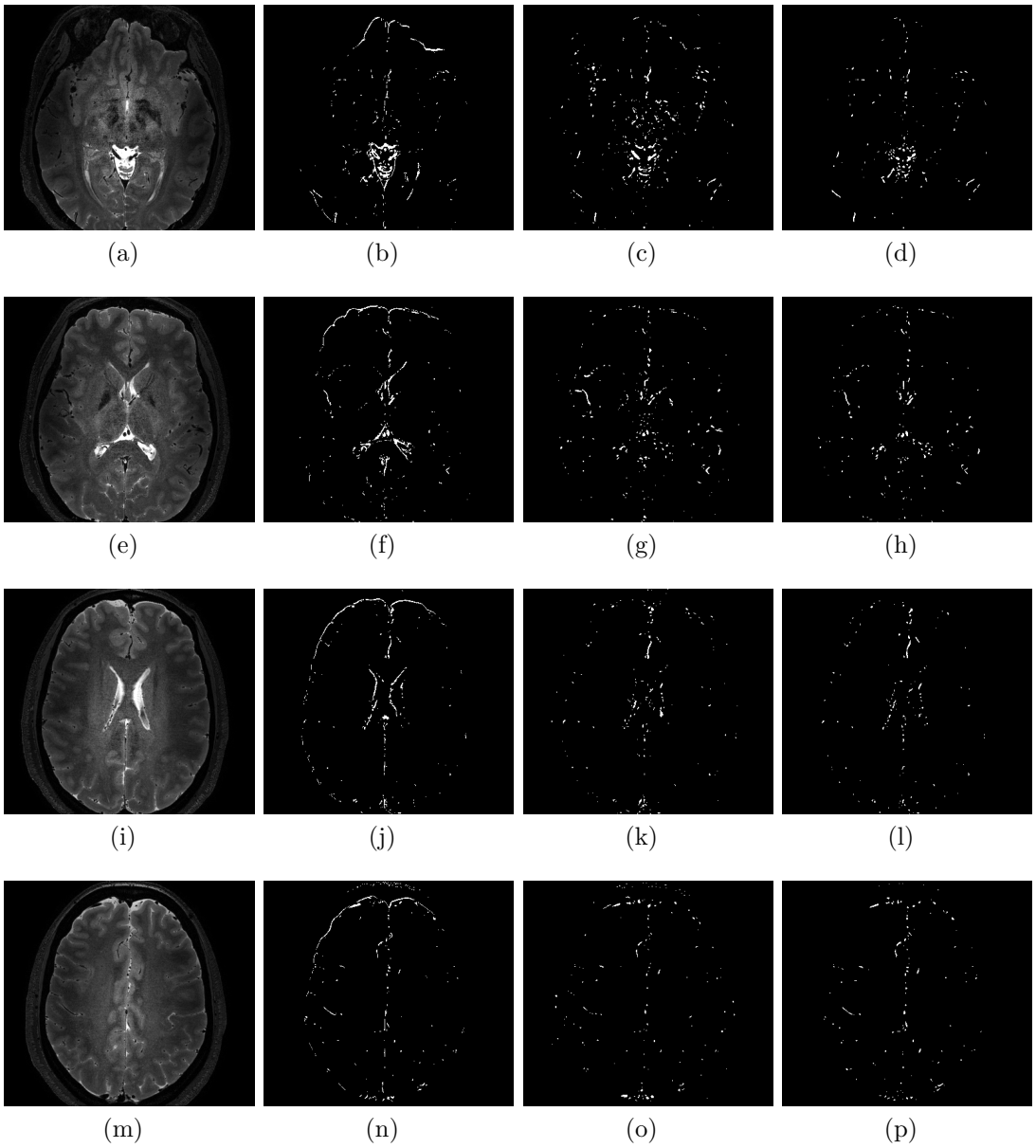


Figure 4.6: Selected cross-sections of segmentation of Head 4. (first column) The original image, (second column) the line filter, (third column) the Hessian–based filter, and (forth column) the proposed method.

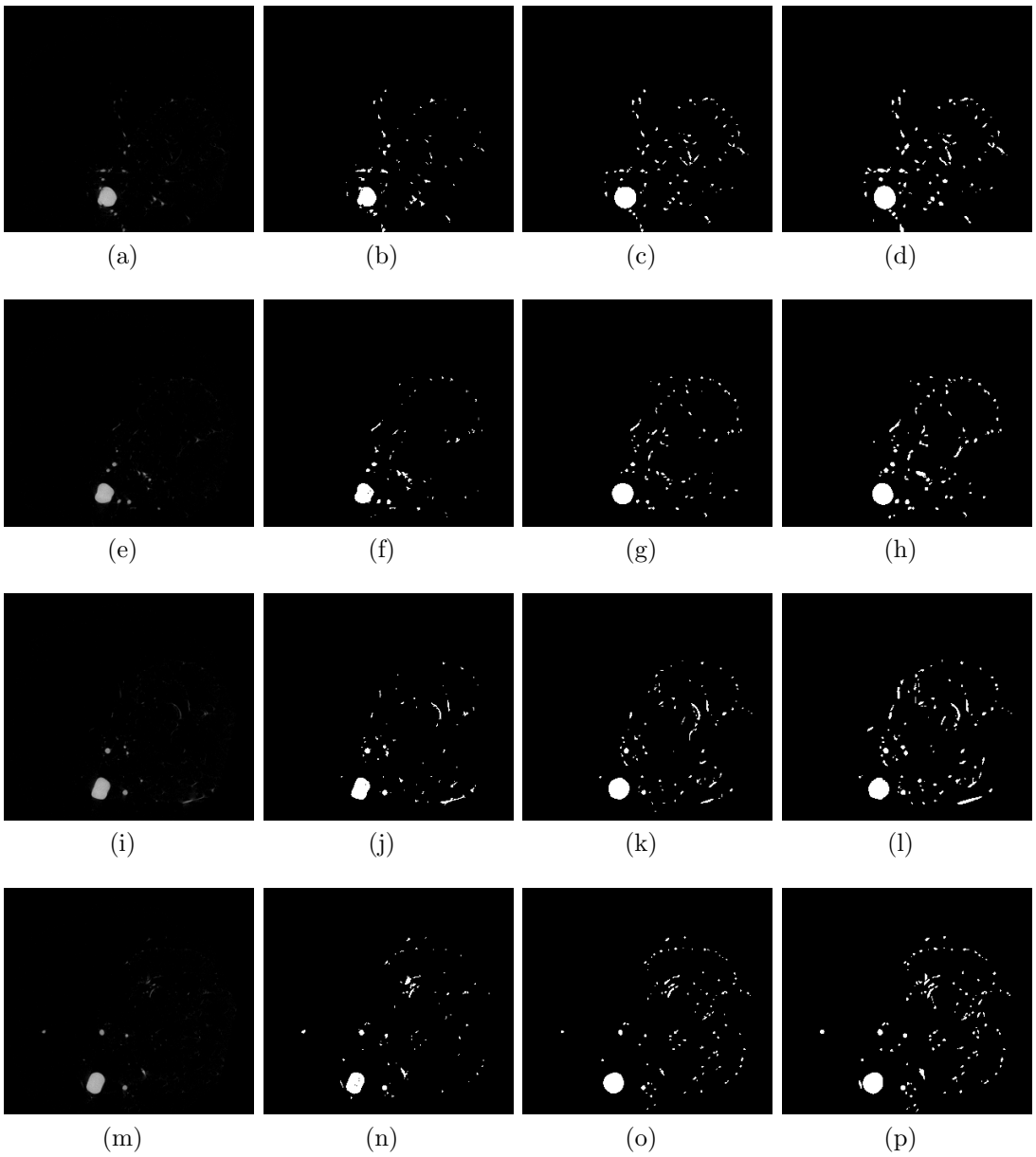
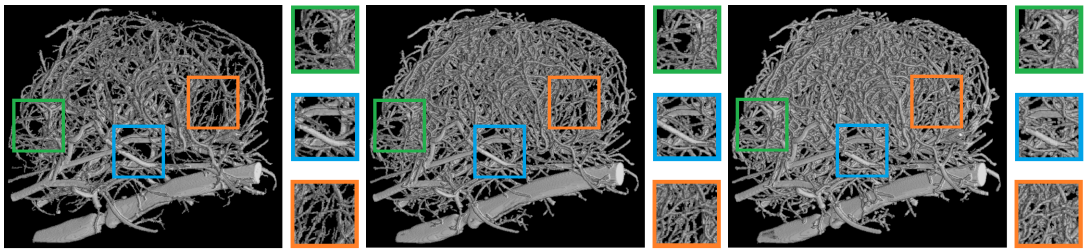
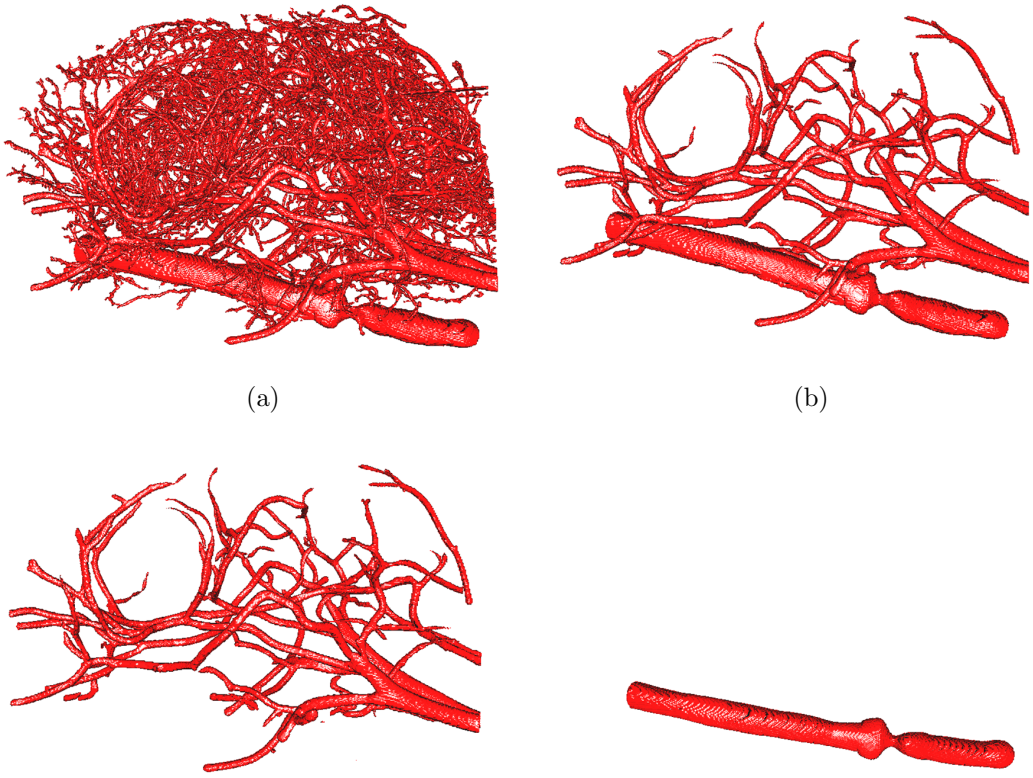


Figure 4.7: Selected cross-sections of segmentation of Rat F2. (first column) The original image, (second column) the line filter, (third column) the Hessian–based filter, and (forth column) the proposed method.



(a) (b) (c)

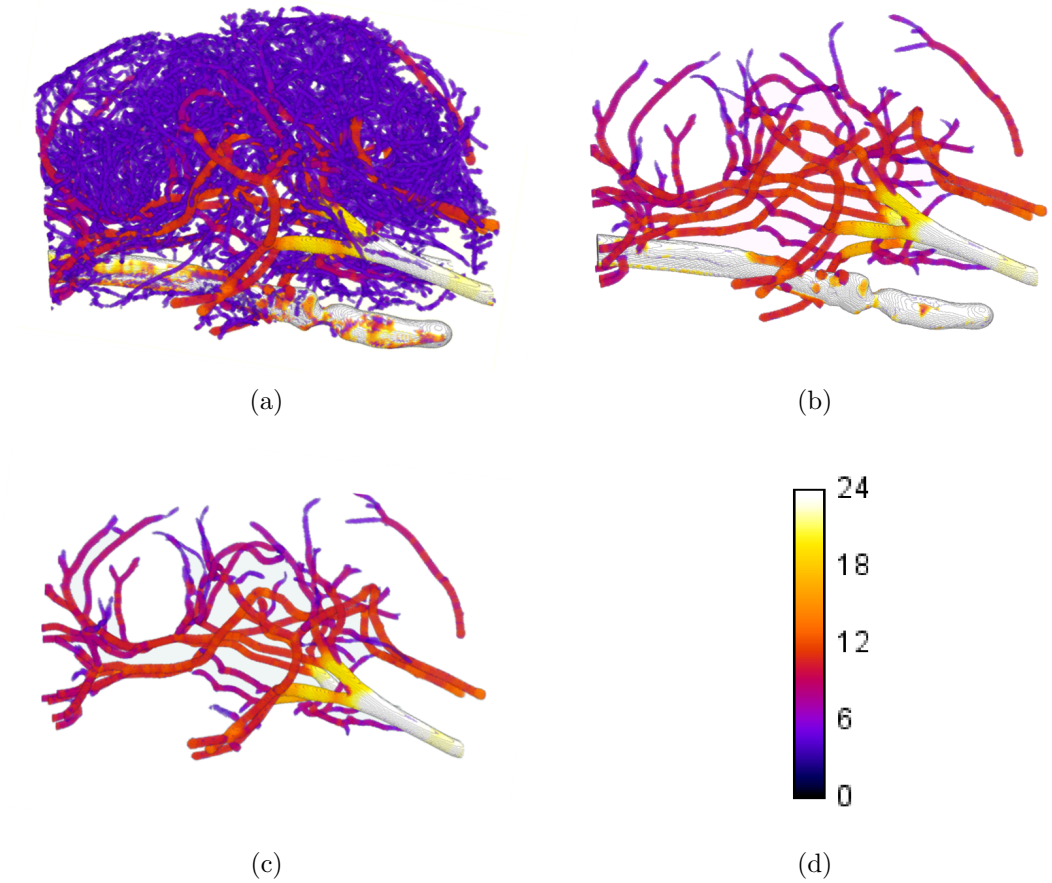
Figure 4.8: Screenshots of segmentation of Rat F2 using (a) the line filter, (b) the Hessian–based filter, and (c) the proposed method.



(a) (b)

(c) (d)

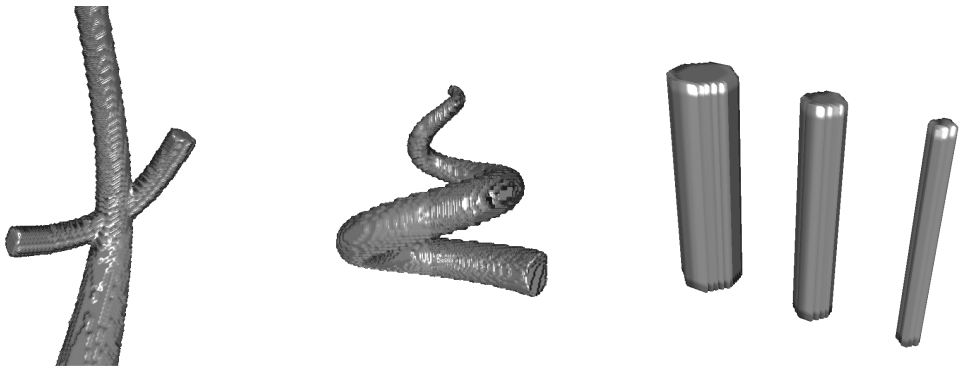
Figure 4.9: Rat brain F2 vessel separation based on scale values in the proposed method. Each subplot shows vessels segmented using scales (a) $\{1, 3, 5, 9\}$, (b) $\{3, 5, 9\}$, (c) $\{3, 5\}$, and (d) a single scale $\{9\}$.



(a) (b)

(c) (d)

Figure 4.10: Vessel thickness visualisation of the segmented rat brain F2 using different scales, corresponding to Figures 4.9(a)-(c), using Fiji plugin in ImageJ. The calibration bar (d) indicates the thickness of the vasculature where 24 is equivalent to 2.4mm based on the scanning resolution.



(a) (b) (c)

Figure 4.11: 3D synthetic models created for experiments (a) branch (b) spiral (c) columns.

4.3 Validation with Synthetic Vascular Data

In order to quantify the effectiveness of the proposed methods from Section 3.1, three synthetic vessel-like models were created, each with different structural properties that are characteristic of the true vasculature. Each model had dimension $100 \times 100 \times 100$ and 'vessel' diameters are given in millimetres, assuming that the model resolution is equal to that of the micro-CT data (10 voxels per mm).

The first image is a branching structure, with two tubular structures intersecting approximately 90° in 3D space, one with constant radius of 0.84mm and the other with a varying radius ranging from 1.7mm to 0.97mm. The second is a tubular structure of increasing diameter (0.2 – 1.8mm) in the form of a logarithmic spiral. The final model is formed of three simple vertical cylinders with different diameters, 1.1mm, 0.7mm, and 0.4mm. This was created to model complex vascular structures typically seen in an image. These are shown in Figure 4.11.

Gaussian noise was applied to these images, informed by the fact that Gaussian noise is typically present in MR images [135]. The noise levels applied are given as signal-to-noise ratio (SNR) in decibels, ranging from -56dB to -80dB. Decreasing

SNR indicates increased noise.

4.3.1 Measures of Success

Similarity measures are defined to demonstrate the effectiveness of the proposed method and compare it with the existing method. Three commonly used measures of success are sensitivity, specificity, and accuracy. Sensitivity is the rate of successful vessel detection. Specificity is the rate of voxels correctly labelled as background. Accuracy is calculated as a degree of 'closeness' between the segmentation and the ground-truth. Specifically, let P and N be respectively the number of actually positive voxels (i.e. vessel voxels) and actually negative voxels (non-vessel voxels) in the volume, and let TP be those positive voxels identified as vessel voxels by the algorithms and let TN be those negative voxels identified as non-vessel voxels by the algorithms. Let FP and FN be false positives (voxels correctly identified as vessels) and false negatives (voxels incorrectly identified as non-vessels) respectively, then:

$$\begin{aligned} \text{sensitivity} &= TP/P \\ \text{specificity} &= TN/N \\ \text{accuracy} &= (TP+TN)/(P+N) \end{aligned}$$

Additional measures of success were also considered, including the Jaccard similarity coefficient $TP/(TP+FP+TN)$, which looks at the ratio of similarity and diversity between segmentation and model; the root-mean-square error (RMSE), measuring the variance of differences between result and truth, defined as RMSE $= \sqrt{(FP+FN)/(P+N)}$; and Cohen's κ coefficient.

The κ coefficient is the measure of closeness between the segmentation result

and the ground truth, and takes into account success occurring by chance. There are two components that make up the value of κ. The first, relative observed agreement, is defined as the accuracy $P(a) = (TP + TN)/(P + N)$. The hypothetical likelihood of a random agreement is described as

$$P(e) = \left(\frac{TP + FP}{P + N}\right)\left(\frac{TP + FN}{P + N}\right) + \left(1 - \frac{TP + FP}{P + N}\right)\left(1 - \frac{TP + FN}{P + N}\right)$$

Removing the weight of successful segmentation by chance in similarity comparison, the κ coefficient is given as: $\kappa = (P(a) - P(e))/(1 - P(e))$.

In all the similarity measures above, except RMSE, the values lie between 0 and 1, with 1 being the perfect score and 0 showing absolute failure. In the case of RMSE, the smallest value is the best result.

Finally, the receiver operating characteristic (ROC) curve can be plotted to visualise the effect of different thresholds and parameters on the segmentation results. The sensitivity for each result is plotted against the value of (1−specificity). The plot begins at $(0, 0)$ and as the sensitivity increases, the specificity is expected to decrease, leading to a convex curve terminating at $(1, 1)$. The closer the curve passes to $(0, 1)$ is an indication of the method's success and its handling of parameter changes. A means for interpreting and quantifying this curve is to calculate the area under the curve (AUC), which will fall between 0 and 1, as with the other similarity measures.

Figure 4.12 gives, for each of the nine experiments, plots of sensitivity, specificity, Jaccard index, and Cohen's κ against increasing levels of noise. The results clearly show the outperformance of the proposed method over the existing methods in all cases, with the difference in results becoming more significant at higher levels of noise. For the proposed method, the segmentation fails completely

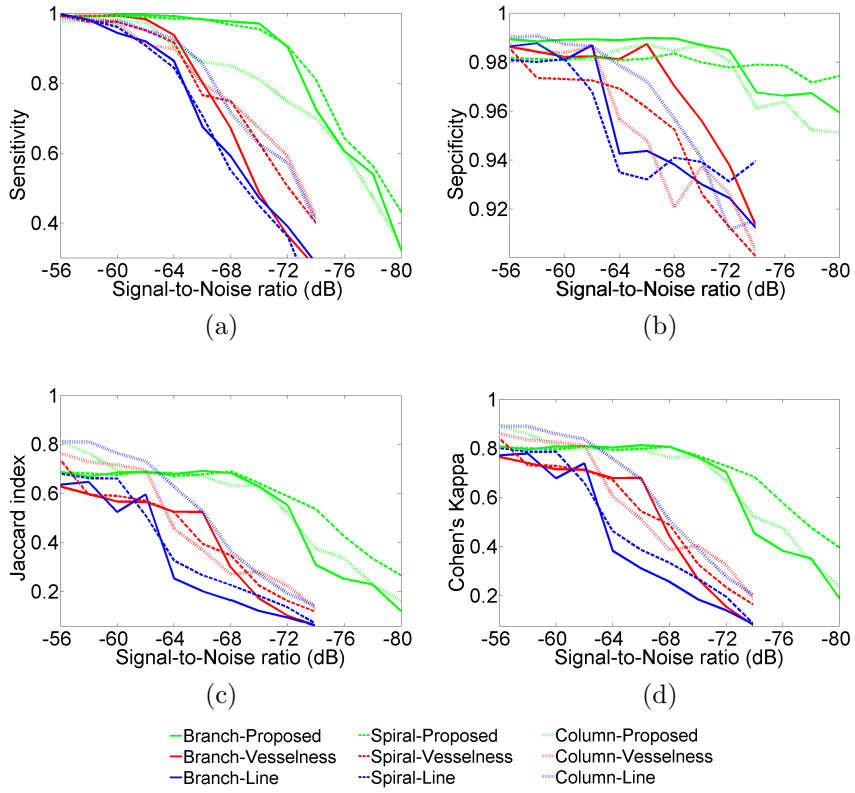
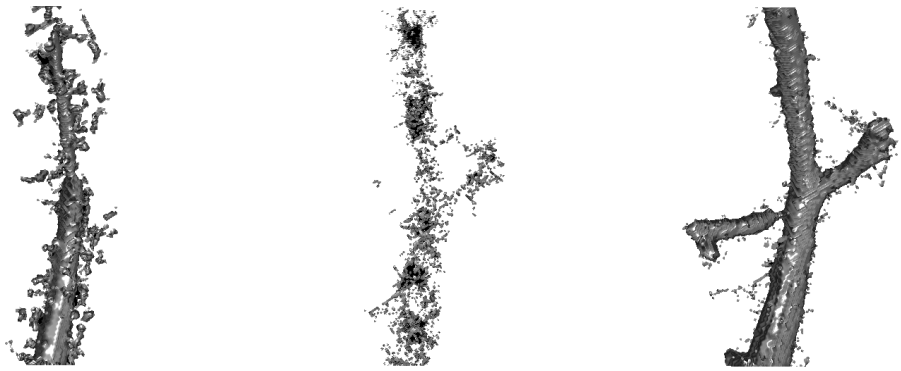


Figure 4.12: Plots of (a) sensitivity (b) specificity (c) Jaccard index (d) Cohen's kappa, for the different methods applied to each synthetic model for the full range of tested noise levels.

for SNR values less than -80dB. For the vesselness filter and line filter tests, the segmentations on all models failed when SNR fell below -74dB.

Figure 4.13 shows the result of each method on the branch model, showing clear distinction in the quality of segmentation. The values for κ in all models segmented with the proposed method remain relatively stable and consistently higher than the results for the other segmentation methods. Jaccard's similarity coefficient also shows consistently better values for the proposed method, especially at high levels of noise.

Accuracy and RMSE results are provided in Tables 4.1, 4.2, and 4.3. Results here show that the performance of the three methods are high at low SNR with



(a) (b) (c)

Figure 4.13: Segmentation results of the branch model, with -74dB Gaussian noise SNR, using (a) vessel filter (b) line filter, and (c) the proposed method.

little error produced. The performance of the line filter decreases rapidly at SNR below around -62dB in the branch and spiral models, but remains consistent for increased noise in the column model, until SNR reaches -66dB. Conversely, the vesselness filter performs poorly after –62dB in the column model, but is higher for the other models until -66dB. This is indicative of the line filter's better capabilities for detecting line structures, and the effectiveness of the vesselness filter on more complex structures. The proposed method incorporates the advantages of both methods and the error is low in all three models until the models become significantly noisy, approximately -74dB.

The corresponding box plots are shown in Figure 4.14. From these results we can see that the proposed method performs consistently better, with higher accuracy and low errors even at greater levels of SNR. The box plots show that there is little variation in performance across the modelled structure types, and that even in the worst case scenario the proposed method yields lower errors than the average performance of the existing methods.

It is also possible to see the quality of performance by the vesselness and line filters with respect to each other on each model. For the curved models (spiral

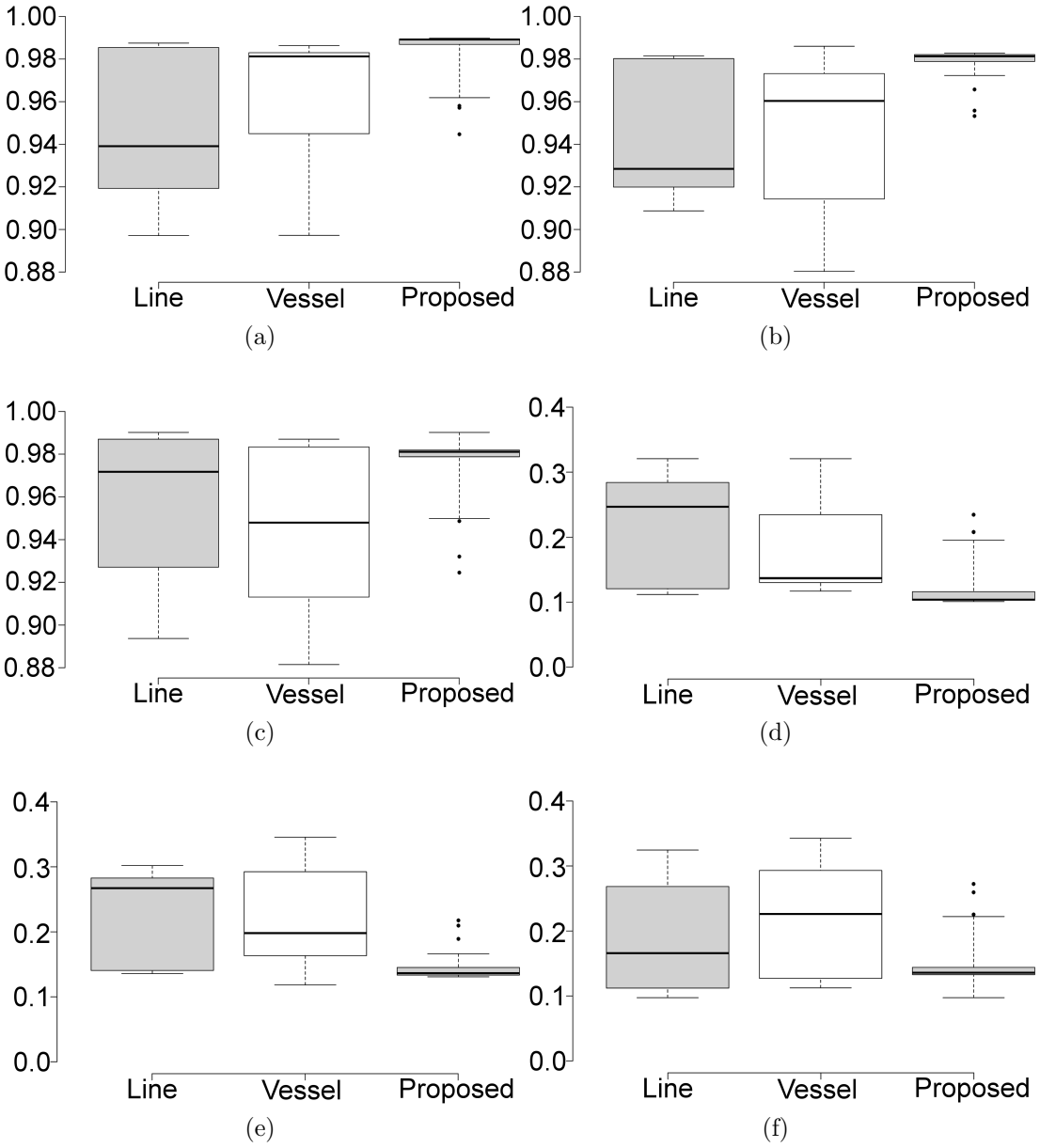


Figure 4.14: Box plot comparison of three methods on each synthetic model. Top row: accuracy for (a) branch model, (b) spiral model, and (c) column model. Bottom row: RMSE for (d) branch model, (e) spiral model, and (f) column model. Black points represent values for models with SNR below -74dB

and branch), the vesselness filter has higher median results, but for the synthetic column image, the line detector method handles segmentation and noise better. Considering the combinatorial nature of our proposed method, the respective pitfalls of the previous methods are mediated or eliminated.

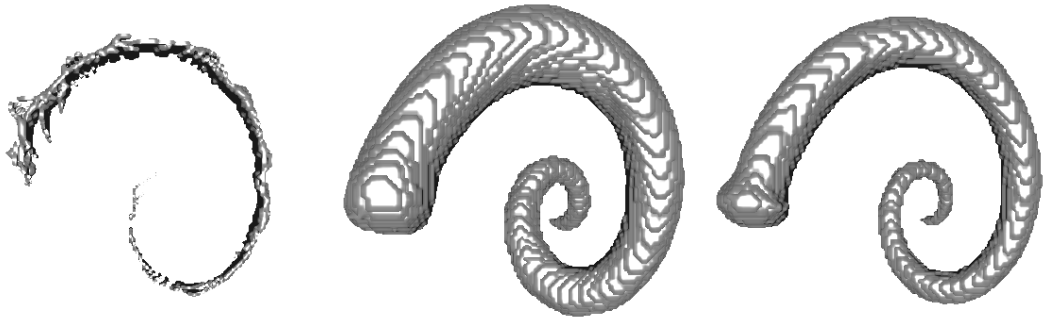
4.3.2 Parameters

This section aims to shed some light on the effect of the control parameters (α, β, and γ) in (3.4) of Section 3.1, as well as the hysteresis thresholds used in the proposed algorithm on the segmentation.

A vascular model containing a binary spiral, shown in Figure 4.11b, is used for testing the effect of α and β on the segmentation. Figure 4.15a shows the segmentation result using the original vesselness filter with β much smaller than α (β=0.01 and α=0.99); Figure 4.15b shows the result when β is greater than α (β=0.99 and α=0.01); and Figure 4.15c shows the result when β and α are equal

	Accuracy			RMSE		
SNR_{dB}	Line	Vesselness	Proposed	Line	Vesselness	Proposed
-56	0.9867	0.9863	0.9894	0.1154	0.1169	0.1028
-58	0.9875	0.9844	0.9885	0.1117	0.1249	0.1071
-60	0.9800	0.9823	0.9893	0.1415	0.1330	0.1032
-62	0.9854	0.9823	0.9894	0.1207	0.1329	0.1029
-64	0.9407	0.9802	0.9891	0.2435	0.1406	0.1044
-66	0.9375	0.9830	0.9898	0.2500	0.1302	0.1010
-68	0.9300	0.9631	0.9894	0.2646	0.1920	0.1028
-70	0.9193	0.9450	0.9869	0.2841	0.2346	0.1161
-72	0.9120	0.9245	0.9829	0.2966	0.2748	0.1306
-74	0.8971	0.8972	0.9619	0.3207	0.3206	0.1952
-76	—	—	0.9579	—	—	0.2052
-78	—	—	0.9573	—	—	0.2066
-80	—	—	0.9446	—	—	0.2353

Table 4.1: Branch model: accuracy and root-mean-square error values for the three tested methods.



(a) (b) (c)

Figure 4.15: Top-down view of the spiral model, showing possible pattern detection depending on different size of α and β value. (a) $\beta = 0.01$ and $\alpha = 0.99$. (b) $\beta = 0.99$ and $\alpha = 0.01$ (c) $\beta = 0.5$, $\alpha = 0.5$.

(β=0.5, α=0.5).

ROC curve analysis was applied to demonstrate the sensitivity of different segmentation methods to image noise levels, and choose suitable values for the control parameters, α, β, and γ, and hysteresis thresholds. Here, each of the methods were tested with values of α and β ranging from 0.1 to 0.9, γ between

	Accuracy			RMSE		
SNR_{dB}	Line	Vesselness	Proposed	Line	Vesselness	Proposed
-56	0.9815	0.9860	0.9821	0.1360	0.1185	0.1338
-58	0.9802	0.9736	0.9817	0.1409	0.1625	0.1354
-60	0.9805	0.9732	0.9811	0.1395	0.1636	0.1374
-62	0.9656	0.9716	0.9824	0.1854	0.1685	0.1327
-64	0.9314	0.9671	0.9809	0.2620	0.1814	0.1382
-66	0.9232	0.9536	0.9815	0.2772	0.2153	0.1360
-68	0.9255	0.9444	0.9828	0.2730	0.2359	0.1311
-70	0.9199	0.9143	0.9789	0.2830	0.2927	0.1454
-72	0.9087	0.8965	0.9750	0.3022	0.3218	0.1582
-74	0.9092	0.8803	0.9723	0.3014	0.3459	0.1665
-76	—	—	0.9655	—	—	0.1858
-78	—	—	0.9556	—	—	0.2107
-80	—	—	0.9529	—	—	0.2171

Table 4.2: Spiral model: accuracy and root-mean-square error values for the three tested methods.

	Accuracy			RMSE		
SNR_{dB}	Line	Vesselness	Proposed	Line	Vesselness	Proposed
-56	0.9901	0.9870	0.9902	0.0995	0.1141	0.0990
-58	0.9902	0.9842	0.9870	0.0990	0.1256	0.1138
-60	0.9870	0.9834	0.9816	0.1138	0.1287	0.1356
-62	0.9850	0.9829	0.9806	0.1224	0.1306	0.1392
-64	0.9764	0.9542	0.9817	0.1537	0.2140	0.1351
-66	0.9671	0.9417	0.9819	0.1813	0.2415	0.1345
-68	0.9464	0.9131	0.9788	0.2314	0.2947	0.1456
-70	0.9271	0.9261	0.9799	0.2700	0.2719	0.1419
-72	0.8970	0.9118	0.9704	0.3210	0.2969	0.1720
-74	0.8937	0.8815	0.9499	0.3261	0.3443	0.2238
-76	—	—	0.9485	—	—	0.2269
-78	—	—	0.9317	—	—	0.2613
-80	—	—	0.9248	—	—	0.2743

Table 4.3: Column model: accuracy and root-mean-square error values for the three tested methods.

100 and 500, and hysteresis thresholds between 0 and 1, and the ROC curves are created (using nonlinear least squares fitting) for each of the methods and models with SNR of -66dB and -74dB, as shown in Figure 4.16. An example segmentation based on the selected parameter values is shown in Figure 4.11. Values representing the area under the curves (AUC ≤ 1) are provided. In each, the area under the curve is highest for the proposed method.

To illustrate the effect of control parameters α and β on the ROC curve, the following six combinations of α and β values were selected and numbered, and their numbers are indicated in the ROC plots in Figure 4.16, whilst the values for γ and hysteresis thresholds were fixed.

#	1	2	3	4	5	6
α	0.1	0.9	0.5	0.25	0.1	0.5
β	0.9	0.1	0.5	0.5	0.5	0.9

From the ROC plots, it can be seen that for the numbers 2 and 5 α and β combinations, there is notably low true positive segmentation rate across all models.

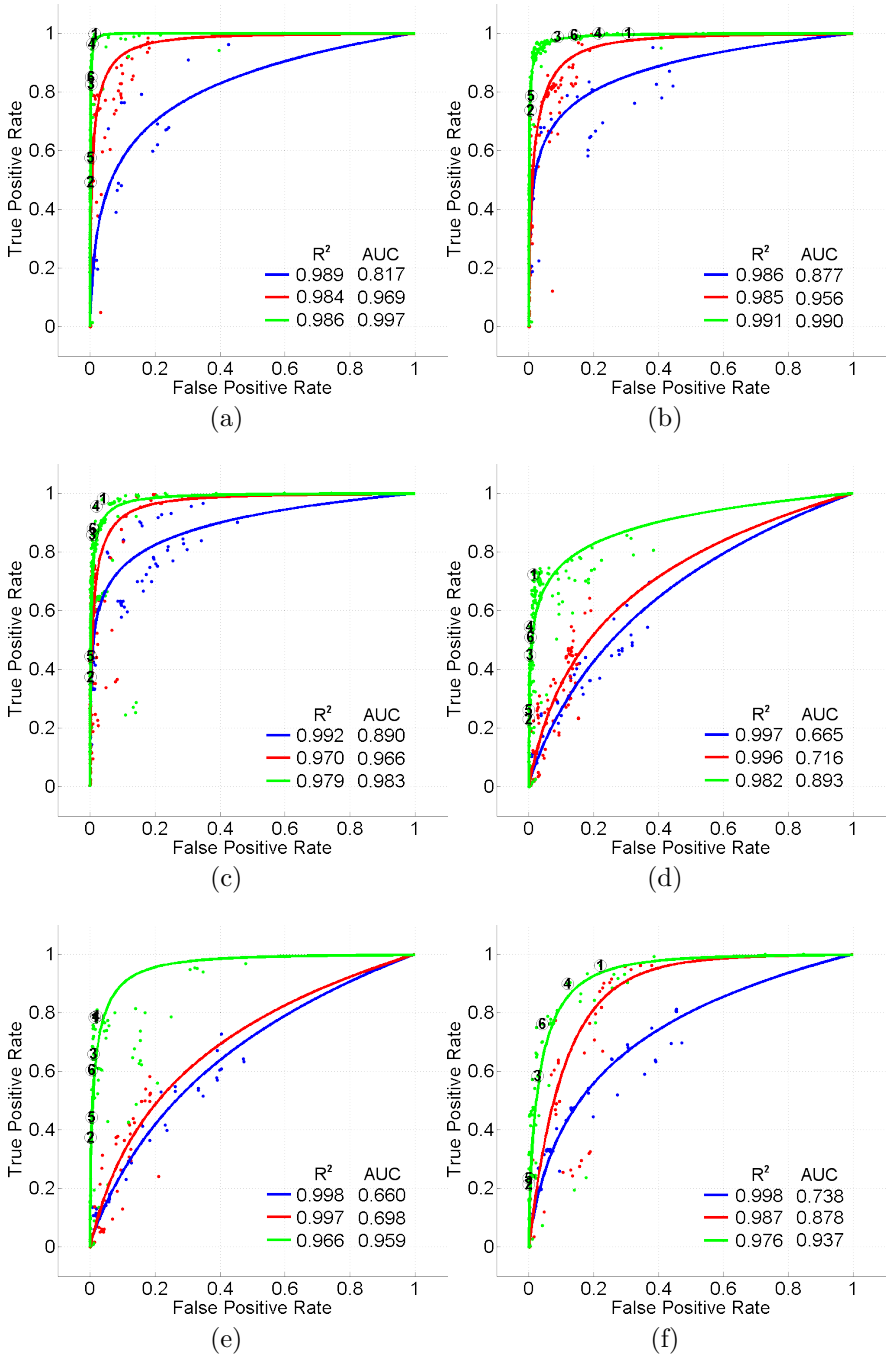


Figure 4.16: ROC curve comparison of the three methods on each synthetic model with two different levels of added noise: SNR -66dB and -74dB. Green points correspond to tests for the proposed method, red for the vesselness filter, and blue for the line filter. Non-linear least squares fitted curves are added, with R^2 values given in legend along with calculated area under the curve.

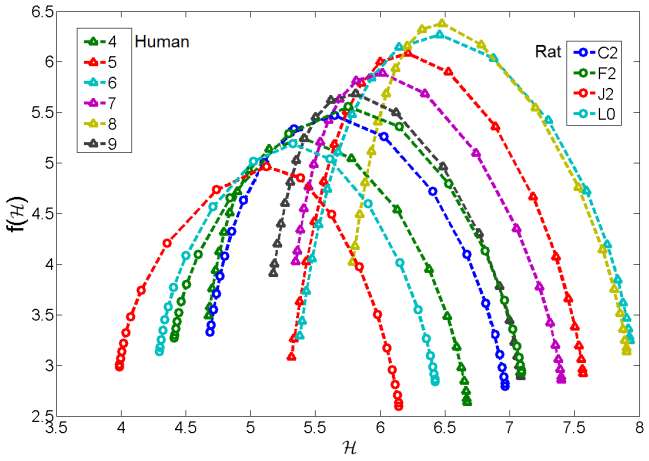
The numbers 1 and 4 combinations perform well for the branch (Figure 4.16a and Figure 4.16b), spiral (Figure 4.16d), and column (Figure 4.16e) models, as shown by their high true positive rates. However, for the spiral (Figure 4.16c) and column (Figure 4.16f) models, these combinations led to over-segmentation, as seen by the increased false positive rate.

4.4 Fractal Feature Extraction

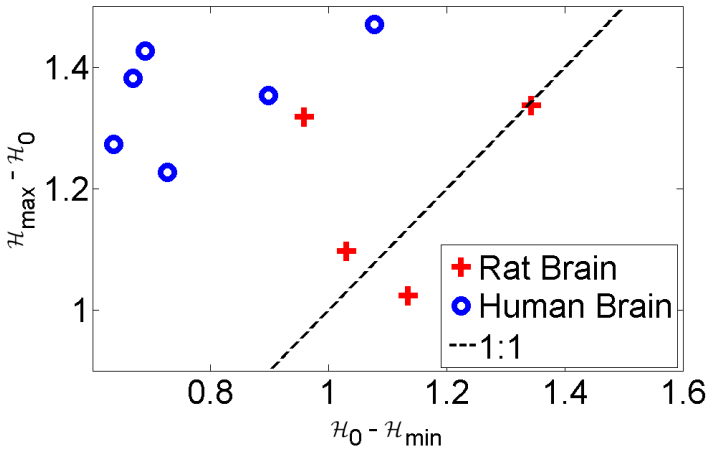
The analysis was based on the methods described in Section 3.3 implemented for 3D datasets. The spectra in Figure 4.10 of the rat brain microvasculature models show similar shape and position, with the exception of image C2, which is shifted slightly. The symmetry plot in Figure 4.17b essentially shows how skewed the spectrum is by comparing the distance of each spectrum tail from the centre. It shows that the spectra are nearly symmetrical, deviating slightly from the 1:1 ratio line [136]. This is likely to be due to a relatively low density of vessels in the rat brain vasculature models.

The human brain spectra show similar homogeneity in scaling to that of the rat microvasculature in the plot, with most of the spectra positioned beneath the 1:1 ratio line. The most distinct properties can be seen in the higher shifted spectra, as well as an increased level of asymmetry shown by the human head spectra.

Based on the vascular analysis results, it appears that the multifractal spectra show similar multifractal properties across different types of brains. Another observation from the analysis is that the symmetry plot shows a clear separation of points corresponding to visually different fractal spectra. This means that the scaling exponent together with the fractal dimension can provide a new vascular signature for classification of vasculature with different density and morphology. This then relates to diseases that alter these properties of the vasculature, and therefore offers a potential diagnostic tool for vascular pathology. Though the analysis was only performed on the small 3D datasets available, the conclusions are in line with previous research that used fractal analysis to classify 2D vasculature [32].



(a)



(b)

Figure 4.17: Multifractal analysis of six human brain vasculature models and four rat brain microvasculature models. (a) multifractal $\mathcal{H}/f(\mathcal{H})$ spectra, (b) symmetry features of each spectrum. The dashed line represents the 1:1 ratio plot.

4.5 Summary

This chapter presented experimental results on 3D vascular data using the proposed segmentation method and feature extraction method. The segmentation method not only prevents vessel discontinuities, but is also able to identify small and faint vessels against a complex ground. Experimental results have also shown that the proposed segmentation method produces good vessel segmentation on synthetic vessel images, with significant ability to deal with high noise levels.

Chapter 5

Case Study 2: 2D Retinal Data

Retinal blood vessels have been implicated in a large number of diseases including diabetic retinopathy and cardiovascular diseases, which cause damages to retinal blood vessels. The availability of retinal vessel imaging provides an excellent opportunity for monitoring and diagnosis of retinal diseases, and automatic analysis of retinal vessels will help with the processes. This chapter focuses on the analysis of 2D retinal images using the proposed methods. Four publicly available datasets are used for the experiments. The flowchart of this chapter can be viewed in Figure 5.1.

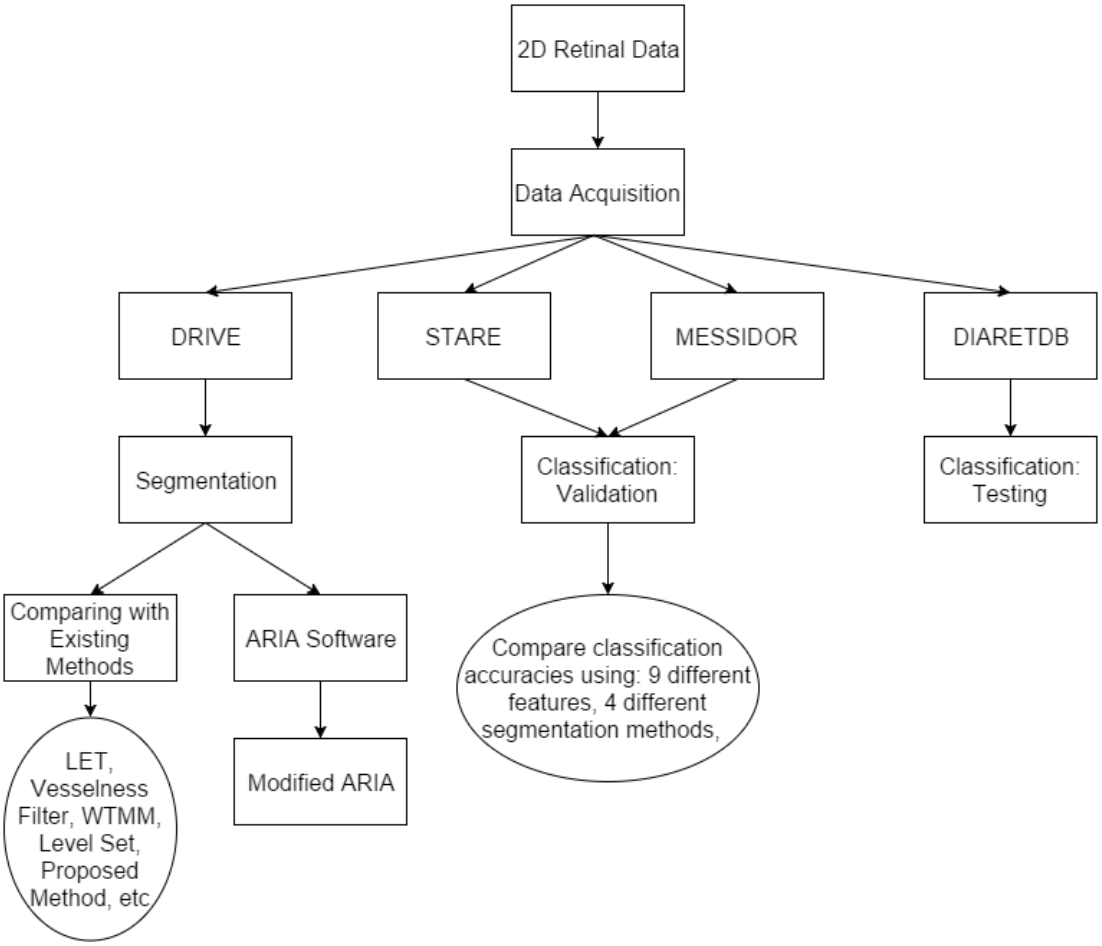


Figure 5.1: Flowchart of case study 2.

5.1 Data Acquisition

5.1.1 DRIVE

Retinal vessel images from a publicly available database, DRIVE (Digital Retinal Images for Vessel Extraction), is selected because the database is commonly used to enable comparative studies on segmentation of blood vessels in retinal images. The DRIVE retinal image database was created by [137], a diabetic retinopathy screening programme in the Netherlands. The database is publicly available and contains 40 retinal images of size 565×584, seven of which show signs of mild early Diabetic Retinopathy. For each image in the database, two manual segmentations of blood vessels are available. The second set of manually segmented images will be used in this investigation, because it is the most commonly used when comparing the effectiveness of methods.

5.1.2 STARE

The STARE (Structured Analysis of the Retina) retinal image database was created by the University of California for automatic diagnosis of eye diseases [138]. The database contains 400 retinal images of size 700×605, with information about the diseases that the images display. In this chapter, three sets of images from STARE are selected. The first dataset contains 10 healthy and 10 pathological (retinal vein occlusion, arteriosclerotic retinopathy, choroidal neovascularisation, background diabetic retinopathy, geographic atrophy RPE, retinitis, vasculitis, emboli, Hollenhorst plaque) retinal vascular images which were manually segmented by two observers (referred to by their initials VK and AH) and were segmented automatically. The images segmented by observer VK show higher levels of detail.

The second dataset contains 20 healthy and 20 pathological (background diabetic retinopathy) retinal vascular images. The third dataset contains 20 healthy, 20 pathological (background diabetic retinopathy) retinal vascular images, and another 20 pathological (retinal vein occlusion, arteriosclerotic retinopathy, and choroidal neovascularisation) retinal vascular images.

5.1.3 MESSIDOR

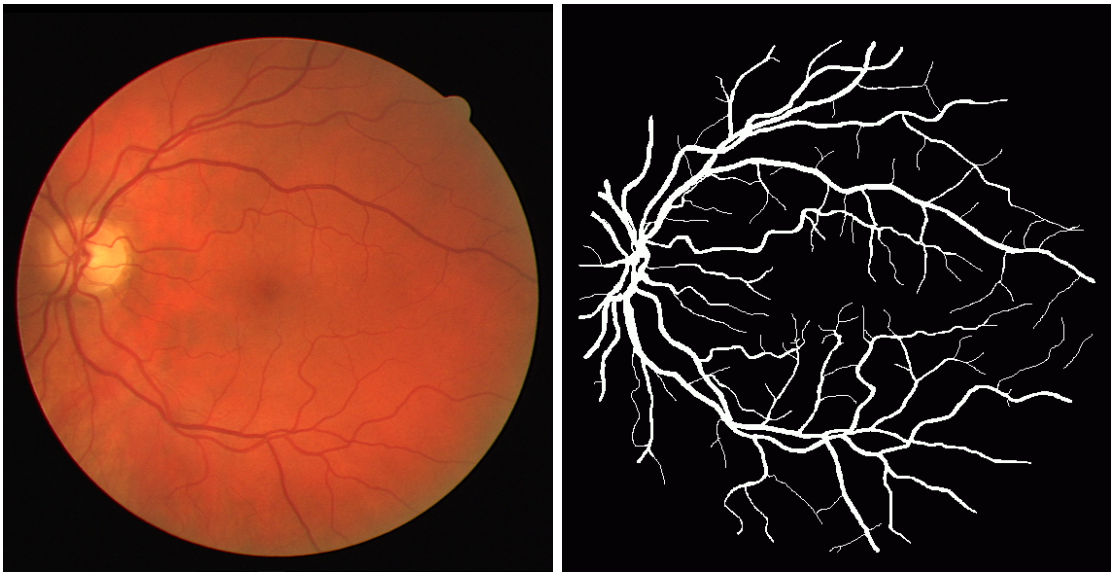
The MESSIDOR database was created by the Messidor research programme (http://messidor.crihan.fr) to evaluate lesion segmentation algorithms for colour retinal images. The database contains 1200 retinal images acquired at three different ophthalmological departments and the sizes of the images are 1440×960, 2240×1488, or 2304×1536. Each image is given a grade for retinopathy level $(0-3)$, and a risk for muscular edema $(0-2)$. The grade is determined based on the shortest distance between macula and hard exudates (<= one papilla diameter). In this chapter, 38 pathological retinal images from the first department with the highest grade for retinopathy level (3) and the risk of muscular edema (2) are selected. Also, 38 healthy retinal images are selected from those with the lowest grade for retinopathy level (0) and the risk of muscular edema (0).

5.1.4 DIARETDB

In 2006, a diabetic retinopathy image database with ground truth, called DIARETDB, was made publicly available for benchmarking diabetic retinopathy detection from digital images. The images were captured with a 50° FOV and a resolution of 1500×1152 at the Kuopio university hospital and were selected by the medical experts [139].

5.2 Segmentation with Retinal Vascular Data

In this section, 2D retinal vessel images from DRIVE are used to compare segmentation between existing methods. Figure 5.2 shows an example original retinal fundus image and its ground truth.



(a) (b)

Figure 5.2: 2D retinal fundus image from DRIVE. (a) original image (b) manual segmentation by an expert.

5.2.1 Experimental Segmentation Results

A review of retinal blood vessel segmentation using images from the DRIVE database has shown that most of the vessel image segmentation algorithms could only achieve 70% - 80% of segmentation sensitivity (blood-vessel pixels correctly classified) [93]. This is due to the difficulty of visualising small vessels in images. So it is desirable to enhance the vessels in images before segmentation, using, for example, a matched filter [140] or Gabor filter [141]. The following section briefly

evaluates the performances of some vessel segmentation methods those have been introduced in Section 2.1.

5.2.1.1 Local Entropy Thresholding

Figure 5.3 shows the vessel segmentation using local entropy thresholding. The drawback of this method is that it is not scale invariant and is not reliable using images with noise and without inhomogeneity, so a proper vessel enhancing algorithm is required.

The Gabor filter [142] is a Gaussian kernel function modulated by a sinusoidal plane wave in 2D and can be used for vessel enhancement [143, 144], edge detection [145], or line detection [146].

The Gabor filter can be represented by:

$$g_{\{\lambda,\theta,\varphi,\sigma,\gamma\}}(x, y) = \exp\left(-\frac{x'^2 + \gamma^2 y'^2}{2\sigma^2}\right)\cos\left(2\pi\frac{x'}{\lambda} + \varphi\right) \tag{5.1}$$

where

$$x' = x\cos\theta + y\sin\theta \tag{5.2}$$

$$y' = -x\sin\theta + y\cos\theta \tag{5.3}$$

where λ is the wavelength of the cosine factor, θ specifies the filter direction, ϕ is a constant representing the phase offset, γ represents the spatial aspect ratio, with σ as the standard deviation of the filter's Gaussian factor.

The Gabor filter has been commonly used for enhancing retinal vessels on fundus images because of its capability of detecting oriented features, and it is capable of tuning a signal to specific frequencies, allowing noise filtering and

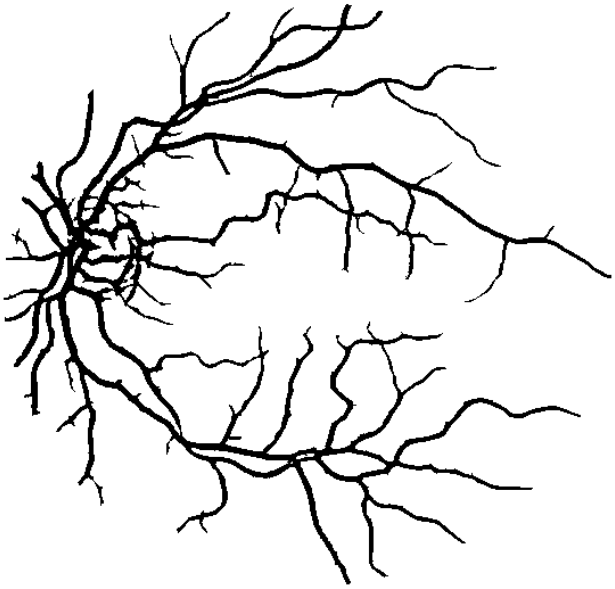


Figure 5.3: Result of LET without Gabor filter in 2D.

vessel enhancement at the same time [141, 147], when compared to several other available analysing wavelets, such as, the 2D Mexican hat and the optical wavelet [141].

Previous research has shown that LET can be used together with the Gabor filter for segmenting retinal blood vessels [148]. Figure 5.4 clearly shows that LET with the Gabor filter performed very well compared to LET (Figure 5.3). More of the narrow vessels are detected, although a few non-vessel pixels are incorrectly classified.

The problem with the use of the Gabor filter for vessel enhancement is that it produces false detection in retinal images with pathologies that present strong contrast. Also it is not able to detect thin vessels in the images [93].

Associated with the use of Gabor filters is the issue of selecting the right parameters that can produce the best result for an application [143, 149]. For example, parameters were suggested by [150] and [151] which gave the maximum

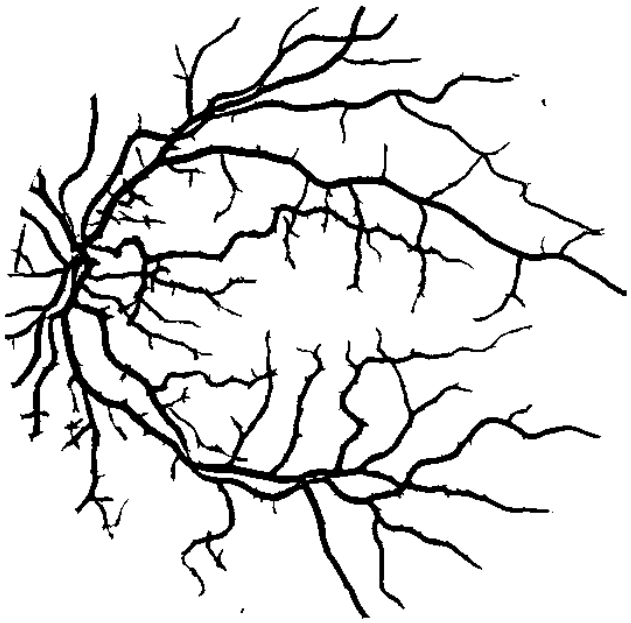


Figure 5.4: Result of LET with Gabor Filter in 2D.

response of an image. However, these parameters have not produced satisfactory results on vessel images. An experiment was therefore conducted for selecting Gabor filter parameters for a specific vessel segmentation method using a genetic algorithm, by taking into account ground truth vessel images.

The genetic algorithm is a method for solving optimisation problems that mimic the natural selection [152]. The algorithm continually modifies a population of individual solutions and reproduces a new generation of offsprings, which inherit features from the previous generation. This evolution process eventually leads to an optimal solution [153]. While there exist many good publicly available genetic algorithm packages, the MATLAB Genetic Algorithm Toolbox was selected because it provides an environment compatible with other tools [154].

The experiment proceeds as follows:

1. The vessel image is enhanced with a matched filter followed by a Gabor filter,

with parameter values selected by a genetic algorithm from real intervals, for example, $Wavelength = [1, 5]; Aspect\ ratio = [0.1, 5];\ Bandwidth = [1, 6];\ Rotation\ Angle\ in\ radians = [0, 4]$ and $Rotation\ Number = [1, 32]$;

2. The enhanced image is segmented with the local entropy thresholding method.

3. The segmentation result is compared with the manually segmented ground truth images [137]. Sensitivity and specificity are calculated for evaluation of selected parameters.

4. The process iterates until the solutions no longer improve. We then select the parameters leading to the highest sum of sensitivity and specificity.

Figure 5.5 shows the sensitivity and specificity of segmentation with selected parameters by the genetic algorithm. The method retains computational simplicity and straightforwardness, and at the same time achieves accurate segmentation results for retinal images. Using a genetic algorithm can help to find good parameters for the filter but it is also time-consuming. Technically, the selected value can only be used for the specific image of current interest. An automated and computationally efficient algorithm is therefore needed.

5.2.1.2 Multiscale Vesselness Filter

The advantages of the vesselness filter are that it is fast, simple, and accurate, as shown in Figures 5.6.

Result shows that segmentation using the vesselness alone on 2D retinal image is not good enough, the method is still sensitive to noise, however, as already introduced in the Section 3.1 that, by combining the vesselness filter with the line

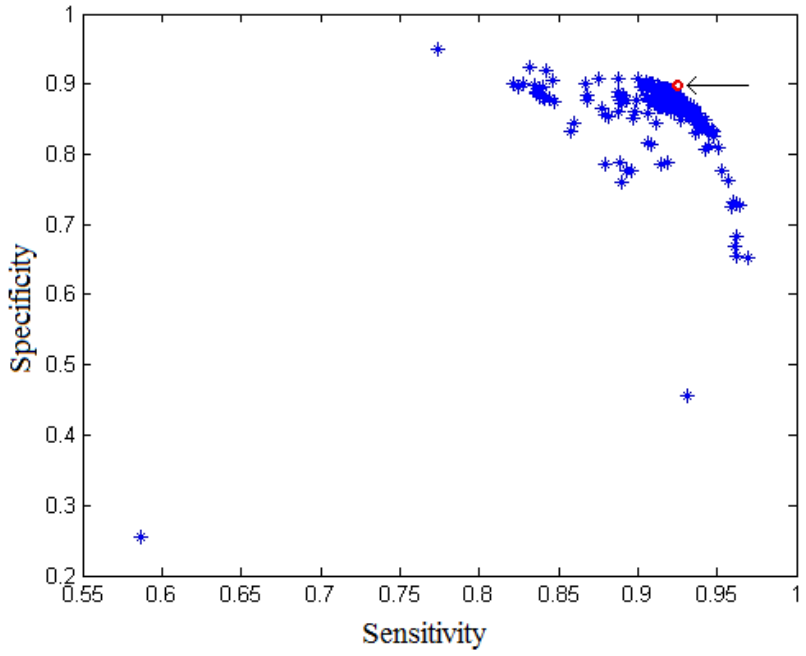


Figure 5.5: Sensitivity/specificity values generated. The red dot represents the results produced using the Gabor filter with the most optimal parameters.

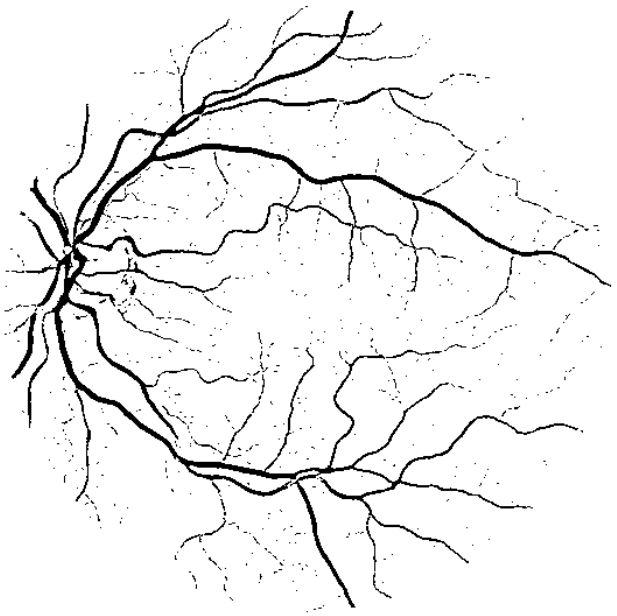


Figure 5.6: Result of the vesselness filter in 2D.

filter can significantly increase the segmentation accuracy. Figure 5.7 shows an example segmentation result using the proposed combinatory vessel filter. It can be seen that the vascular is clearer and more microvessels were detected.

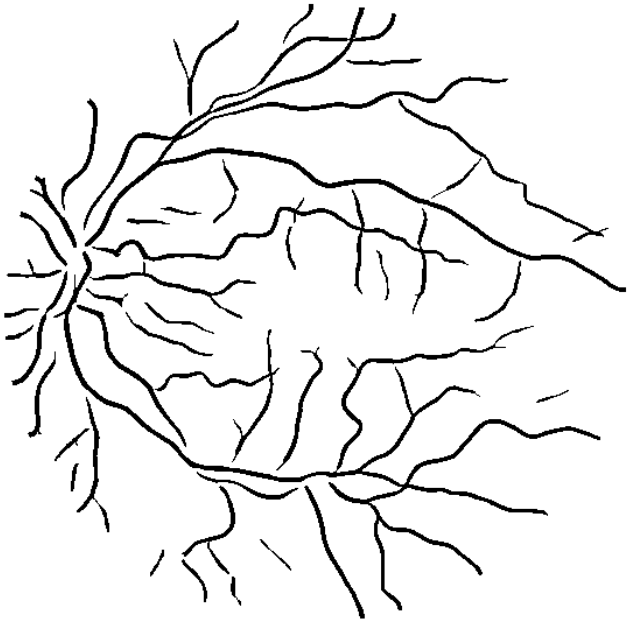


Figure 5.7: Result of the combinatory vessel filter in 2D.

Because vessels always appear in varying widths, the original vesselness filter integrates the filter response at different scales to form a final estimate. The critical drawback of the vesselness filter is that it is not scale invariant: user interaction is required for selecting the range of scales. Failure to select the correct scale values will result in double (or multiple) vessels for a single vessel, as shown in Figure 5.8a. The problem can be solved by including a discrete wavelet transform for its multiscale property, as shown in Figure 5.8b.

Discrete wavelet transform can look at a signal at different resolutions and scales, allowing the use of a single transform to analyse multiscale data and remove the requirement for repeated applications [120, 155]. The vesselness filter produced



(a) (b)

Figure 5.8: Samples of vessel extraction with one scale (a) with and (b) without applying discrete wavelet transform.

higher sensitivity when implemented together with the discrete wavelet transform. However, the computational cost of vessel segmentation with discrete wavelet transform in higher dimension is much higher. An image with large vessel width differences requires a higher level of decomposition, a higher level of decomposition requires longer implementation (8 wavelet coefficients at level one and 15 wavelet coefficients at level two). Also, different databases may require different wavelets to obtain the best result so that the design of wavelets is also very important; indeed it is crucial.

5.2.1.3 Wavelet Transform Modulus Maxima (WTMM)

Figure 5.9 shows that WTMM is very likely to be a Canny edge detector. The problem with this method is that the computational time increases exponentially with the size of the image. Also, when the scales were large, thin vessels were blurred due to the large Gaussian window convolution, which was unable to provide an analytical model due to the removal of crispness of the thin vessels.

Thus, these thin vessels appear to be a slightly broader, when compared to the results of thresholding schemes.

In general, the major advantage of the system was its simplicity of implementation. The drawback of this method is that edges found are not connected, and also it is susceptible to error for noisy images.

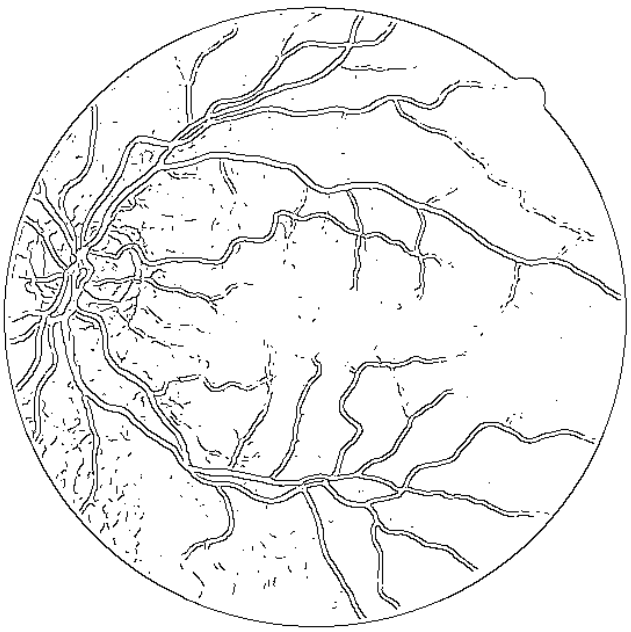


Figure 5.9: Result of WTMM in 2D.

5.2.1.4 Level Set Methods

Figure 5.10 shows the result of a simple gradient-based level set method using a 2D retinal vessel image. Because this method extracts the blood vessel as a whole, noise in the background where no blood vessels are present is removed. However, as stated earlier, the evolving contour simply leaks through the gaps and the object is represented by incomplete contours.

The local phase-based level set method can distinguish line and edge by taking

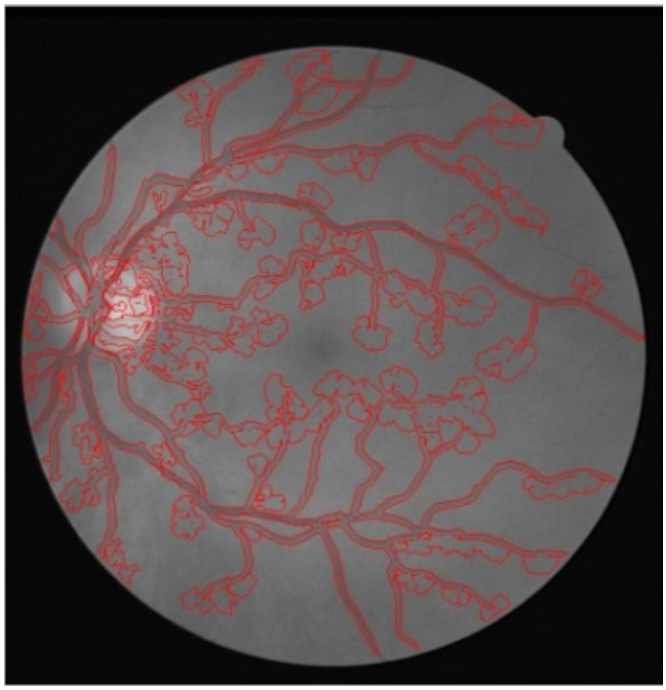


Figure 5.10: Leaking problem with level set.

local phase into account. Most importantly, it halts the evolving contour at the end of the vessel to prevent leakage. Although the method succeeds in other areas, such as, object and motion segmentation, it fails for images that contain faint and narrow vessel pixels, leading to the level set terminating early and leaving many vessels undetected, as shown in Figure 5.11.

As an experiment, we integrated this phase-based level set method with a preprocessing method, matched filter, to enhance the vessel image before segmentation. The main concept of the matched filter [156] is to convolve a signal with a designed kernel and extract information (from that signal) which matches the kernel. Based on the fact that blood vessels are typically line-like, with small curvature and usually have a relatively low contrast, a matched filter kernel was designed for blood vessel' network extraction [157, 140, 17, 138]:

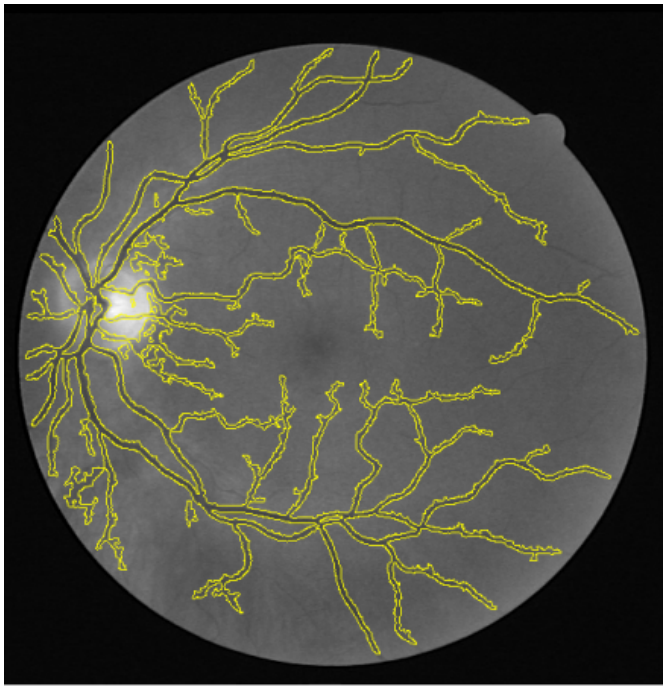


Figure 5.11: Result of phase-based level set.

$$f(x,y) = -exp\left(\frac{-x^2}{2\sigma^2}\right), for\ |y| \leq L/2, \tag{5.4}$$

Here, σ defines the spread of the intensity profile and L is the length of the segment. It is assumed that a fixed vessel has orientation along the y-axis. In reality, vessels are oriented in many different directions, so a set of kernels at equiangular rotations is applied at each pixel along 12 possible directions and only the maximum response is retained. The highest response of the filter is selected for each pixel and is thresholded to provide a binary vessel image followed by some post-processing to produce final vessel segmentation [157].

Figure 5.12 shows the level set segmentation result using level set on a matched filtered image: many faint vessels were detected, although level set failed to halt the evolving contour at the end of some vessels. Moreover, the kernel may not respond to vessels that have a different profile. Also, the image background

variation and presence of pathologies in the image increase the number of false detections [93], an example of which is shown in Figure 5.13. Additional processing techniques are therefore required to produce more accuracy segmentation.

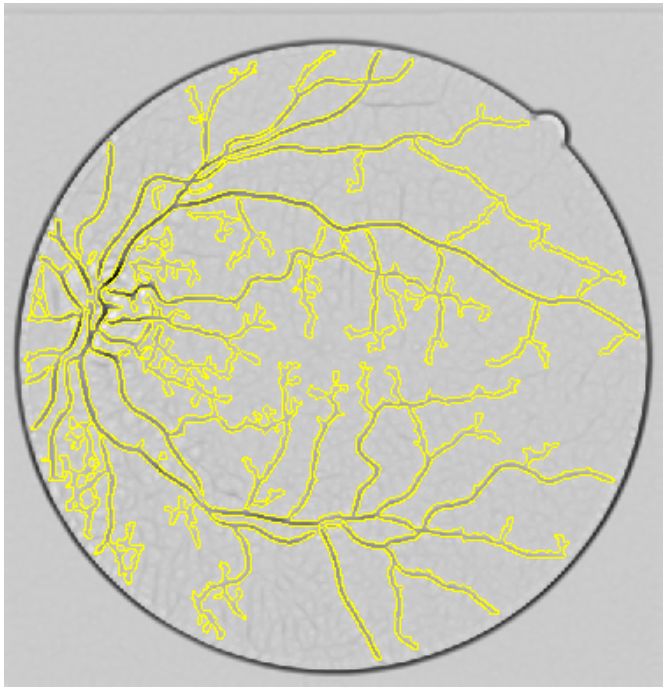
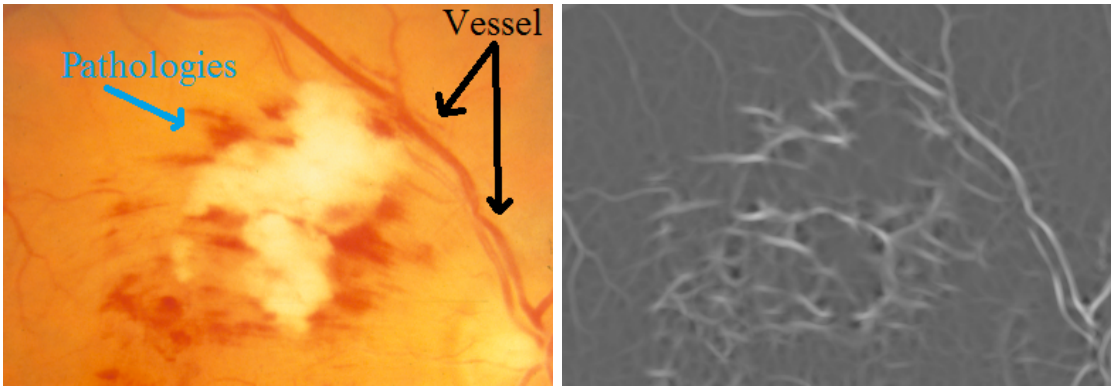


Figure 5.12: Result of phase-based level set on matched filtered image.

5.2.1.5 Summary of the Results

The aim of this section is to report on the experimental results of the vessel segmentation methods those described above. Full details on the implementation can be found in Chapter 8.

Tables 5.1 contain performance detail on 2D vessel data. Performance measures are sensitivity, the percentage of correctly classified blood-vessel pixels, obtained by TP/(TP+FN); specificity, the percentage of correctly classified non-blood-vessel pixels, obtained by TN/(FP+TN); accuracy, how close the number of correctly classified pixels is to the actual value, obtained by (TP+TN)/(TP+FP+FN+TN)



(a) (b)

Figure 5.13: (a) Original retinal image, where vessel and pathologies are labelled in black and blue respectively. (b) Image after being matched filtered.

and precision, how close the true positive and false positive are, obtained by TP/(TP+FP); where T=TURE, F=FALSE, P=POSITIVE and N=NEGATIVE.

In general, WTMM was the fastest. The speed of the vesselness filter and LET were acceptable, but LET with Gabor filter are slower due to parameter selection for the Gabor filter. LET with Gabor filter achieved the highest sensitivity (89.83%). Both this method and the level set method provided higher sensitivity as more vessels are detected. WTMM and LET produced low sensitivity due to unconnected and missing vessels. The vesselness filter produced low sensitivity (62.64%) as user-selected scales and threshold values were susceptible to error. The best specificity obtained is by the vesselness filter (98.74%), because it is robust to image noise. Also, improved LET, level set methods, and WTMM are sensitive to image noise. Although the proposed combinatory vesselness filter produced the highest accuracy (95.05%) while maintaining a good implementation speed, the improvement was not very significant. This is because the combinatory vessel filter was not designed particularly for segmenting retinal blood vessel.

The availability of retinal vessel DRIVE dataset has provided an excellent

Methods	Sensitivity	Specificity	Accuracy	Run time	Drawback
WTMM	0.4545	0.9518	0.8916	0.27s	Unconnected vessels
LET	0.7599	0.9621	0.9383	2.15s	Missing vessels
LET+Gabor filter	0.8983	0.9435	0.9378	16.15s	Parameter selection
Phase-based level set	0.8567	0.9399	0.9299	40.53s	Early termination
PB level set+matched filter	0.8712	0.861	0.8622	25.46s	Non-smooth vessels
Vesselness filter	0.6264	0.9874	0.9425	1.05s	Needs user interaction
Combinatory filter	0.6747	0.9831	0.9569	2.08s	No significant improvement

Table 5.1: Performance detail using 2D retinal vessel image, based on literature review in this thesis.

Methods	Sensitivity	Specificity	Accuracy
Supervised Based [158]	0.7067	0.9801	0.9452
Matched Filtering Based [159]	0.7120	0.9724	0.9382
Morphological Processing Based [160]	0.7352	0.9795	0.9458
Multiscale Based [161]	0.7470	0.9550	0.9290
Model Based [162]	0.7436	0.9615	0.9352
Combinatory filter	0.6258	0.9820	0.9505

Table 5.2: Performance detail using 2D retinal vessel image, based on previous literature review [93].

opportunity for researchers to design and implement blood vessel algorithm, the performance of these algorithms were then summarised and evaluated in detail in literature [93]. The methods were divided into two main categories, supervised and unsupervised methods. The unsupervised methods were then divided into several groups base on the basic method used. We have reviewed these methods and then selected the best one from each of these groups to represent the whole group, the segmentation results are shown in Tables 5.2. In summary, the proposed segmentation method produced the highest specificity and accuracy but the sensitivity is relatively lower than the other methods. Although many algorithms have produced promising results, it is believed that there is still room for improvement in blood vessel segmentation methodologies, for example, by applying segmentation method on high resolution images to achieve high accuracy. For the time being, the resolution of the images is good enough for certain analyses like fractal dimension or tortuosity, which will be discussed in Section 5.3.

5.2.2 Improving An Existing Retinal Analysis Software

Traditional methods for vascular analysis on 2D retinal vasculature often include measuring the number of vessel branching points or length of individual vessels, and these can now be easily achieved through MATLAB morphological operations:'bwmorph'. Example results of this on a retinal image are shown in Figure 5.14.

- Figure 5.14b shows a segmented retinal vasculature using the method presented in Section 3.1.
- To find branch points of the vessels, the image must be skeletonised. The basic concept of this algorithm is to remove the boundaries of an object without breaking it apart. Figure 5.14c shows the centreline of the segmented retinal vasculature using MATLAB commend "bwmorph(im, 'skel')".
- The basic algorithm of branch point detection is to look at the 3×3 neighbourhood pixels; a point is a branch point if at least three of its neighbouring pixels are '1 '. Figure 5.14d shows branching points of the segmented retinal vasculature using the MATLAB command "bwmorph(im, 'branchpoints')", branch points are highlighted in red.
- Figure 5.14e shows the isolated vessels after removing the branch points and short vessels.
- Figure 5.14f shows the length of two isolated vessel; this was done by counting the number of pixels that are connected.

For practical use, a robust image analysis tool is desirable. ARIA is open-source software written in MATLAB for the analysis of blood vessels in retinal

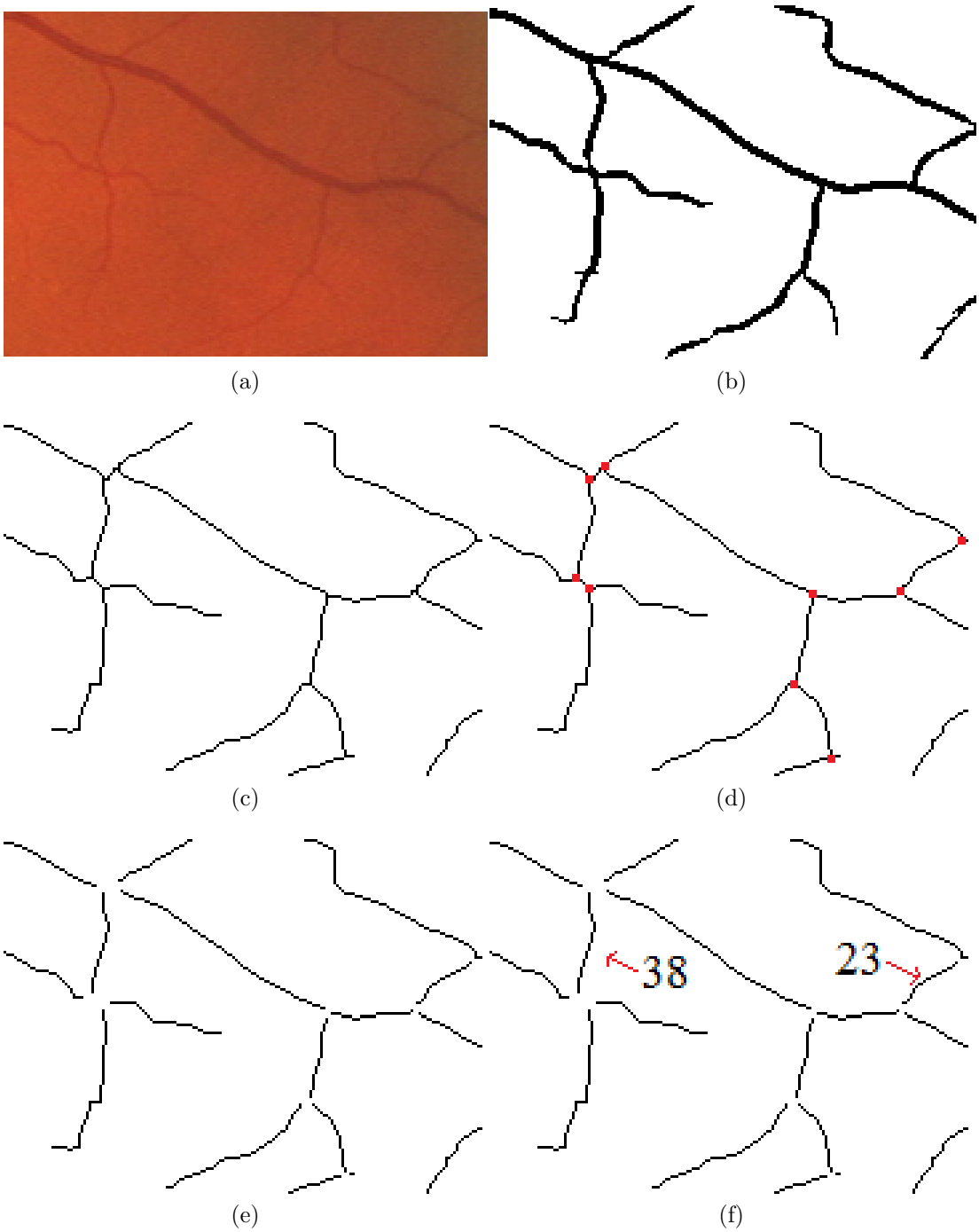


Figure 5.14: (a) Original retinal fundus image, (b) segmented retinal vasculature, (c) centreline of segmented retinal vasculature, (d) highlighted vessel branching point, (d) vasculature skeleton after removing branch points and small vessels, (e) length of a selected vessel branch.

images. There are many ophthalmologists have been using ARIA to accurately quantify eye structure and function in order to understand diseases that affect the eyes and the brain. However, the main algorithm of the software is very basic, and thus needs some improvements. We have been collaborating with the University of Leicester to improve the ARIA. The following section briefly introduces the improved ARIA software, and some comparison with the original version are given.

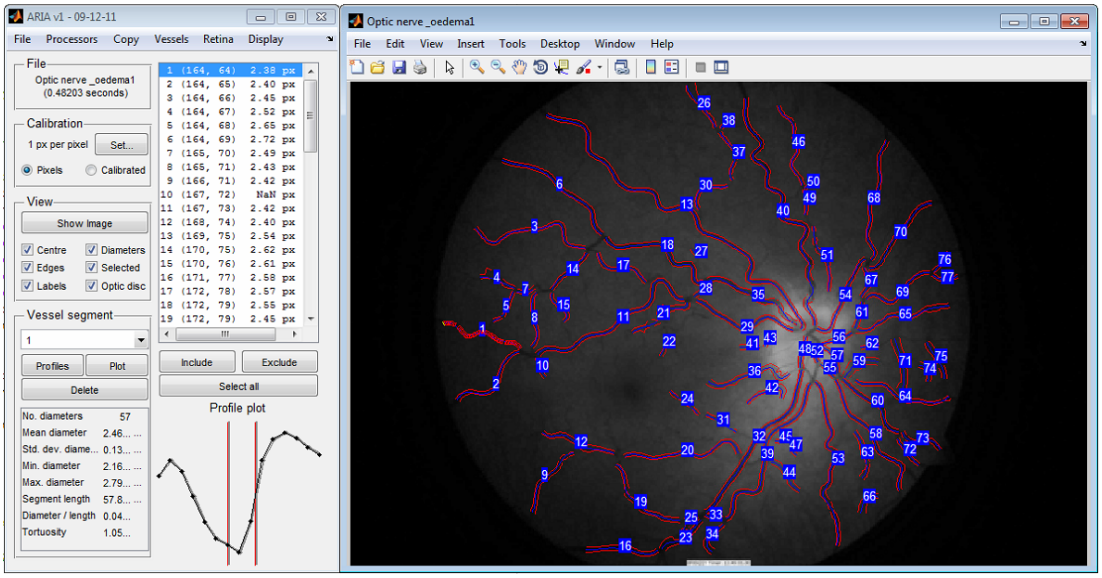
5.2.2.1 Original ARIA

ARIA (automated retinal image analyser) is free, open-source, MATLAB based software developed at Queen 's University, Belfast, for the automated detection and measurement of retinal vessel diameters [163]. The software is fast and easy to modify while achieving average segmentation accuracy. Although it was designed to analyse human fundus photographs, it has also successfully been applied to rodent fluorescein angiograms in a physiology study.

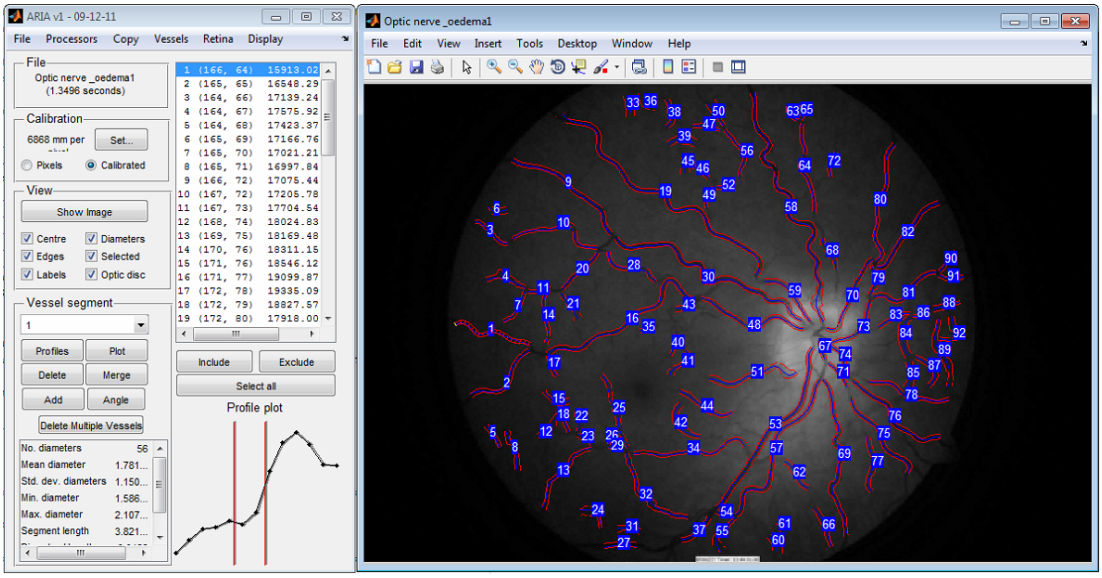
However, the software suffers from a few drawbacks which make it inefficient:

- The software segments an image using the isotropic undecimated wavelet transform to enhance vessels, and uses a single threshold value to produce a vasculature image, so it is not very accurate due to the inhomogeneity of fundus images. An example segmentation result using the original ARIA is shown in Figure 5.15a. It can be seen that many small but clearly visible vessels are not detected.

- The collaborators from the University of Leicester therefore added a new function to manually add a new vessel, as shown in the 'Add' button in Figure 5.15b. The function solved the missing vessels issue but was extremely time-consuming, so new functions were required to improve the working



(a)



(b)

Figure 5.15: (a) Original ARIA interface, (b) improved ARIA interface.

efficiency.

- Other function such as deleting vessels is also time-consuming; the user is required to input the label of the vessel to delete it.

- Because ARIA was designed to measure vessel diameter, it lacks other basic

functions that ophthalmologists normally need, such as measuring vessel branch angles.

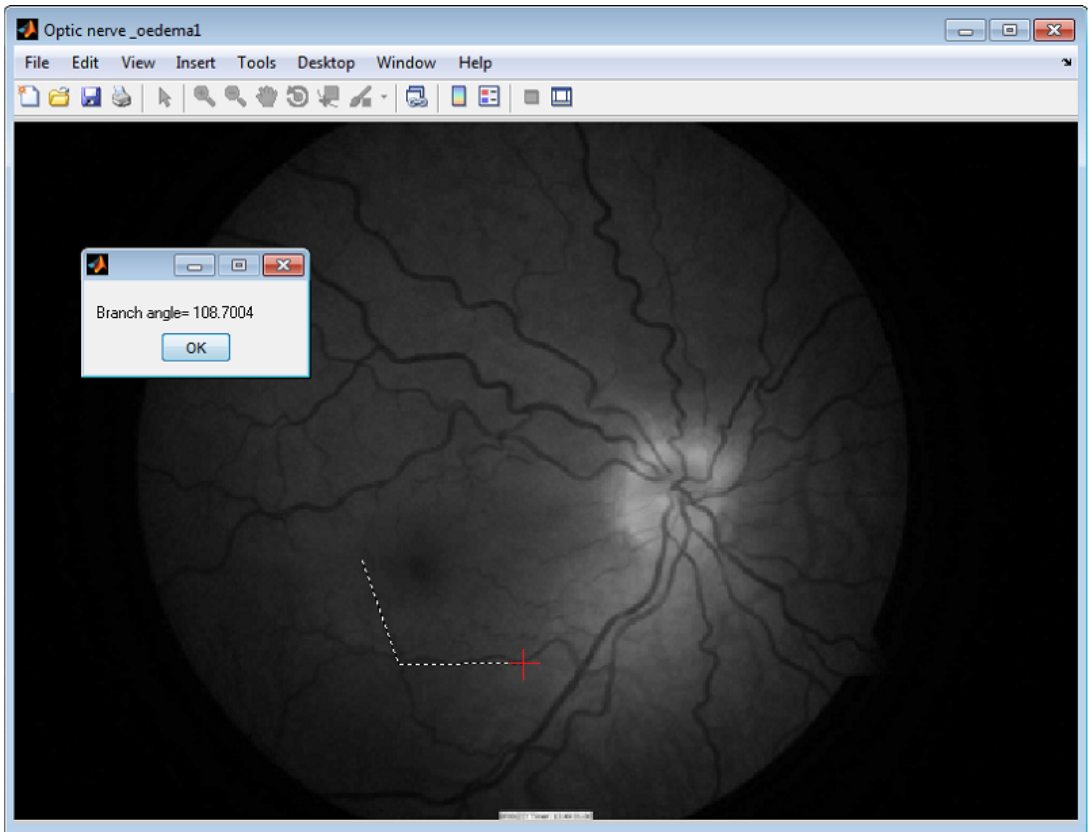
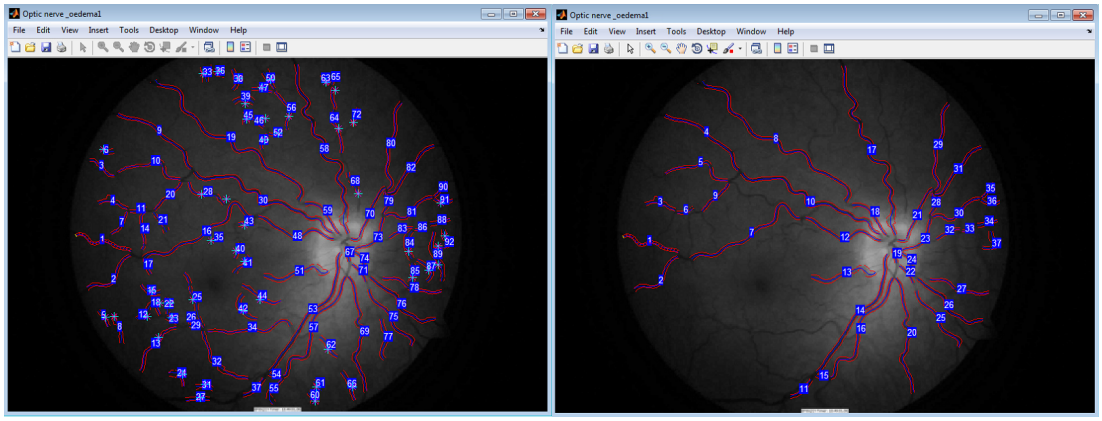


Figure 5.16: Measuring vessel branch angle.

5.2.2.2 The Improved ARIA Software

We have developed improved ARIA software with the following new features: The new ARIA not only produces more accurate segmentation, but it also helps the ophthalmologist in analysing retinal vessels more efficiently.

- The improved ARIA segments the retinal vasculature, using the method presented in Section 3.1, and more missing vessels are detected so a lot of



(a) (b)

Figure 5.17: (a) Select vessel to delete, (b) vessels after deleting.

time is saved compared with manually adding new vessels. An example segmentation result using the improved ARIA is shown in Figure 5.15b.

- A new function was added to manually measure vessel branch angle, the function requires the user to draw two lines along the vessel branch of interest, and the branch angle is shown in a pop-up window. An example of this is shown in Figure 5.16.

- A new function to delete multiple vessels was added. The user can click on the vessels to be deleted instead of keying in the label of the vessel. The biggest advantage of this function is that instead of deleting the vessels one by one, this function supports the deleting of multiple vessels at the same time. An example of this function is shown in Figure 5.17. One of the potential uses of this function is that user can delete all the artery vessels and investigate just the vein vessels.

5.3 Classification with Retinal Vascular Data

It has been suggested in recent years that vascular anomaly, especially the microvascular anomaly, could potentially serve as an early imaging biomarker of many diseases [164, 14]. For example, retinal arteriolar narrowing is associated with risk of diabetes, whereas retinal venular widening is associated with the development of diabetic retinopathy [165]. However, the current practice of diabetic retinopathy screening is based on manual examination of fundus images by human experts [166], which are not suitable for the microvasculature.

There has been published research using fractal analysis to calculate fractal dimensions of retinal blood vessels [167, 32]. Research has shown that, compared with the normal retina, the density of vessel in the diabetic retinopathy retina is different due to the growth of tiny, twisted, and easy to break blood vessels [167, 168]. However, so far there has been no systematic research extracting discriminant fractal features from retinal vessels for classifications.

This section reports experiments for feature extraction from multifractal spectra of retinal vessels and classification of these features to distinguish healthy and pathological retinal vessels. The methods are tested on three public available retinal databases. Results show that high classification accuracy can be achieved by combining features extracted from multifractal spectra and those extracted from Fourier power spectra of retinal images.

5.3.1 Validation

5.3.1.1 Retinal Databases

In this section, two major publicly available retinal databases, STARE and MESSIDOR are used for the experiments. The quality of some of the retinal images is bad, the vasculature is hardly visible to the human eye and is therefore discarded. Vessel extraction is often the first stage of processing before pathology detection algorithms are applied. Therefore, the vessels are segmented using three different methods to demonstrate how classification accuracy can be affected by the quality of vessel segmentation algorithms. The three segmentation methods are the line filter [126, 6], the Hessian–based vessel filter [19, 5], and the combinatory vessel filter [169], which were introduced in Section 3.1. The combinatory vessel filter performs better than the other two filters because it is robust to broken and faint vessels [169]. Descriptions of these databases are presented as follows, and example segmentation images are shown in Figures 5.18 and 5.19.

5.3.1.2 Feature Extraction

Multifractal analysis is performed on the segmented vasculature to obtain multifractal spectra and features are extracted from the spectra.

Figure 5.20 shows multifractal spectra of the same retinal vessel image rotated in eight directions. It is clear the fractal spectra for all the images are the same.

Figure 5.21 shows the multifractal spectra and Fourier power spectra of retinal vasculature automatically segmented using different methods from the STARE datasets. Both multifractal spectra and Fourier power spectra of diabetic retinopathy vasculature are higher than those of healthy vasculature due to the fact that the pathology is indicated by the density and tortuosity of the vasculature.

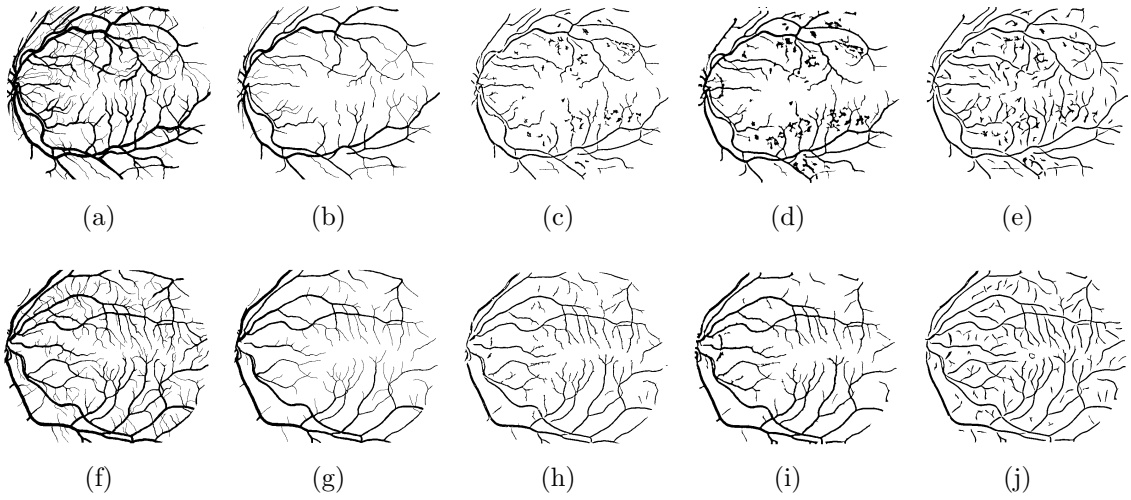
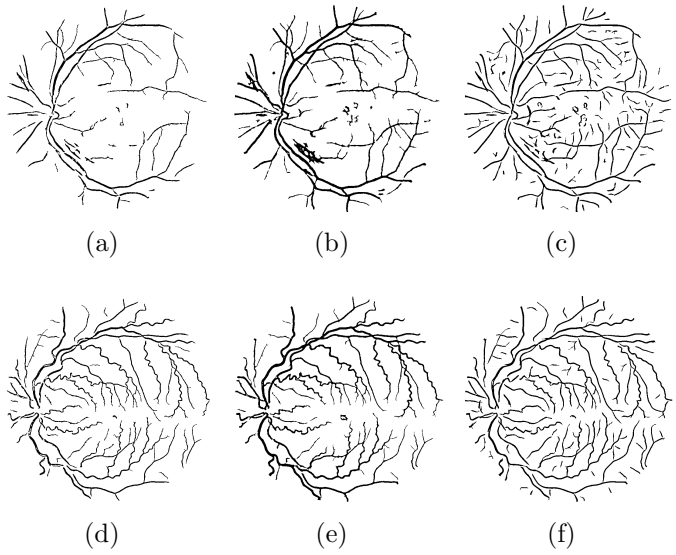


Figure 5.18: Example vessel segmentation on images from STARE. (a)-(e) are retinal vascular images of a diabetic patient manually segmented by VK and AH, and automatically segmented using the Hessian–based vessel filter, the line filter, and the combinatory vessel filter respectively. (f)-(i) are retinal vascular images of a healthy patient manually segmented by VK and AH, and automatically segmented by the Hessian–based vessel filter, the line filter, and the combinatory vessel filter respectively.

The spectra of the retinal vasculature segmented using the combinatory vessel filter discriminate the classes better because the segmentation accuracy of the combinatory vessel filter is higher than the line filter and the Hessian–based vessel filter [169].

Figure 5.22 shows the multifractal spectra and Fourier fractal spectra of retinal vasculature automatically segmented using different methods from MESSIDOR dataset. The results are similar to those shown in Figure 5.21: because muscular edema is the cause of diabetic retinopathy [170], both multifractal spectra and Fourier fractal spectra of pathological vasculature are higher than those of healthy vasculature.

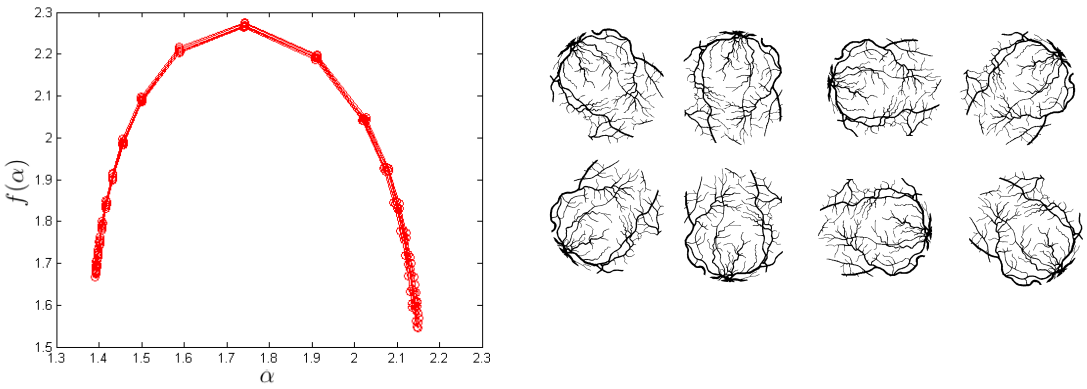
Figure 5.23 shows that the multifractal spectra and the Fourier fractal spectra of both manually and automatically segmented retinal vasculature from the



(a) (b) (c)

(d) (e) (f)

Figure 5.19: Example vessel segmentation on images from MESSIDOR. (a)-(c) are retinal vascular images of a patient (macular edema) segmented by the Hessian–based vessel filter, the line filter, and the combinatory vessel filter respectively, (d)-(f) are retinal vascular images of a healthy patient segmented by the Hessian–based vessel filter, the line filter, and the combinatory vessel filter respectively.



(a) (b)

Figure 5.20: Multifractal analysis of a retinal vascular image from STARE manually segmented by VK: (a) multifractal $\alpha/f(\alpha)$ spectra, (b) the vascular image rotated in eight directions.

STARE dataset have similar shape, with those of the pathological vasculature being slightly lower than the healthy vasculature. The difference of the spectra of automatically segmented retinal vasculature is less distinct due to the fact that

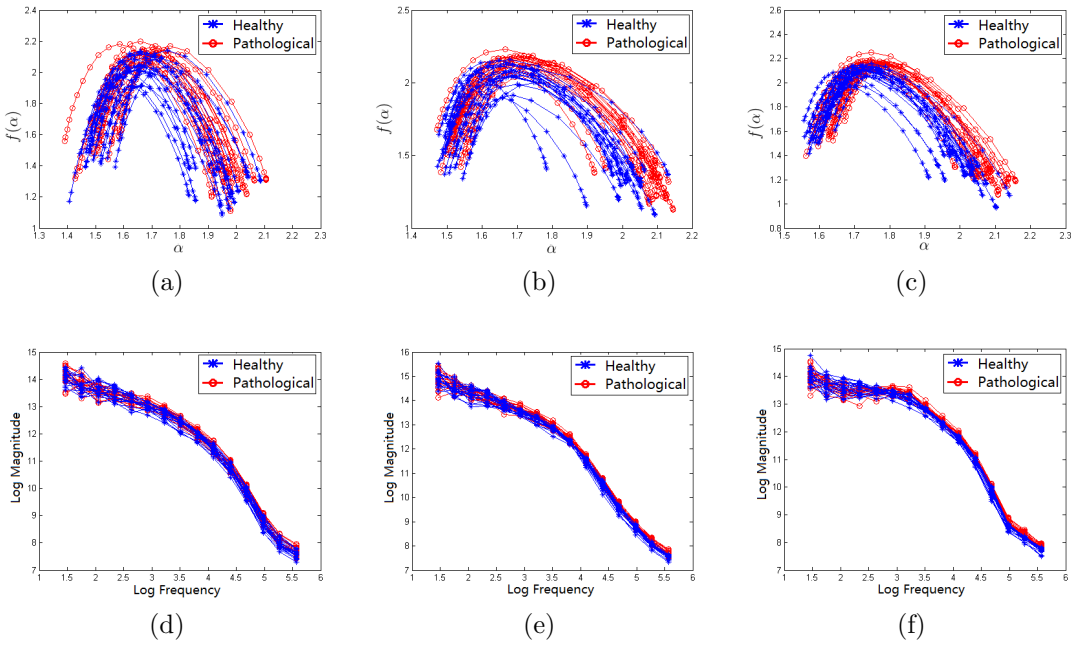


Figure 5.21: Multifractal analysis of 20 healthy and 20 pathological (background diabetic retinopathy) retinal vasculatures from STARE: (a)-(c) $\alpha/f(\alpha)$ spectra of vasculatures automatically segmented by the Hessian–based vessel filter, the line filter, and the combinatory vessel filter respectively; (d)-(f) Fourier power spectra of vasculature automatically segmented by the Hessian–based vessel filter, the line filter, and the combinatory vessel filter respectively.

the results are affected by the segmentation.

Figure 5.24 shows the multifractal features of a healthy dataset and two pathological datasets. The first pathological dataset contains images of patients with diabetic retinopathy and the second contains images of patients with various eye diseases such as retinal vein occlusion, arteriosclerotic retinopathy, and choroidal neovascularisation. It appears that the feature values of the vasculature in the second pathological dataset are slightly lower than those of the first pathological dataset, and are shifted to the right of those of healthy vasculature. The multifractal spectra of the classes are somehow overlapped but the plots of their features $\alpha_0 - \alpha_{\min}/f_0$ plots appear to separate the classes.

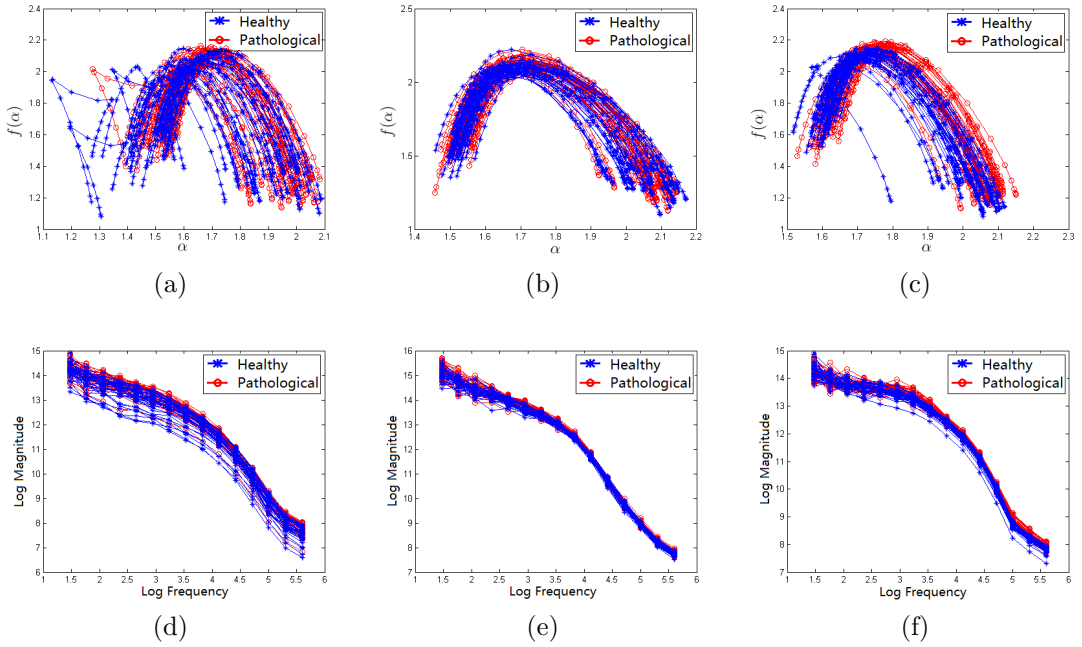
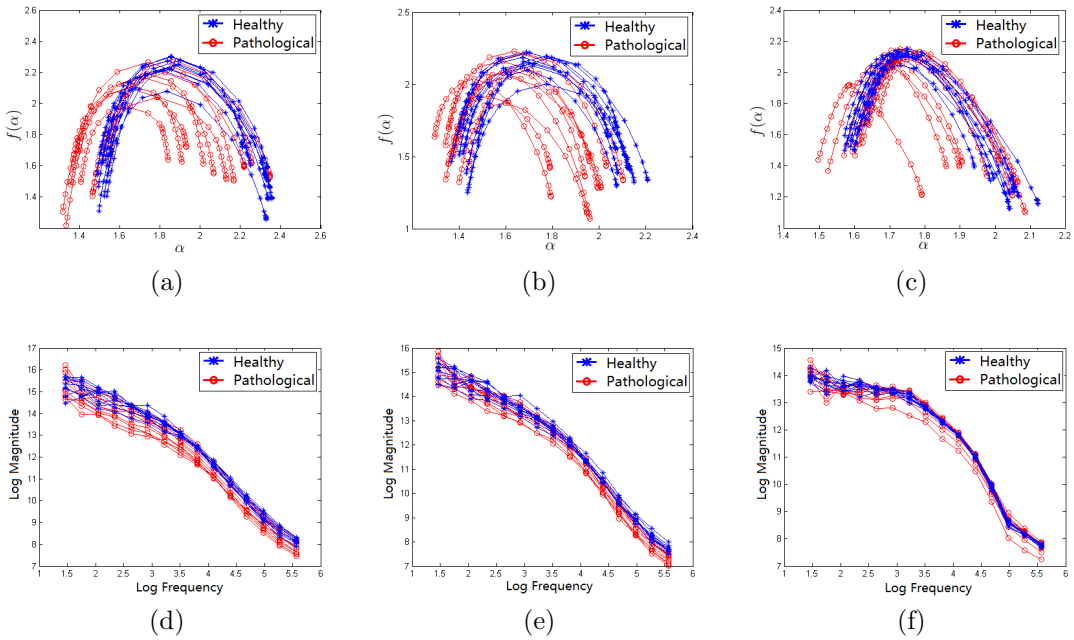


Figure 5.22: Multifractal analysis of 38 healthy and 38 pathological (muscular edema) retinal vasculature from MESSIDOR: (a)-(c) $\alpha/f(\alpha)$ spectra of vasculature automatically segmented by the Hessian–based vessel filter, the line filter, and the combinatory vessel filter respectively; (d)-(f) Fourier power spectra of vasculatures automatically segmented by Hessian–based vessel filter, the line filter, and the combinatory vessel filter respectively.

Due to massive overlapping occurring in the multifractal spectra and Fourier fractal spectra, box plots are used to show the differences of the extracted features between retinal vasculature of healthy people and patients with retinal diseases, with a focus on diabetic retinopathy. The plots presented use vasculatures automatically segmented using the combinatory vessel filter.

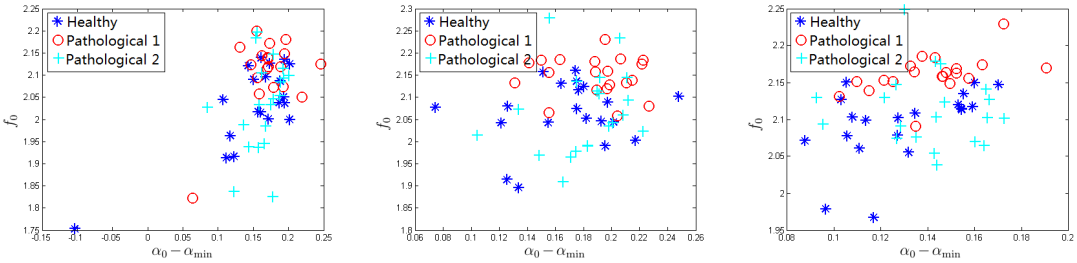
Figure 5.25 shows the fractal features of a healthy dataset and two pathological datasets from the STARE datasets. The first pathological dataset (P1) contains images of patients with diabetic retinopathy, and the second (P2) contains images of patients with various eye diseases such as retinal vein occlusion, arteriosclerotic retinopathy, and choroidal neovascularisation. It can be seen from Figure s5.25a,



(a) (b) (c)

(d) (e) (f)

Figure 5.23: Multifractal analysis of 10 healthy and 10 pathological retinal vasculature from STARE: (a)-(c) $\alpha/f(\alpha)$ spectra of vasculature manually segmented by VK and AH, and automatically segmented by the combinatory vessel filter, respectively; (d)-(f) Fourier fractal spectra of vasculatures manually segmented by VK and AH, and automatically segmented by the combinatory vessel filter, respectively.



(a) (b) (c)

Figure 5.24: Multifractal analysis of 20 healthy, 20 pathological (background diabetic retinopathy) and 20 pathological (retinal vein occlusion, arteriosclerotic retinopathy, choroidal neovascularisation) retinal vasculatures from STARE: (a)-(c) $\alpha_0 - \alpha_{\min}/f_0$ plots of vasculatures automatically segmented by the Hessian–based vessel filter, the line filter, and the combinatory vessel filter respectively.

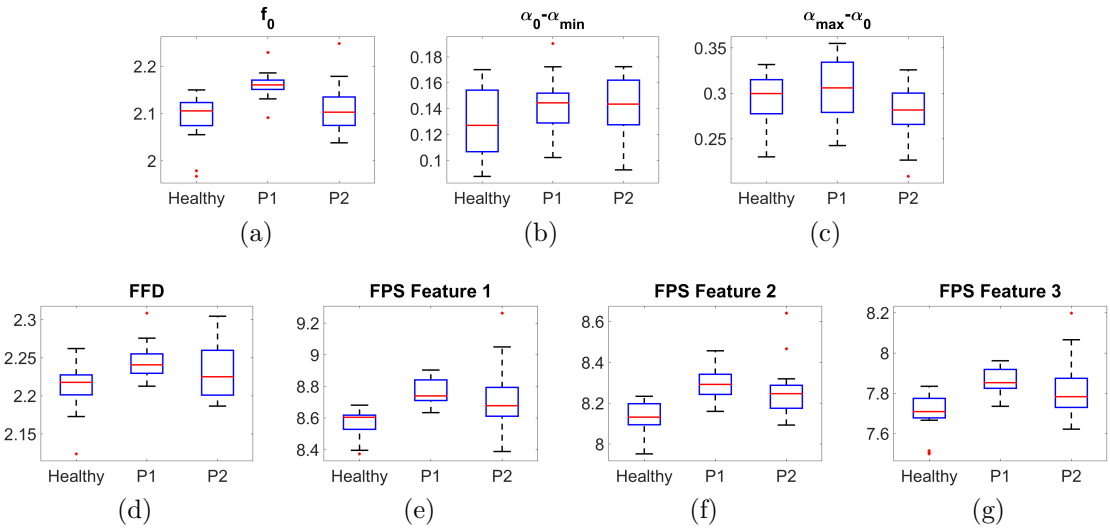


Figure 5.25: Features extracted from $\alpha/f(\alpha)$ spectra and Fourier power spectra of vasculatures automatically segmented by the combinatory vessel filter: (a) the peak of the multifractal spectrum (f_0); (b) the symmetry features $\alpha_0 - \alpha_{\min}$, and (c) $\alpha_{\max} - \alpha_0$, as well as the Fourier features (d) FFD and (e)-(g) FPS magnitude values at high frequencies. The dataset contains 20 healthy and 20 pathological (P1: background diabetic retinopathy) and another 20 pathological (P2: retinal vein occlusion, arteriosclerotic retinopathy, and choroidal neovascularisation) retinal vasculatures from STARE.

5.25b and 5.25c that the multifractal spectra of diabetic retinopathy vasculature are higher than those of healthy vasculature, and the width of the spectra of diabetic retinopathy vasculature is slightly wider. The Fourier fractal spectra of diabetic retinopathy vasculature are steeper than those of healthy vasculature, and the Fourier fractal spectra magnitude values of diabetic retinopathy vasculature at high frequencies are also higher. The values of features of the second pathological dataset have large variation and are in between the healthy dataset and the diabetic dataset. All these differences shown in the plots represent the fact that the pathology is indicated by the density and tortuosity of the vasculature, especially the change of microvasculature [171, 172, 173]. This means that the conclusions are in line with previous research that used fractal analysis to classify

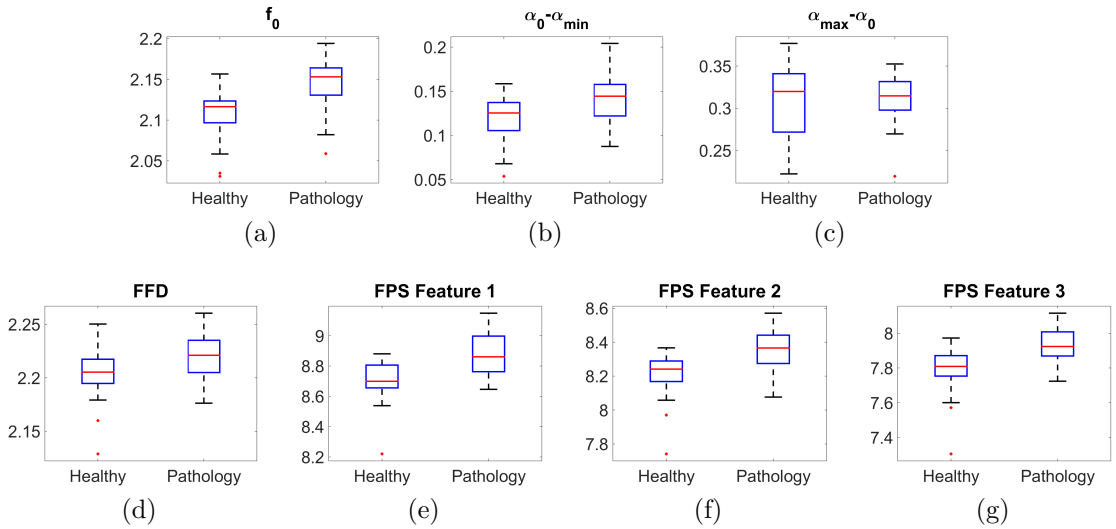


Figure 5.26: Features extracted from $\alpha/f(\alpha)$ spectra and Fourier power spectra of vasculatures automatically segmented by the combinatory vessel filter: (a) the peak of the multifractal spectrum (f_0), (b) the symmetry features $\alpha_0 - \alpha_{\min}$, and (c) $\alpha_{\max} - \alpha_0$, as well as the Fourier features (d) FFD and (e)- (g) FPS magnitude values at high frequencies. The dataset contains 38 healthy and 38 pathological (muscular edema) retinal vasculature from MESSIDOR.

2D vasculature [32].

Figure 5.26 shows the features of retinal vasculature from the MESSIDOR dataset. The results are similar to those shown in Figure 5.21 because muscular edema is the cause of diabetic retinopathy [170].

5.3.1.3 Classification

A nonlinear support vector machine (SVM) classifier described in Section 2.3.1 with Gaussian radial basis function (RBF) kernel [174] is chosen for classification of the extracted vascular features of healthy and pathological vasculature.

To evaluate the performance of the proposed feature extraction methods for classification, each dataset in the STARE and MESSIDOR databases is split into two parts: three-quarters of the dataset as a training set and the rest of the

dataset as test set, each containing an equal number of healthy and pathological retinal vascular images. Both automatic and manual segmentation of the images in the STARE database are used for comparison purposes. The classifier is trained using the training set and tested using the test set. The process is repeated 100 times, and results are averaged.

Three similarity measures (sensitivity, specificity, and accuracy) are defined to demonstrate the effectiveness of the proposed method and to compare it with existing methods. Sensitivity is the rate that healthy vasculature is correctly identified; specificity is the rate that pathological vasculature is correctly identified; and accuracy is the 'closeness' of the classification result to the ground-truth. Specifically, let P and N be the numbers of healthy vasculature and pathological vasculature, respectively. Let TP be the healthy vasculature identified correctly; and TN be the pathological vasculature identified correctly. Let FP be the pathological vasculature identified incorrectly as healthy; and FN be the healthy vasculature identified incorrectly as pathological. We then have:

$$\begin{aligned} \text{sensitivity} &= TP/P \\ \text{specificity} &= TN/N \\ \text{accuracy} &= (TP+TN)/(P+N) \end{aligned}$$

The classification results are shown in Table s5.3 and 5.4. Apart from those manually segmented by VK and AH, all vasculatures are automatically segmented.

Results show that SVM performed poorly on monofractal dimension features (f_0, FFD) of the vasculature from STARE. Classification accuracy with f_0 is slightly improved when the method takes into account the symmetry feature, although the accuracy is still poor (83% for two classes and 57.47% for three

Label	Feature Type	Detail	Accuracy for 2 classes	Accuracy for 3 classes
1	Fractal Feature	f_0	0.859	0.5413
2		Symmetry Feature	0.55	0.356
3		f_0 + Symmetry Feature	0.83	0.5747
4	Fourier Feature	FFD	0.722	0.4547
5		FPS Feature	0.899	0.6093
6		FFD + FPS Feature	**0.928**	0.628
7		f0+ FFD	0.849	0.5453
8		Symmetry Feature + FPS Feature	0.901	0.6487
9	Combinatory Feature	Combinatory Feature: (f_0 + FFD + Symmetry Feature + FPS Feature)	0.855	**0.6813**
Vessel Filter			0.602	0.4367
Line Filter			0.854	0.6373
Manual:Ah			0.79	n/a
Manual:VK			0.772	n/a
Auto: Combinatory			0.736	n/a

Table 5.3: Classification accuracy using different methods on the STARE dataset. The best result is highlighted in bold. Number 1-9 use vasculature segmented by the combinatory vessel filter. The last three rows use the manual and automatically segmented vasculature data.

Label	Feature Type	Detail	Accuracy for 2 Classes
1	Fractal Feature	f_0	0.726
2		Symmetry Feature	0.656
3		f_0 + Symmetry Feature	0.768
4	Fourier Feature	FFD	0.649
5		FPS Feature	0.793
6		FFD + FPS Feature	0.769
7		f_0, FPS Feature	0.7
8		Symmetry Feature + FPS Feature	**0.796**
9	Combinatory Feature	f_0 + FFD + Symmetry Feature + FPS Feature)	0.77
Vessel Filter			0.581
Line Filter			0.665

Table 5.4: Classification accuracy using different methods on the MESSIDOR dataset. The best result is highlighted in bold. Number 1-9 use vasculature segmented by the combinatory vessel filter.

classes). Classification accuracy with FFD has been significantly increased by including the FPS feature (92.8% for two classes and 62.8% for three classes).

Results also show that the classification on vasculature from STARE using the combinatory feature has produced slightly lower accuracy (85.5%), when compared with the combination of FPS feature and symmetry feature (90.1%), and the combination of FPS feature and FFD (92.8%) for two classes (healthy and background diabetic retinopathy). Nonetheless, the fact that classification using the combinatory feature produced the highest classification results (68.13%) for three classes (healthy, background diabetic retinopathy, vein occlusion etc) demonstrates the ability of the combinatory feature for handling complex data with large varieties.

Classification using the combinatory feature of automatically segmented vasculature from STARE by the combinatory vessel filter produced higher accuracy, compare with the Hessian–based vessel filter and the line filter (85.5%, 60.2%, and 85.4% for two classes respectively, 68.13%, 43.67%, and 63.73% for three classes respectively). However, classification using the combinatory feature of vasculature automatically segmented by the combinatory vessel filter performed poorly (77.2%) when compare with vasculature manually segmented by observer VK (79%) and observer AH (73.6%). The conclusion is that the accuracy of vessel segmentation algorithms can also affect the classification accuracy.

The same conclusions were drawn from the accuracy on vasculature from MESSIDOR for classifying healthy and muscular edema vasculature, with classification accuracy using the combinatory feature (77%) being slightly lower than using the combination of FPS feature and symmetry feature (79.6%); classification using the combinatory vessel filter produced higher accuracy than using the other two methods with lower segmentation accuracy.

A receiver operating characteristic (ROC) curve is plotted, showing sensitivity for each result against the value of 1−specificity to visualise the performance of all

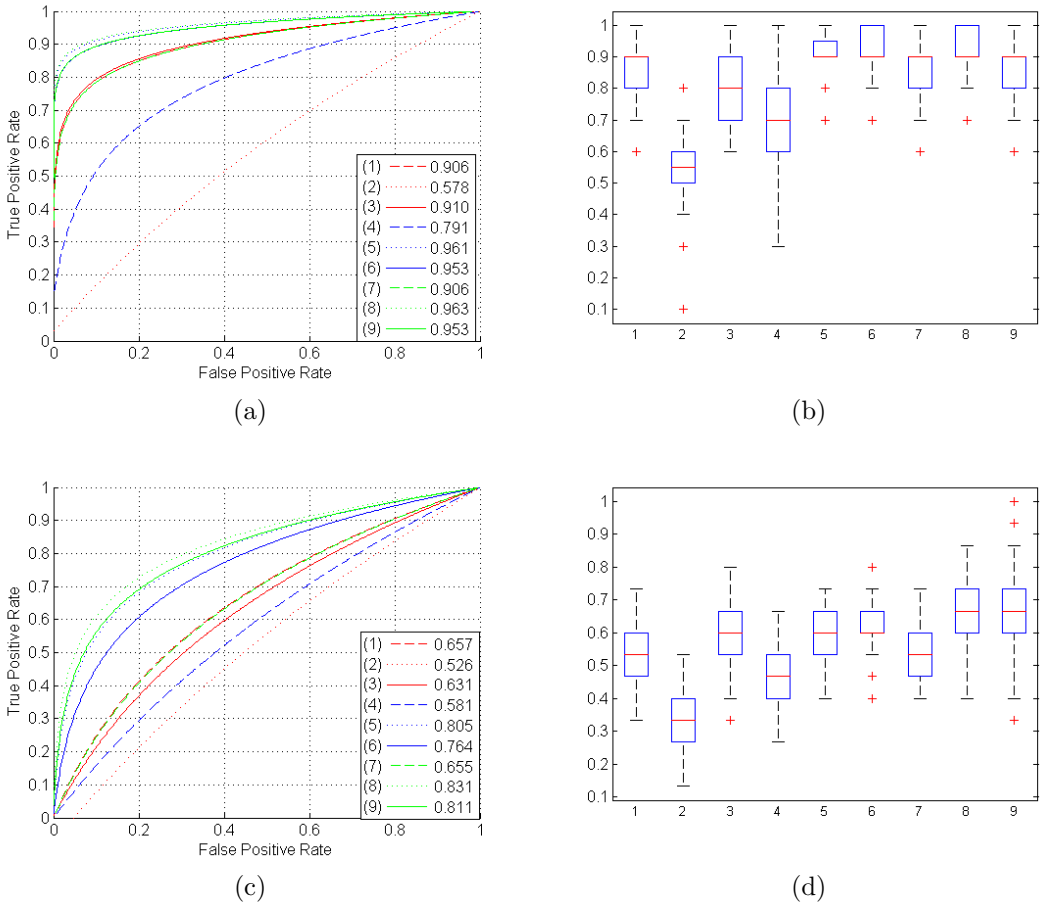


Figure 5.27: ROC analysis with area under the curve (AUC) and box plots on the STARE dataset: SVM results using different features for classifying (a)(b) two classes and (c)(d) three classes respectively. The labels refer to the feature combinations in Table 5.3.

the methods. The plot begins at $(0, 0)$ and as sensitivity increases, the specificity is expected to decrease, leading to a convex curve terminating at $(1, 1)$. The closer the curve passes to $(0, 1)$ the more it indicates success. A way to interpret and quantify this curve is to calculate the area under the curve (AUC), a value between 0 and 1.

Figures 5.27a, 5.27c and 5.28a show the curves (fit using non-linear least squares) for each of the methods using different features on the STARE and

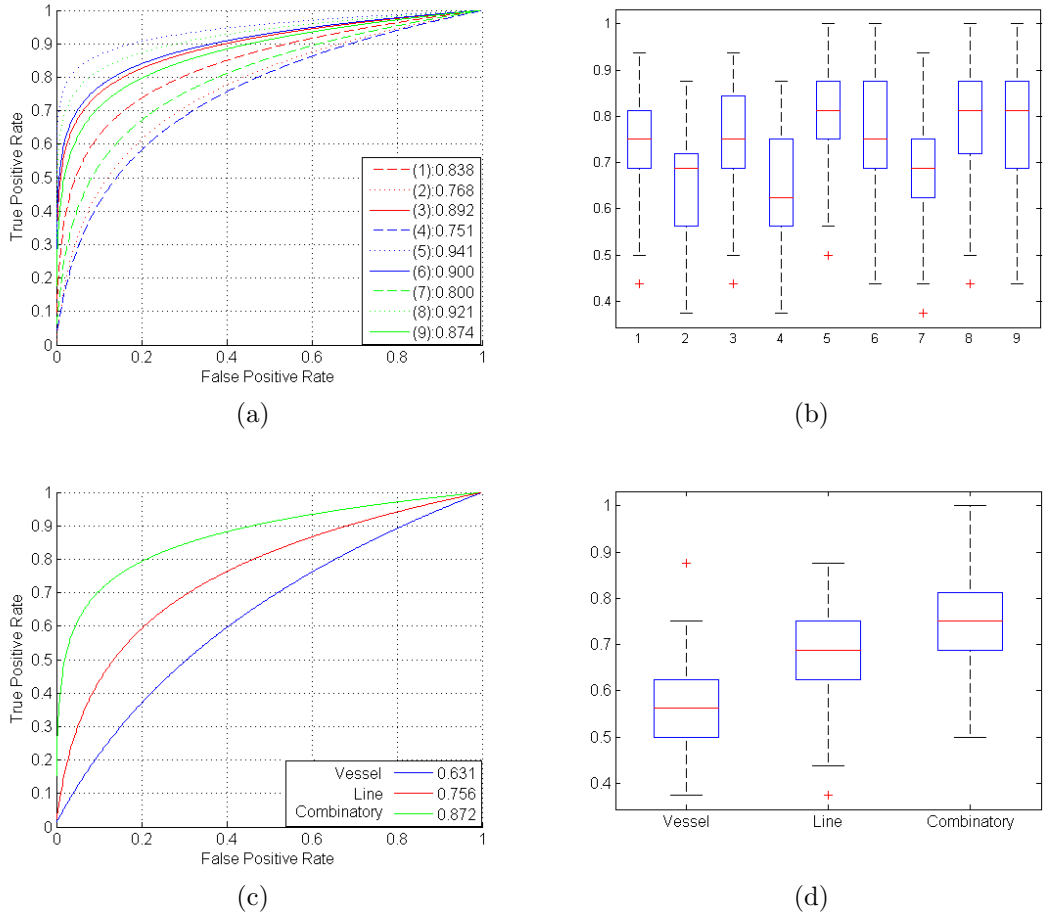


Figure 5.28: ROC analysis with area under the curve (AUC) and box plots on the MESSIDOR dataset: (a)(b) SVM results using different features for classifying two classes. Vasculature segmented by the combinatory vessel filter. (c)(d) SVM results using the combinatory features for classifying two classes. Vasculature segmented by the Hessian–based vessel filter, the line filter, and the combinatory vessel filter. The labels refer to the feature combinations in Table 5.4.

MESSIDOR datasets (two class and three class for STARE and two class for MESSIDOR). Values representing the area under the curves (AUC $\leq$ 1) are provided. The figures clearly show that classification with SVM using the combinatory features has higher AUC than those of using fractal features and Fourier power spectrum feature only, which demonstrates the power of the combinatory feature for classification.

Figures 5.28c, 5.29a, 5.29c and 5.30a show the curves for each of the methods on vasculature segmented by different methods (automatically segmented by the Hessian–based vessel filter, the line filter, the combinatory filter, and manually segmented by VK and AH). The figures show that classification achieved higher accuracies on vasculature segmented automatically using the combinatory vessel filter, compared with those segmented using the Hessian–based vessel filter and the line filter. Although classification on vasculature segmented manually performed the best, the method is very time-consuming and requires user intervention.

The corresponding box plots are shown in Figures 5.27, 5.28, 5.29, and 5.30. Classification using the combinatory feature performs consistently better than other methods on vasculature segmented using the combinatory vessel filter, with higher accuracy and low error on different datasets.

5.3.2 Diabetic Retinopathy Classification

Diabetic retinopathy is a microvascular complication of diabetes, causing abnormalities in the retina, and it may eventually lead to blindness [175]. Although we have tested the performance of the proposed method for distinguishing healthy and pathological retinal vasculature from STARE and MESSIDOR, those two databases were not established to study diabetic retinopathy. Moreover, automatic diagnosis of diabetic retinopathy from retinal fundus images has been a challenging task due to the lack of representative image database with a verified ground truth.

In this section, 40 images were selected from the DIARETDB dataset to further evaluate the general performance of diagnosis ability of the proposed method from Section 3.3. The dataset consists of 40 colour fundus images of which 20 are normal and 20 contain signs of diabetic retinopathy (hard exudates, soft exudates, micronaneurysms, haemorrhages, and neovascularisation). Example original funds

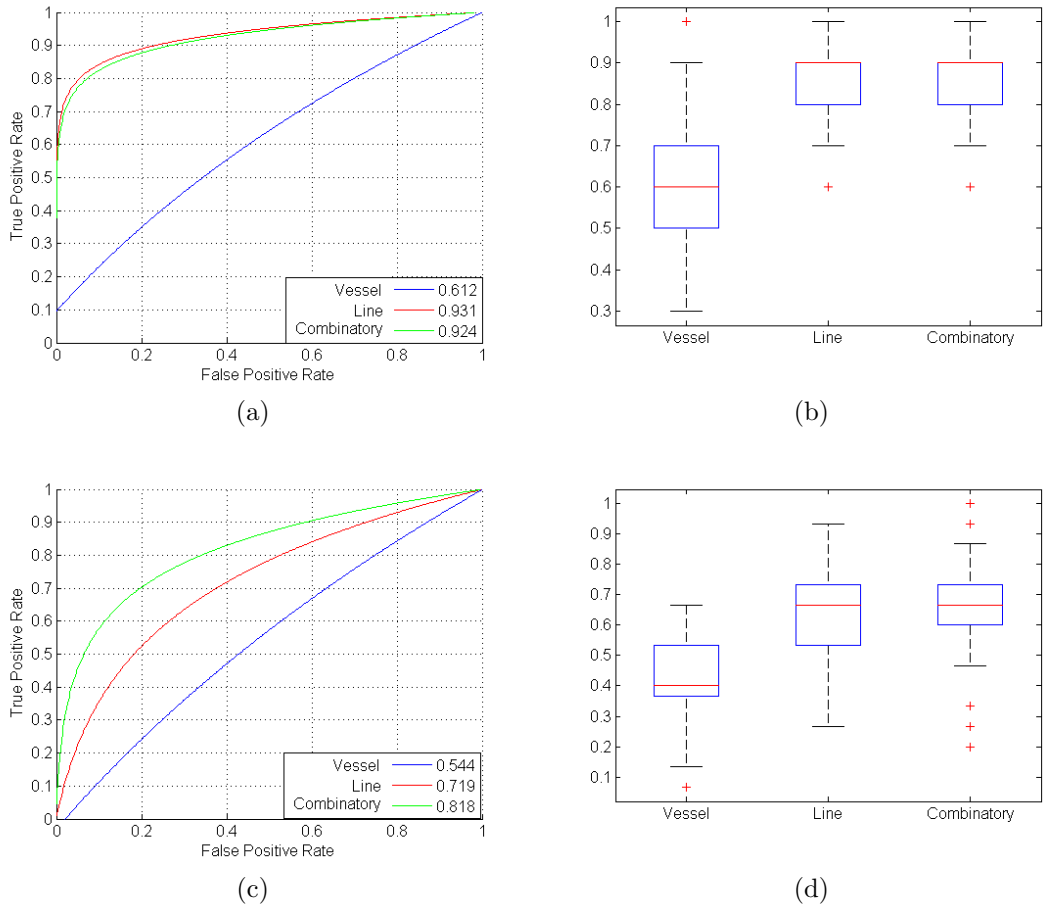
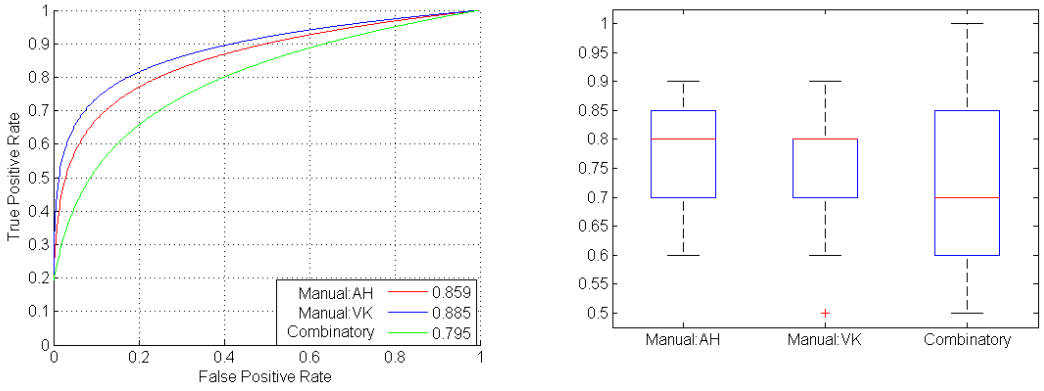


Figure 5.29: ROC analysis with area under the curve (AUC) and box plots on the STARE dataset segmented by the Hessian–based vessel filter, the line filter, and the combinatory vessel filter. SVM results using the combinatory features for classifying (a)(b) two classes and (c)(d) three classes respectively.

images and segmentation images are shown in Figure 5.31.

Figure 5.32 shows the multifractal spectra and Fourier power spectra of retinal vasculature automatically segmented using the combinatory vessel filter from the DIARETDB datasets. Both multifractal spectra and Fourier power spectra of diabetic retinopathy vasculature are higher than those of healthy vasculature because the pathology is indicated by the density and tortuosity of the vasculature.

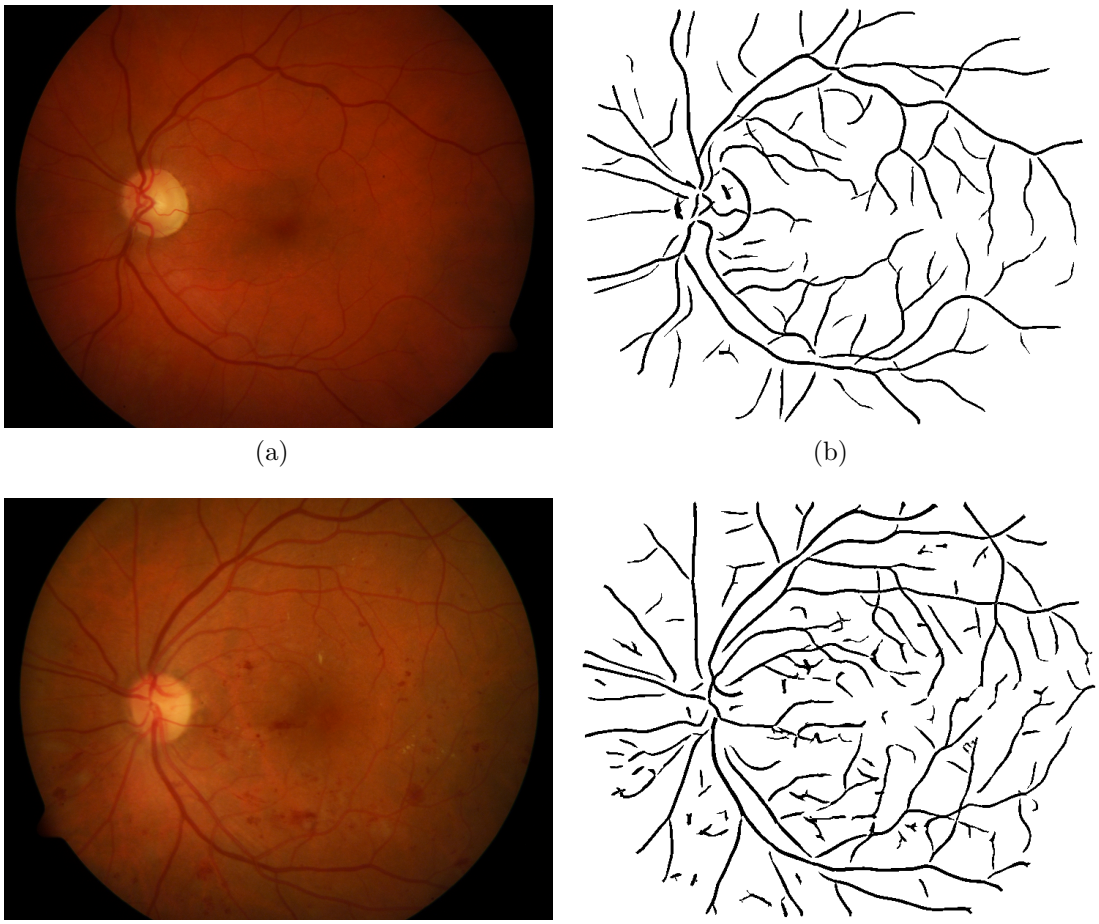
The dataset is then split in half, one as a training set and one as a test set, each



(a) (b)

Figure 5.30: (a) ROC analysis with area under the curve (AUC) and (b) box plots on the STARE dataset manually segmented by VK and AH, and automatically segmented by the combinatory vessel filter, SVM classification results using the combinatory features for classifying two classes.

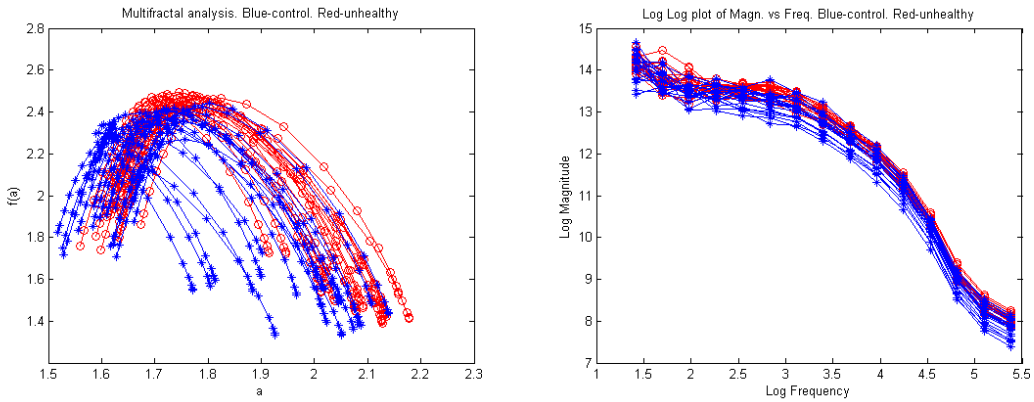
containing 10 healthy and 10 pathological retinal vascular images. The classifier is trained using the training set and tested using the test set. The process is repeated 100 times and the results are averaged. Experiments showed that the method has obtained a classification accuracy of 81.2% using the combination of the multifractal feature and and Fourier fractal feature. The accuracy is not significantly higher than in other research using different approaches, such as based on the detection of exudates [176], for diagnosis of diabetic retinopathy. But we believe that the idea behind the approach is novel, and the performance of the classifier is sufficient to suggest some value in the proposed method and that it can potentially be used as a tool for the study of eye diseases.



(a) (b)

(c) (d)

Figure 5.31: Example vessel segmentation on images from DIARETDB: (a) retinal image and (b) segmented vascular image of a diabetic patient; (c) retinal image and (d) vascular image of a healthy patient.



(a) (b)

Figure 5.32: Multifractal analysis of 20 healthy and 20 pathological (background diabetic retinopathy) retinal vasculatures from DIARETDB: (a) $\alpha/f(\alpha)$ spectra of vasculatures automatically segmented by the combinatory vessel filter respectively. (b) Fourier power spectra of vasculature automatically segmented by the combinatory vessel filter respectively.

5.4 Summary

This chapter demonstrated the performance of the vessel segmentation method and feature extraction on several publicly available retinal databases. Apart from further demonstrating that the proposed vessel segmentation method can produce higher accuracy than the vesselness filter and the line filter, experiments have shown that the combination of features extracted from both types of spectra is the most effective for discriminating healthy and pathological (diabetic and muscular edema) retinal vessels even when only small training sets for the classifier are available. Experiments have also shown that the classification accuracy can be affected not only by the natural differences of retinal vessels in different people but also by the accuracy of vessel segmentation algorithms.

Chapter 6

Case Study 3: Microglial Histology Data

Alzheimer 's disease is a progressive brain disorder characterised by amyloid plaques and neurofibrillary tangles, and it is more prevalent in women than men. Neuroinflammation is one of the main events responsible for the cognitive decline, and it involves the activation of microglia. Lipopolysaccharide (LPS) is used to trigger acute neuroinflammation response through the binding to the microglial exclusive toll-like receptors-4 (TLRs4), and is associated with a transient sickness syndrome. We have built a system to help neuroscientists from the University of Nottingham to assess the susceptibility of Alzheimer 's disease (AD) mouse model to LPS by analysing microglia density and activation at 4 hours post-injection, with a particular focus on sex differences. Details of the method are given in this section. The flowchart of this chapter can be viewed in Figure 6.1.

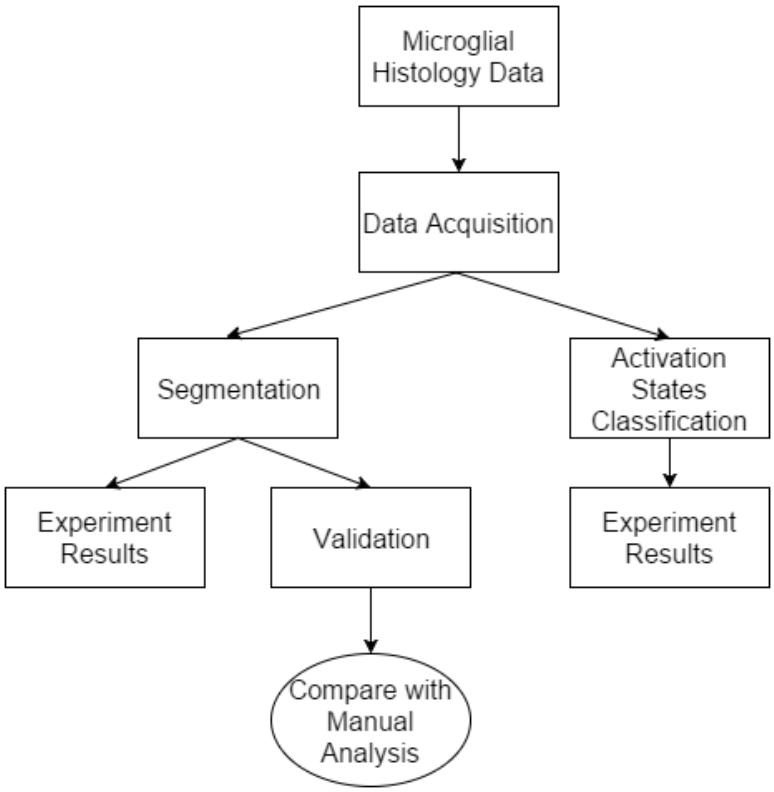


Figure 6.1: Flowchart of case study 3.

6.1 Data Acquisition

The data were generated from brain tissue collected 4 hours after treatment with lipopolysaccharides (LPS, 100ug/kg, i.v.) to activate microglia or its vehicle phosphate buffered saline (PBS), post fixed in 4% paraformaldehyde for at least 24h at 4°C and embedded in paraffin wax on a tissue embedding station (Leica TP1020). Then 7μm-thick coronal sections were cut throughout the hippocampus, using a microtome (Microtome Slee Cut 4060), mounted on APES-coated slides and dried overnight at 40°C. Immunostaining was carried out using standard procedures at room temperature. All the solutions were freshly prepared using PBS + 1% Tween 80, except DAB solution, which was prepared in distilled water. Briefly, the tissue was rehydrated in consecutive rinses in xylene, 100% ethanol, 70% ethanol, and distilled water. Antigen retrieval was performed by incubation in sodium citrate buffer at 95-99°C, followed by incubation in 1% H2O2 (Sigma Aldrich, St. Louis, MO, USA). Tissue was then blocked in 5% normal goat serum, incubated in rabbit polyclonal anti-Iba-1 primary antibody (1:6000; WAKO Chemicals, VA, USA) for 1h followed by 30 minutes incubation with anti-rabbit secondary antibody (1:200; Vector Laboratories Inc. Burlingame, CA). After washing, sections were incubated with Vectastain Elite ABC kit (Vector Laboratories Inc. Burlingame, CA) and labelled with DAB peroxidase substrate (Vector Laboratories, Burlingame, CA) according to manufacturer 's instructions. Sections were then counterstained with haematoxylin and eosin and mounted with DPX-mount media. All procedures were approved as required under the UK Animals (Scientific Procedures) Act 1986. Female AD mice (APPswe/PS1dE9 n=19) or wild type (WT) controls (C57b6, n=19) were used in the study.

Digital focused photo-scanning images were acquired using a Hamamatsu

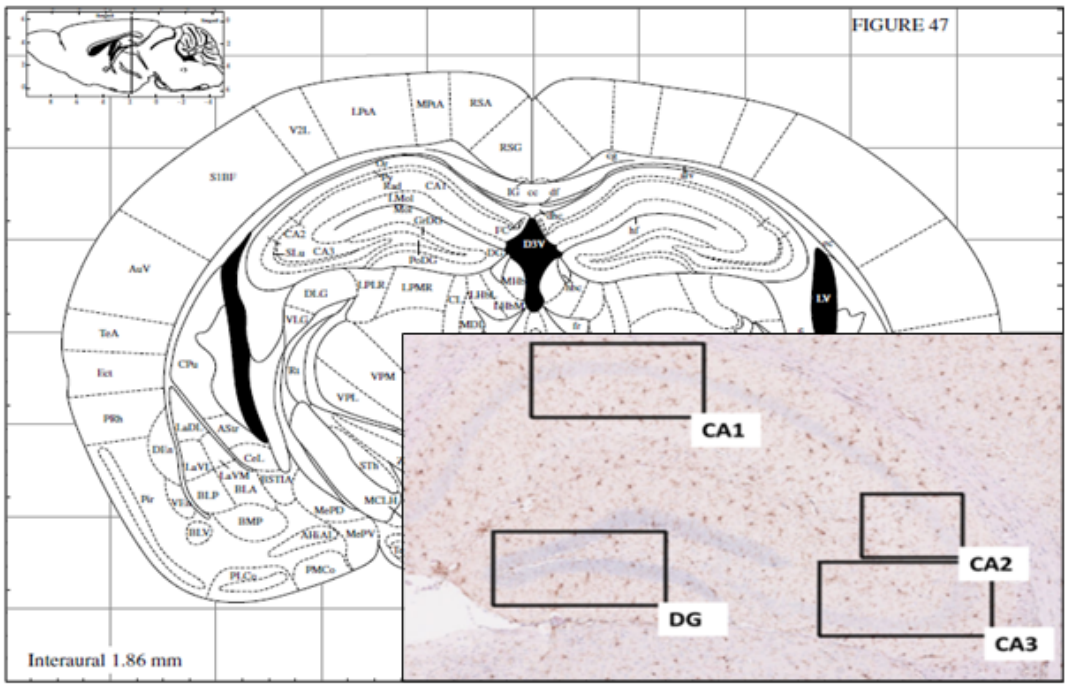
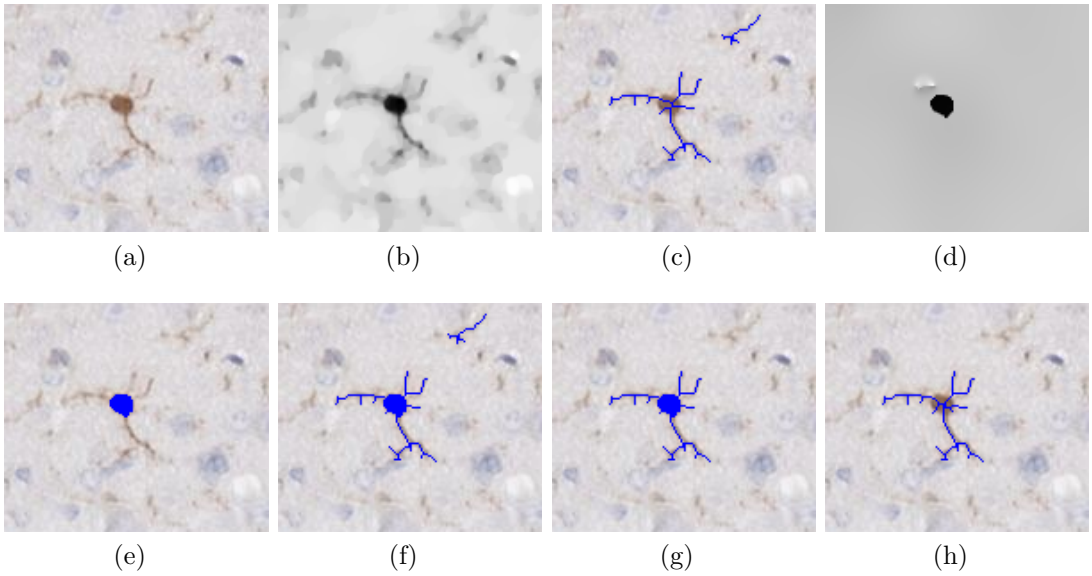


Figure 6.2: (a) Identification of hippocampal subfields using the Franklin and Paxinos Altlas [177].

NanoZoomer-XR with TDI camera technology. Rectangular region of interest (ROIs) were drawn for each hippocampal subfields with an area of 0.2mm^2 for CA1, CA3, and DG, and 0.1mm^2 for CA2 (Figure 6.2) using NDP.view2 (NanoZoomer Digital Photography).



(a) (b) (c) (d)

(e) (f) (g) (h)

Figure 6.3: (a) Cropped image, (b) smoothed image ($\alpha = 10$) (c) microglia processes, (d) smoothed image ($\alpha = 150$), (e) microglia soma, (f) combined microglia processes and soma, (g) full microglia, (h) skeleton of microglia.

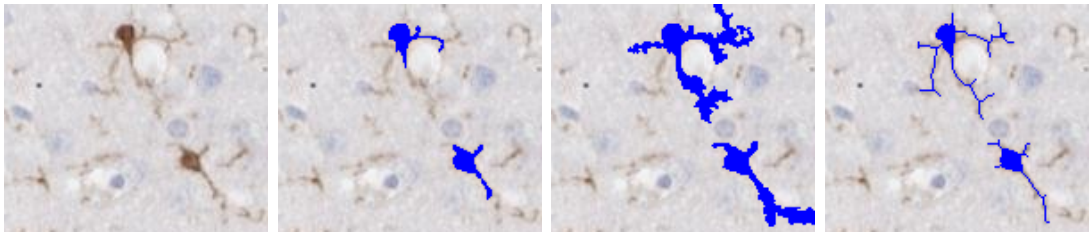
6.2 Segmentation

6.2.1 Workflow

Example segmentation results of a denoised images are shown in Figure 6.3, where Figure 6.3c shows the segmented microglia processes and Figure 6.3e shows the microglia soma.

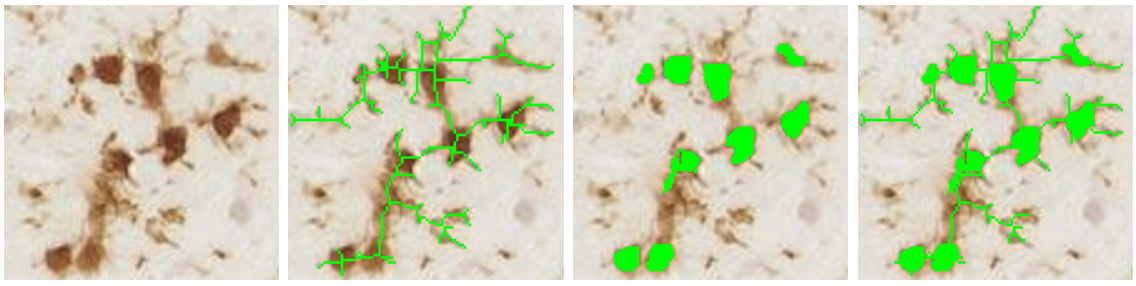
The segmentation method is compared with the thresholding and level set segmentation methods [101]. The thresholding method failed to identify faint microglia processes, and the level set method failed to identify the complete processes (Figure 6.4). The proposed method, however, performed well.

For some cases, microglia clusters are found in the hippocampal region of the brain with Alzheimer's disease. Figure 6.5 shows an example microglia cluster image, along with skeleton, soma, and multifractal spectrum images. The number



(a) (b) (c) (d)

Figure 6.4: (a) Cropped microglia image, (b) microglia segmentation using simple thresholding, (c) microglia segmentation using level set, (d) microglia segmentation using the proposed method.



(a) (b) (c) (d)

Figure 6.5: (a) Microglia cluster image, (b) microglia skeleton, (c) microglia soma, (d) microglia skeleton and soma.

of microglia in a cluster can be identified by counting the somas.

Figure 6.6 shows the workflow of the proposed method on an example microglia histology data.

6.2.2 Validation

Previous studies have described several problems and limitations of the existing methods [49]. This includes: microglia contrast issues within the same image, large artefacts, different visual textures within the same field of view, and textures that blurs the distinction between microglial cell and background: examples of these problems are shown in Figure 6.7. Experiments show that the proposed

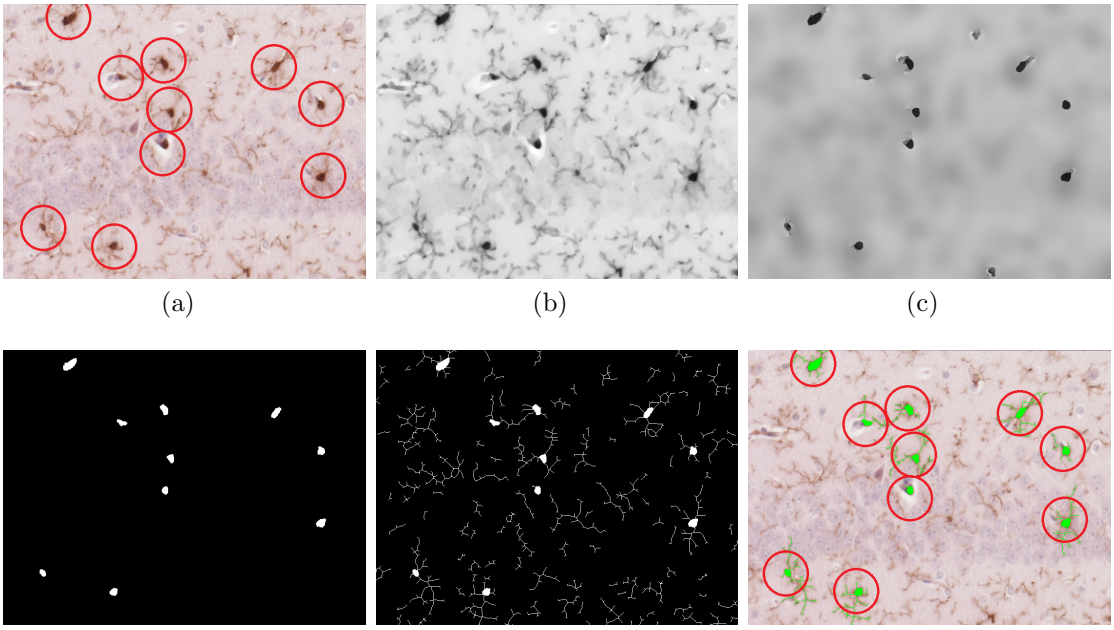


Figure 6.6: Workflow of the proposed segmentation for a sample image: (a) original histology image, (b) smoothed image ($\alpha = 10$), (c) smoothed image ($\alpha = 300$), (d) microglia soma segmentation, (e) microglia soma and processes segmentation, (f) automatically labelled microglia overlaid onto the histological image.

segmentation method is accurate and overcomes the common problems that were described earlier; example segmentation results are shown in Figure 6.7.

Twenty images were used for validation of the proposed automated technique against manual analysis. For manual segmentation, the soma of microglial cells was delineated using the freehand line tool in NDP.view2 at a magnification of 40× and the data (number of soma per ROI and soma size in μm^2) extracted. ROIs were exported 20× and saved as Jpeg images for subsequent analysis of the percentage of area stained, using ImageJ [53]. Images were split into red, green, and blue using the RGB stack command, prior to thresholding. The blue stack was chosen to eliminate non-specific highlighting of the neuronal nuclei. The threshold level was adjusted manually, to highlight the soma and processes, and

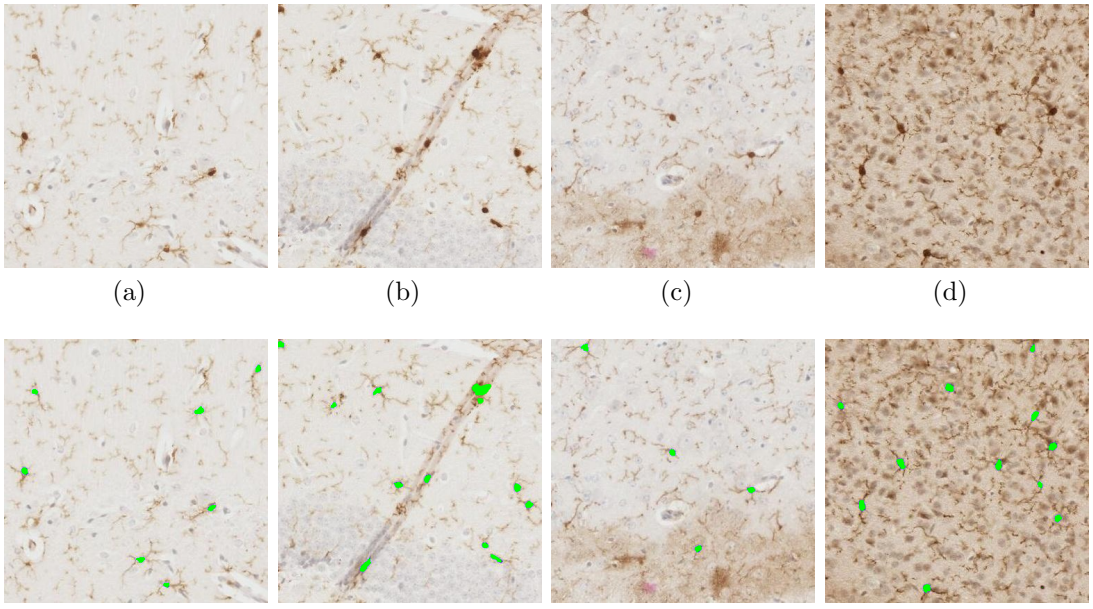


Figure 6.7: Challenges described in a previous study and overcome using the proposed method [49]: (a) image shows microglial cells with strong and weak intensities, (b) image has a large complex artefact with microglia located partly inside the artefact, (c) image shows two regions that exhibit different visual textures, (d) image displays a complex texture appearance that blurs the distinction between microglial cell and background pixels, (e)-(h) Microglia soma labelled using the proposed method.

the percentage area stained extracted.

An example automated segmentation result using the proposed method for analysing the number of soma per ROI and soma size in μm^2 is shown in Figure 6.8e, and the analysis of the percentage of area stained is shown in Figure 6.8f. The results from the proposed automatic method and the manual method on the image dataset are compared. As shown in Figure 6.9, the proposed method has produced similar results to those obtained by the manual method for the number of cells per ROI, though the proposed method produced slightly higher error rate due to the artefact in the histology image, examples of which are shown in Figure 6.10. These artefact can compromise the accuracy of the automated segmentation

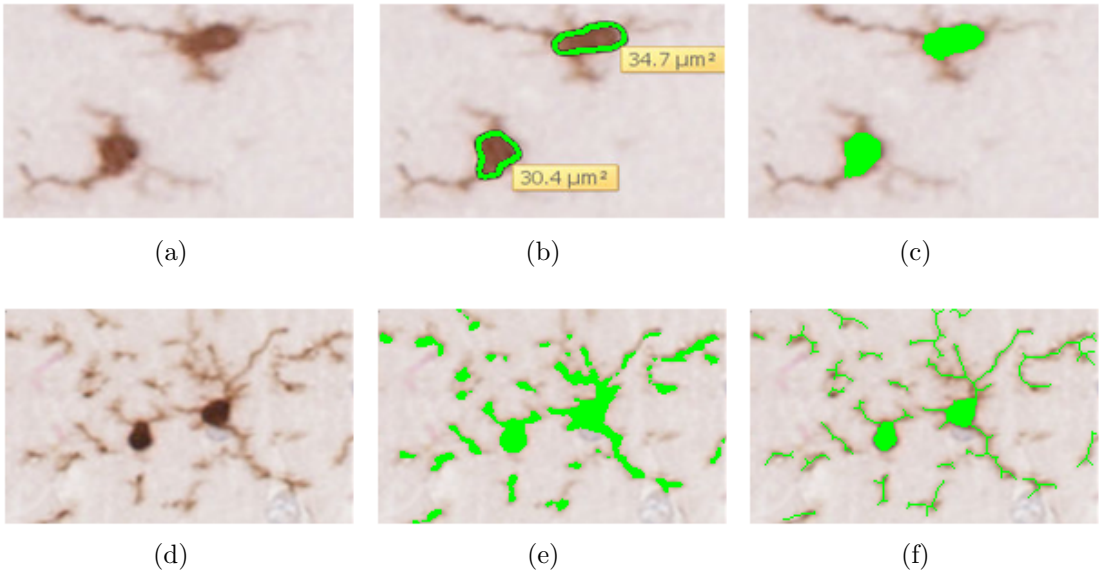
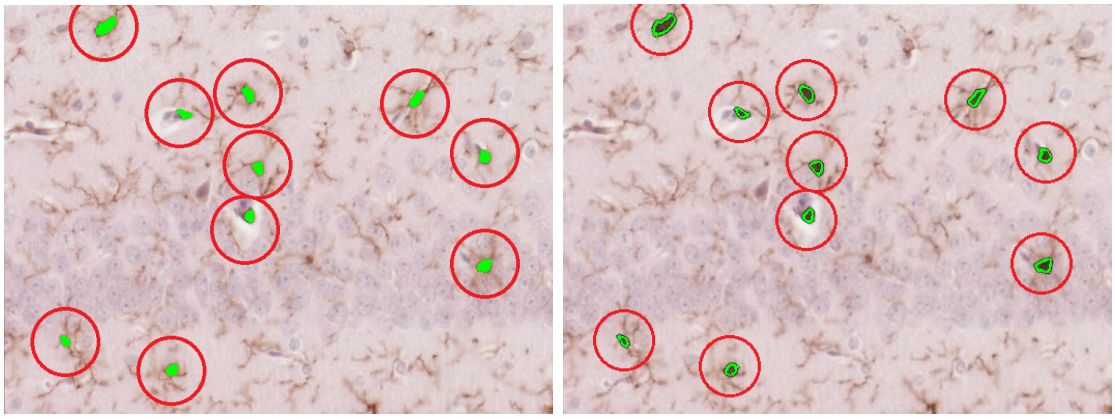
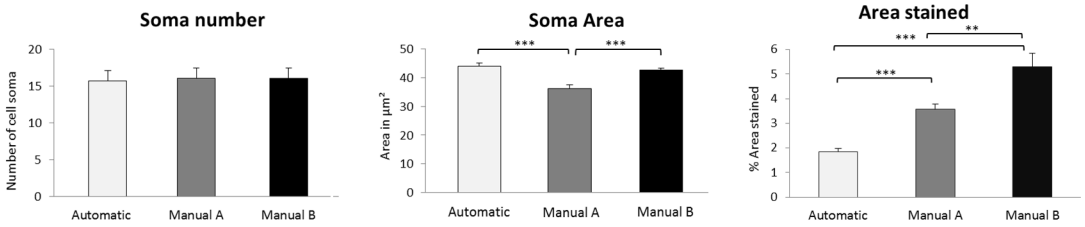


Figure 6.8: Examples of soma area estimation, and estimation of the percentage of the area stained: (a) and (d) Iba-1 positive microglial cells in unprocessed images, (d) freehand delineation of microglial somas and annotation of the soma size calculated by NDP.viewer2 software, (c) soma segmentation by the proposed method, (e) example of manually adjusted threshold level for the estimation of the percentage of area stained by Iba-1, (f) example of automatic estimation of the percentage of area stained by Iba-1.

method, but they can be removed manually. For soma size, the proposed method is more accurate. Differences between scorers for the manual analysis are due to differences in judgement in defining the border of the soma. The proposed method is better than the manual method for percentage area stained, which is very dependent upon the scorer's judgement, leading to inconsistencies between scorers (Figure 6.8) as it can be compromised by background staining, counterstaining of neuronal nuclei, and inhomogeneities in tissue.

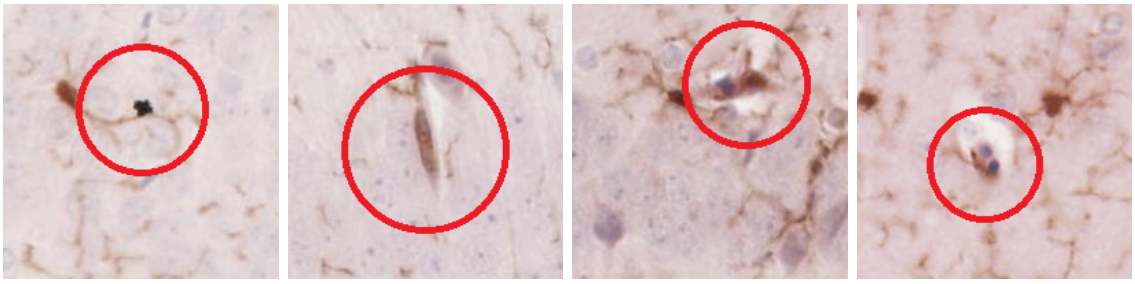


(a) (b)



(c) (d) (e)

Figure 6.9: Comparison of segmentation results using the proposed segmentation method and the manual segmentation method: (a) Microglia soma segmented using the proposed automatic segmentation method; (b) Microglia soma manually segmented by the expert. Analysis results calculated using automatic and manual segmentation methods within the hippocampus; (c) Soma number; (d) Soma area. ***, p¡0.0001. Statistically significant differences between scorers and between some scorers and automated method; (e) Percent area stained. **, p¡0.01. ***, p¡0.0001. Statistically significant differences between scorers and between scorers and automated method. Automatic: results produced by the proposed method. Manual A and Manual B: results produced by the experts.



(a) (b) (c) (d)

Figure 6.10: Artefacts that the proposed method incorrectly detected as microglia.

6.3 Microglia Activation States Analysis

Apart from the features extracted using the method previously introduced in Section 3.3, lacunarity, which describes the heterogeneity of fractal structures, is also taken into consideration to complement fractal dimension by measuring how the data fills the space [44]. A box-counting algorithm is used for estimating lacunarity [178]. The algorithm uses a unit box of size r to glide over the entire image. The number of points within the box (mass p) is counted at each step, and a distribution of box masses $B(p, r)$ is created at the end of gliding. The distribution is then converted into a probability distribution $Q(p, r)$ by dividing the total number of boxes $B(r)$ of size r:

$$Q\left(p, r\right) = \frac{B\left(p, r\right)}{B\left(r\right)} \tag{6.1}$$

Lacunarity is then defined as the division of first and second moments of the box mass probability distribution:

$$L\left(r\right) = \frac{\sum_p pQ\left(P, r\right)}{\left(\sum_p p^2 Q\left(P, r\right)\right)^2} \tag{6.2}$$

Figure 6.11b shows multifractal spectra of the same microglia image rotated in eight directions. It is clear that the fractal spectra for all the images are the same. Being orientation invariant is one of the advantages of multifractal analysis, as the same structure may appear in different orientations in images, and image analysis methods should be robust to these orientation variations.

Figure 6.11d shows multifractal analysis of microglia at different stages: activated, slightly ramified, partially ramified, and fully ramified. It can be seen that

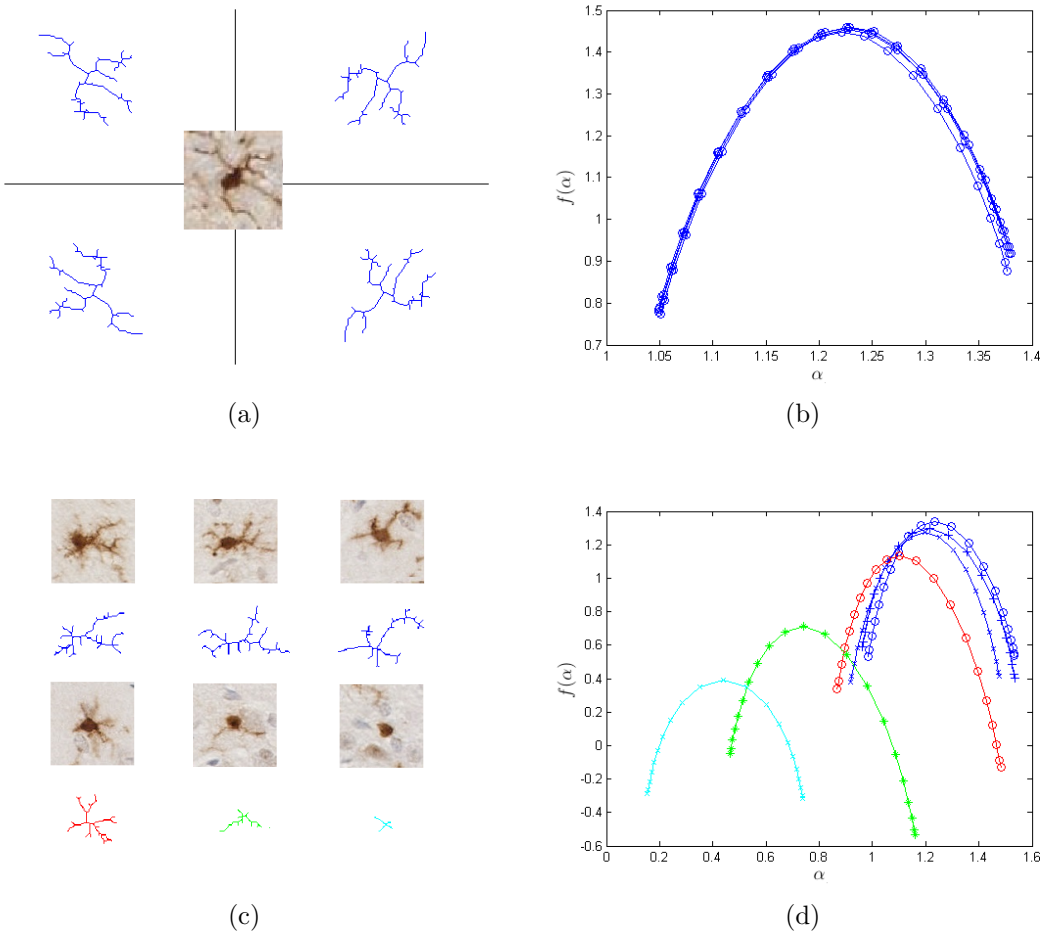
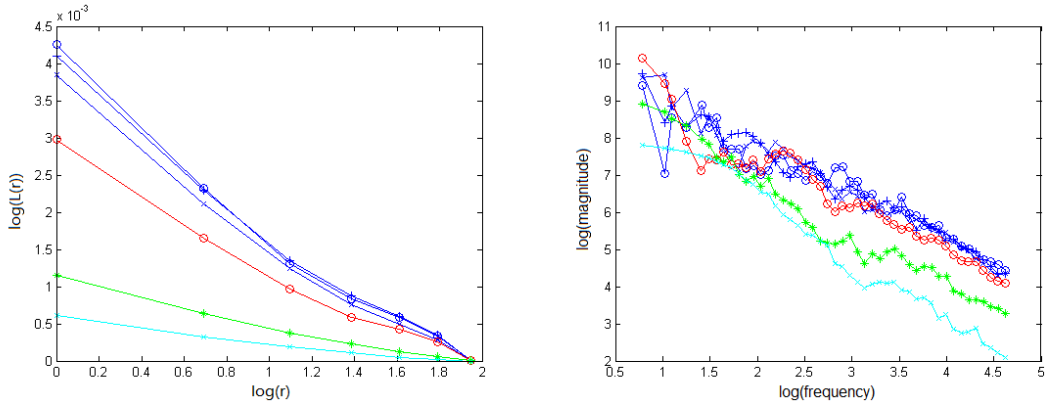


Figure 6.11: Multifractal spectra of microglia: (a) segmented microglia rotated in four different directions, (b) multifractal $\alpha/f(\alpha)$ spectra of the microglia, (c) segmented microglia at four common activation stages, (d) multifractal $\alpha/f(\alpha)$ spectra.

the multifractal spectra of the microglia in different stages are distinctly different. The multifractal spectra of less ramified microglia shift to the left, with lower values compared to those of more ramified microglia. There is little difference in the shapes of the multifractal spectra of the microglia in the same stage, but each of them is slightly shifted in position from the others. This is due to the complexity of the microglia.

Figure 6.12a shows some example lacunarity plots of microglia at different



(a) (b)

Figure 6.12: (a) Lacunarity plot, (b) Fourier power spectra in log-log scale of the microglia in Figure 6.11 at four common activation stages.

stages. The plots of the four classes become separated at the beginning of the plots, more ramified microglia have higher lacunarity values than less ramified microglia as it is 'less rotationally invariant'. This is in agreement with the results in [44]. The value of lacunarity at the beginning of the plot is taken as the lacunarity feature.

Figure 6.12b shows some example Fourier power spectra of microglia at different stages. The power spectra of the four classes become more separated near the end of the log-log power spectra.

In summary, the features extracted from the microglia for classification are the multifractal features (the peak of the multifractal spectrum (f_0) and the symmetry features $\alpha_{\max} - \alpha_0$ and $\alpha_0 - \alpha_{\min}$), the lacunarity value at the smallest scale (L_{min}), and the Fourier features (FFD and the FPS magnitude values at high frequencies).

Performance Evaluation of the Method for Classification To evaluate the performance of the extracted multifractal features for classification, 500 microglia are first extracted from a selected histology image and divided into four groups

based on their morphologies. Multifractal analysis is performed on the segmented microglia to obtain multifractal spectra, and features are extracted from the spectra. Eight sets of features are used for microglia activation state classification in the experiments. Figure 6.13 shows the multifractal spectra, the Fourier power spectra, and the lacunarity plots of all 500 microglia, and the plots are colour coded to represent the different activation states of the microglia. It can be seen that the plots of the four classes are separated. Figures 6.13d, 6.13e, and 6.13f show that the plot of four classes using three features is more discriminating than the plots using two features. The results indicate that there is a good basis for automated classification of the microglia using the extracted fractal features.

To evaluate the performance of the proposed feature extraction methods for classification, a nonlinear support vector machine (SVM) classifier with Gaussian radial basis function (RBF) kernel [174], which was introduced in Section 2.3.1, is chosen for classification of the extracted microglia features.

The dataset is split into two halves, one as training set and the other as a test set, each containing an equal number of microglia images in different activation states. The classifier is trained using the training set and tested using the test set. The process is repeated 100 times, and the results are averaged. The classification results are shown in Table 6.1. Results show that SVM performed poorly on monofractal dimension features (f_0, FFD, L_{min}) of the microglia. The use of the combinatory features achieved the highest classification accuracy (94.27%).

Performance of features extracted from the original microglia images was also evaluated and compared with the proposed methods using multifractal features. Gabor wavelets were applied directly to the greyscale microglia images. Results show that SVM performed poorly using the features from the microglia images. This is because the classification is affected by the orientation of the microglia

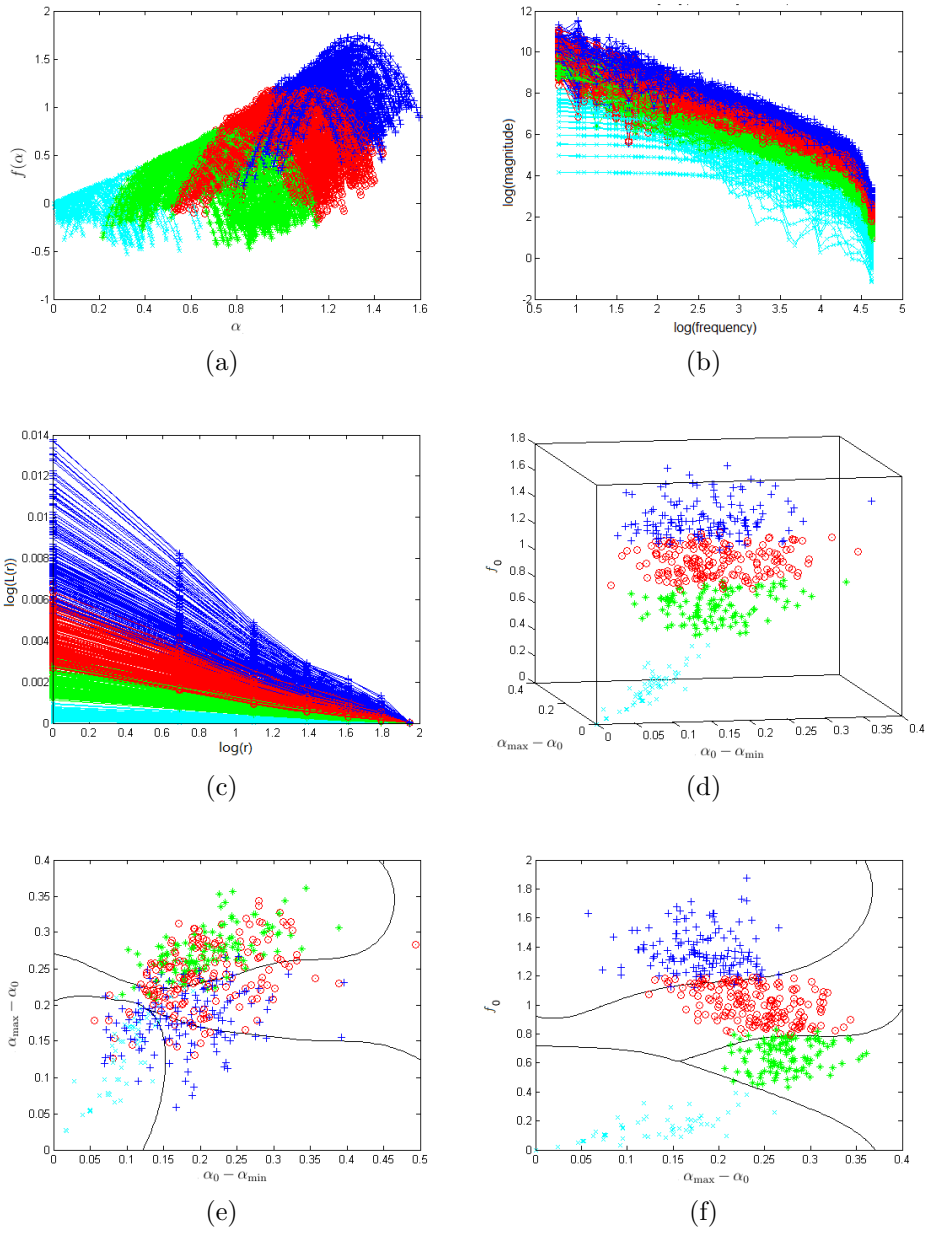


Figure 6.13: Multifractal analysis of microglia at four common activation stages: (a) multifractal $\alpha/f(\alpha)$ spectra, (b) Fourier power spectra in log-log scale, (c) lacunarity/box-size plot, (d) feature of the multifractal spectra in (a) $\alpha_0 - \alpha_{min}$ / $\alpha_{max} - \alpha_0$ /f_0, (e) feature of the multifractal spectra $\alpha_0 - \alpha_{min}$ / $\alpha_{max} - \alpha_0$, (f) feature of the spectra in (a) $\alpha_{max} - \alpha_0$ / f_0. The boundary curve (by SVM classifier) shows a clear difference between the four classes.

	Number of Features	Feature Descriptions	Feature Names	Accuracy
Mono Fractal Features	1	Peak of Multifractal Spectrum	f_0	93.17%
	1	Slop of Fourier Power Spectrum	FFD	45.62%
	1	Lacunarity Value (at Minimum Scale)	L_{min}	90.32%
Multi Fractal Features	3	Combination of Three Mono Fractal Features	f_0+ FFD+L_{min}	93.15%
	3	Peak of Multifractal Spectrum+ Symmetry Feature	f_0+ $\alpha_0 - \alpha_{min}$+ $\alpha_{max} - \alpha_0$	91.08%
	4	Peak of Multifractal Spectrum+ Symmetry Feature, Lacunarity Value	f_0+ $\alpha_0 - \alpha_{min}$+ $\alpha_{max} - \alpha_0$+ L_{min}	93.92%
	4	Slop of Fourier Power Spectrum+ Fourier Power Spectrum Magnitude Values at High Frequencies	FFD+FPS feature	86.25%
	8	Combinatory Fractal Features	f_0+ $\alpha_0 - \alpha_{min}$+ $\alpha_{max} - \alpha_0$+ L_{min}+ FFD+ FPS feature	**94.27%**
Gabor Features	40	Gabor Features Extracted From Greyscale Microglia Image	Gabor Features	21.65%

Table 6.1: Classification accuracy with SVM on different features.

and the illumination of the images. In contrast, the proposed methods using multifractal features produced good classification accuracy.

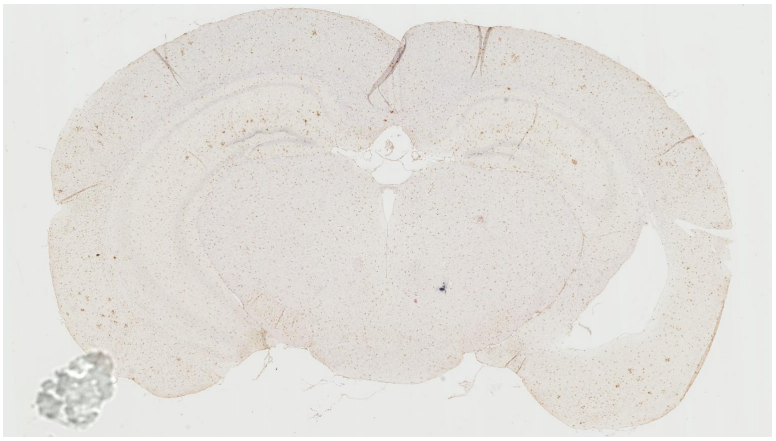
6.4 Summary

Once microglia are segmented and their activation stages are determined through SVM classification, analyses of selected regions in the histology image can be achieved. The scalability of the proposed methods on large datasets is tested in the analysis of microglial distribution in images of both healthy mouse brain and Alzheimer's disease mouse brain models, each of which is 8640×15360 in size. An example of these images is shown in Figures 6.14 and 6.15. Zoomed-in hippocampal regions are shown in Figures 6.14b, 6.14c, 6.15b and 6.15c, and density map images are shown in Figures 6.14d and 6.15d. From these it can be seen that there are more microglial cells in the hippocampal region of the Alzheimer's disease brain.

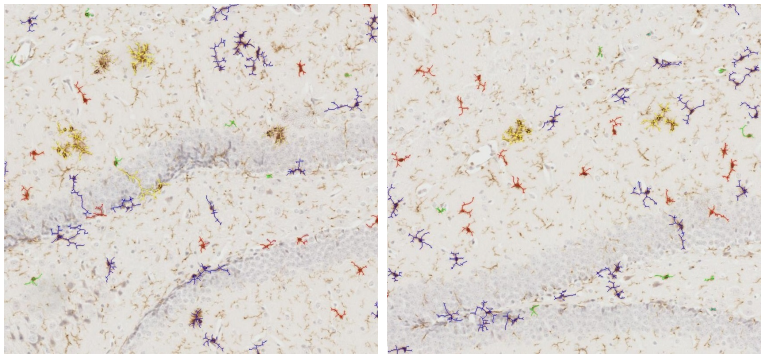
With the help of our system, our collaborators have concluded that LPS had no effect on microglia, but a higher microglial density in CA2, CA3, and DG and lower microglia activation were observed in APPswe/PS1dE9 compared to wild-type female. In addition, wild-type female showed reduced microglial density in CA3 and DG but higher microglia activation compared to wild-type male. These data show that LPS did not show a higher susceptibility of APPswe/PS1dE9 mice compared to wild-type mice, regardless of sex. But improvement in spatial working memory was observed in the APPswe/PS1E9 female, suggesting a beneficial effect of microglia stimulation. Further work needs to be done to clarify the mechanisms underlying this beneficial effect of microglia on behaviour, in response to an immune challenge.

In this chapter, microglial histology images were used to demonstrate the ability of the proposed microglial cells segmentation method and classification method. Segmentation of both microglia process and soma is achieved through

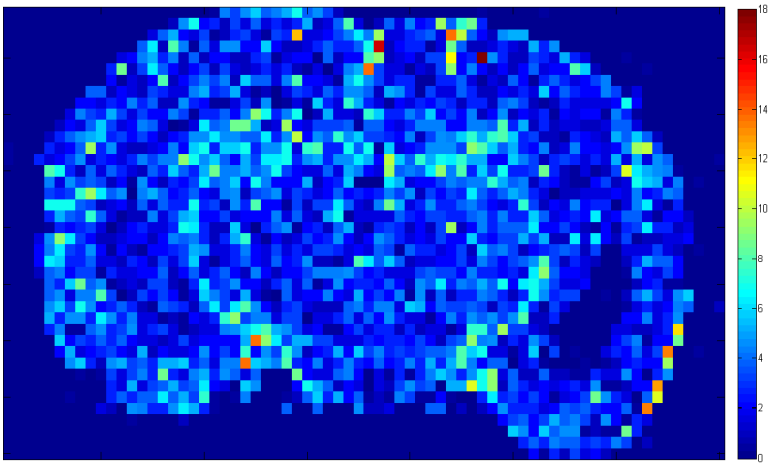
a novel variational method in combination with a fast split Bregman algorithm, which overcomes the problems caused by inhomogeneity of histology images. Experiments show that the proposed methods are fast and accurate and scalable to analysing large microglial datasets.



(a)

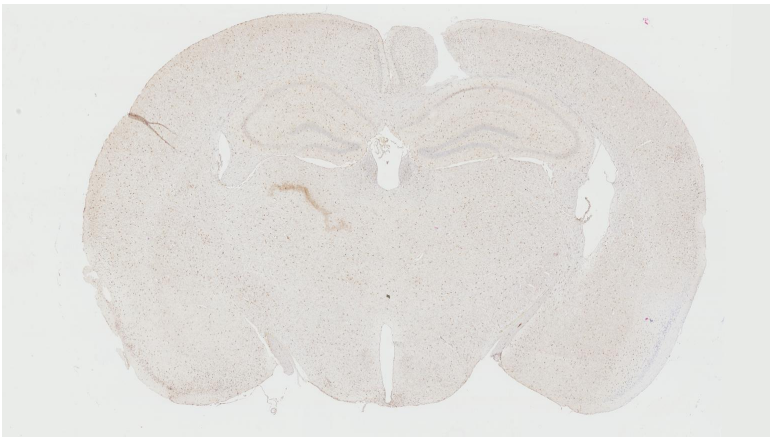


(b) (c)

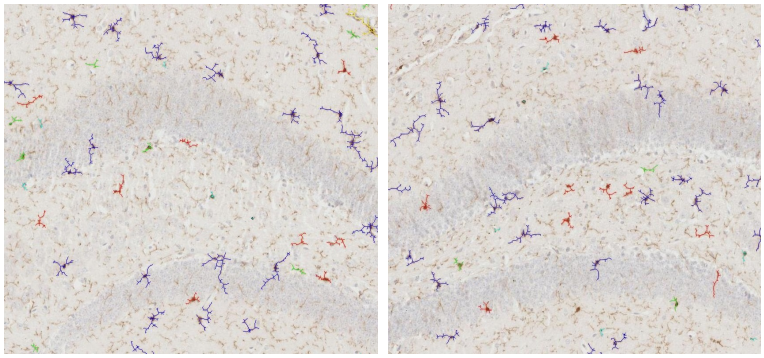


(d)

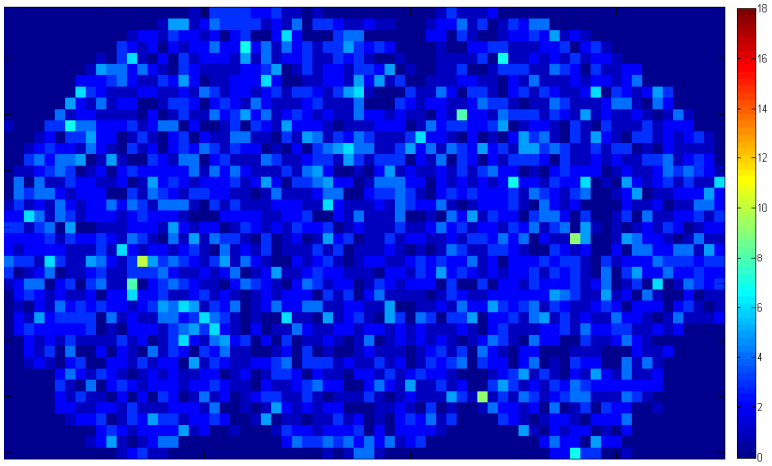
Figure 6.14: Segmentation result of a typical Alzheimer's mouse brain slice (a) the original histology data, the hippocampus being labelled with square boxes; (b)(c) zoomed in hippocampal regions. Microglia are labelled in four different colours. Cyan: activated, Green: slightly ramified, Red: partially ramified. Blue: fully ramified; (d) heat map of the microglial density image and the corresponding colour bar, representing the number of microglia within a square region.



(a)



(b) (c)



(d)

Figure 6.15: Segmentation result of a typical healthy mouse brain slice: (a) the original histology data, the hippocampus being labelled with square boxes; (b)(c) zoomed in hippocampal regions. Microglia are labelled in four different colours. Cyan: activated, Green: slightly ramified, Red: partially ramified. Blue: fully ramified; (d) heat map of the microglial density image and the corresponding colourbar, representing the number of microglia within a square region.

Chapter 7

Summary and Future Work

This thesis addressed several important problems in vascular image analysis. This chapter will give a summary of the contributions of this thesis and some suggestions for future development.

7.1 Summary of Contributions

7.1.1 Improved Vessel Segmentation Method

This thesis first proposed a novel method for 3D brain vessel segmentation that combines a line filter and a Hessian–based vessel filter. Quantitative evaluation of the performance of the method under varying noise levels was performed. The main contribution of this method is that it is a vessel filter framework that is effective in dealing with high–density vessels, including microvessels, and dealing with noise present in images; the method works particularly well on micro-CT and T2*-ffe MRI vessel images.

7.1.2 Novel Fractal Feature Classification Method

A novel machine learning method for feature extraction and classification of retinal vasculature into healthy and pathological ones was introduced. Both methods achieved good classification accuracy, even though only small training sets were available (STARE, MESSIDOR and DIARETDB retinal databases). In practice, classification on multifractal features can be affected by the accuracy of vessel segmentation, as well as by natural differences of vasculature in different people.

7.1.3 Automatic Microglia Analysis Framework

An automated image analysis framework capable of accurately and efficiently segmenting the microglia from histology images and analysing their morphology is introduced. Segmentation of both microglia process and soma is achieved through a novel fast split Bregman algorithm which overcomes the inhomogeneity of histology images and outperforms other segmentation methods. Analysis of

microglia activation stages is achieved through SVM classification of features extracted through multifractal analysis of the microglia. To the best of our knowledge, this is the first time that multifractal analysis has been used to extract features for classifying activation stages of the microglia. Microglia density maps of the whole brain and histograms of microglia in different activation stages are also provided. Experiments show that the proposed framework is accurate and fast, suitable for analysing large datasets.

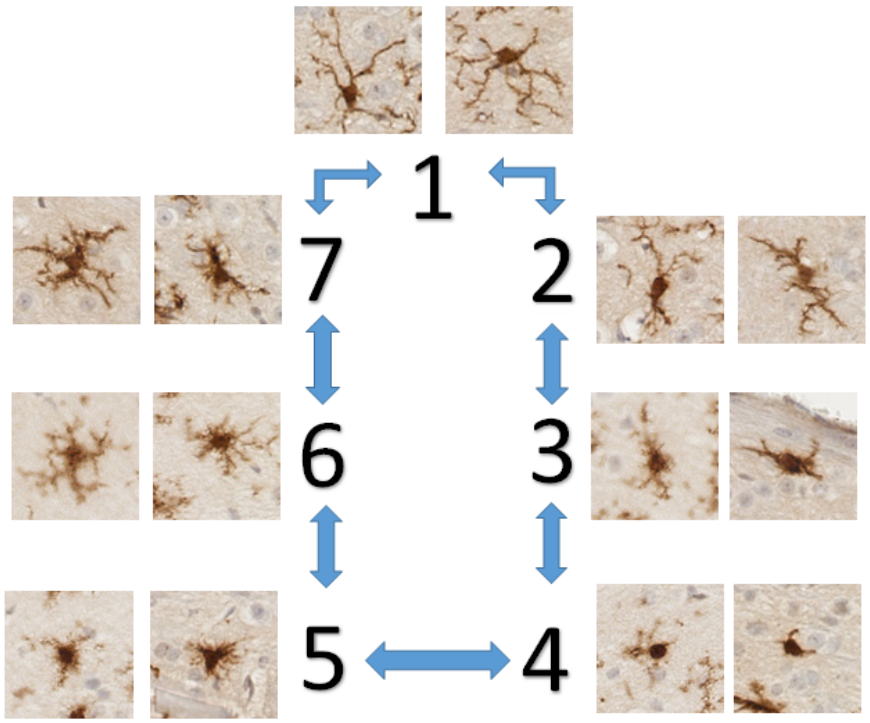
7.2 Future Works

7.2.1 Vascular Analysis on Large Databases

For future work, the segmentation method and postprocessing analysis will be tested on large 3D vascular datasets, potentially containing data from both healthy and pathological patients, along with ground truth images where available. The focus will also include combining filter-based methods with classification based methods to further reduce false vessel detection in case of uncertainty present in images [109, 179]. With a large database of segmented vessels created using the proposed method, further progress can then be made on multifractal analysis and blood flow simulation [180] to investigate vascular development and pathology to complement conventional clinical assessment.

7.2.2 Microglia Activation States Classification

Multifractal analysis was used to extract features for classifying four microglia activation states in this thesis. However, as Figure 7.1 illustrates, a microglial cell can cycle reversibly from a simple rounded to a complex branched form in seven different activation states, including ramified, hypertrophied, bushy, and amoeboid. A review has indicated that there is little research in classification of these microglia activation states [44, 54, 55]. Classification of three microglia activation states (ramified, hypertrophied, bushy) based on fractal features was once presented in [127] but classification accuracies were poor. We have also experimentally produced multifractal spectra of microglia in all seven activation states, as shown in Figure 7.2. The results revealed that there is no signification difference found from the multifractal spectra of microglia in the intermediate

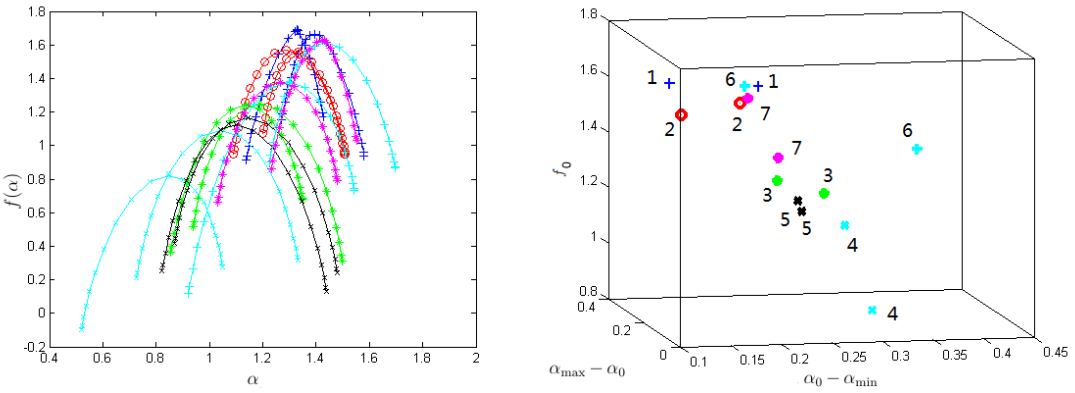


(a)

Figure 7.1: Examples of morphological types of microglia: ramified (1), hypertrophied (2,7), bushy cells (3,6), and amoeboid (4,5).

activation states, thus leaving classification of the states as a challenging job. However, we believe that finding the feature difference between all seven microglia activation states is a potential research direction which could be very important for studying microglia biology.

In addition, the microglia segmentation and analysis framework described in this thesis will be tested on large histology datasets of healthy and diseased brains, along with ground truth images provided by neuroscientists, to validate its sensitivity to disease progression and pro-inflammatory states.



(a) (b)

Figure 7.2: Multifractal analysis of microglia at seven activation stages: (a) multifractal $\alpha/f(\alpha)$ spectra (b) feature of the multifractal spectra $\alpha_0 - \alpha_{min}$ / $\alpha_{max} - \alpha_0$ / f_0. The numbers correspond to the activation states in Figure 7.1.

Chapter 8

Method Implementation Code

This section provides the implementation code for all algorithms which were implemented and illustrated throughout this thesis. The code has been rewritten for easy understanding/reproduction and their origin has been referenced. The added comments/explanation are shown in green colour.

8.1 Local Entropy Thresholding [17]

```
InputImage=rgb2gray(InputImage);
%Convert original colour image to grayscale image
[M,N] =size(InputImage);
CMatrix = zeros(256,256);
for m = 1:M-1
    for n = 1:N-1
        CMatrix(InputImage(m,n)+1,InputImage(m,n+1)+1) =
            CMatrix(InputImage(m,n)+1,InputImage(m+1,n+1)
            +1) + 1;
    end
end
%co-occurrence asymmetrix matrix
%Here CMatrix(i,j) is the (i,j)th entry of the matrix that
    gives
%the number of times the grey level j follows the grey
    level i.

sCMatrix = sum(CMatrix(:));
prob = CMatrix/sCMatrix;
%Here prob is the probability of co-occurrence of grey
    levels i and j,
emax = -100;
for i=1:256
```

```
19      probA = 0;
20      probC = 0;
21      %Here probA is the probability of co-occurrence of
            grey levels i and j,
22      %probA and probC are the probabilities of vessel
            object and background.
23      subProbA = prob(1:i,1:i);
24      probA = sum(subProbA(:));
25      HA(i) = -0.5*(probA*log2(probA+0.0000001));
26      %HA is the total second-order local entropy of the
            object
27      subProbC = prob(i+1:256,i+1:256);
28      probC = sum(subProbC(:));
29      HC(i) = -0.5*(probC*log2(probC+0.0000001));
30      %HC is the total second-order local entropy of the
            background
31      HT(i) = HA(i) + HC(i);
32      if HT(i) >= emax
33          emax = HT(i);
34          ThresholdValue = i;
35          %The value of ThresholdValue which maximises HT
                gives the optimal threshold for vessel
                segmentation.
36      end
37  end
```

```
38
39 OutputImage = 255*ones(M,N);
40 for i=1:M
41     for j=1:N
42         if InputImage(i,j)>=ThresholdValue
43             OutputImage(i,j)=0;
44             %Segment the image using the computed
                   ThresholdValue
45         end
46     end
47 end
```

8.2 Gabor Filter [181]

```
1 InputImage=InputImage(:,:,2);
2 %Convert original colour image to grayscale image
3 OutputImage = zeros(size(InputImage,1), size(InputImage,2)
      , N);
4 for n=1:N
5     sigma = lambda/pi*sqrt(log(2)/2)*(2^bw+1)/(2^bw-1);
6     sigma_x = sigma;
7     sigma_y = sigma/gamma;
8     sz=fix(8*max(sigma_y,sigma_x));
9     if mod(sz,2)==0, sz=sz+1;end
10    [x y]=meshgrid(-fix(sz/2):fix(sz/2),fix(sz/2):-1:fix(-
          sz/2));
```

```
11      x_theta=x*cos(theta)+y*sin(theta);
12      y_theta=-x*sin(theta)+y*cos(theta);
13      GaborWavelet=exp(-0.5*(x_theta.^2/sigma_x^2+y_theta
            .^2/sigma_y^2)).*cos(2*pi/lambda*x_theta+psi);
14      % This creates a n-th Gabor Wavelet
15      % bw is bandwidth
16      % gamma is aspect ratio
17      % psi is phase shift
18      % lambda is wave length
19      % theta is angle in rad
20      OutputImage(:,:,n) = imfilter(InputImage, GaborWavelet
            , 'symmetric');
21      % Filter the InputImage with the GaborWavelet and
            store it to the n-th channel
22      theta = theta + 2*pi/N;
23      % Move to next orientation
24  end
25  OutputImage_show = sum(abs(OutputImage).^2, 3).^0.5;
26  OutputImage_show = OutputImage_show./max(OutputImage_show
        (:));
27  % normalisation to show the final output image
28  % (maximum response to the filter)
```

8.3 Matched Filter [17]

```
1   InputImage=InputImage(:,:,2);
```

```
%Convert original colour image to grayscale image
[M,N] = size(InputImage);
MatchedFilterKernal = exp(-(x.*x)/(2*sigma*sigma));
% Create 1D matched filter kernal
% sigma defines the spread of the intensity profile
MatchedFilterKernal = max(MatchedFilterKernal)-
    MatchedFilterKernal;
MatchedFilterKernal2D = repmat(MatchedFilterKernal,[9  1]);
sht1 = sum(MatchedFilterKernal2D(:));
mean = sht1/(13*9);
MatchedFilterKernal2D = MatchedFilterKernal2D - mean;
MatchedFilterKernal2D = MatchedFilterKernal2D/sht1;
% Create a 2D kernal using 1D matched filter kernal
Kernal2D12Direction{1} = zeros(15,16);
for i = 1:9
    for j = 1:13
        Kernal2D12Direction{1}(i+3,j+1) =
            MatchedFilterKernal2D(i,j);
    end
end
for k=1:11
    ag = 15*k;
    Kernal2D12Direction{k+1} = imrotate(
        Kernal2D12Direction{1},ag,'bicubic','crop');
end
```

```
% Kernal2D12Direction contains matched filter kernal in 12 direction
for k=1:12
    R{k} = conv2(InputImage, Kernal2D12Direction{k}, 'same');
end
% Convole the InputImage with a set of kernels at equiangular
% rotations is applied at each pixel along 12 possible directions
% R is the response image
OutputImage = zeros(M,N);
for i=1:M
    for j=1:N
        ER = [R{1}(i,j), R{2}(i,j), R{3}(i,j), R{4}(i,j), R{5}(i,j), R{6}(i,j) ,...
              R{7}(i,j), R{8}(i,j), R{9}(i,j), R{10}(i,j), R{11}(i,j), R{12}(i,j)];
        OutputImage(i,j) = max(ER);
    end
end
% Produce a final output by retaining the maximum response
```

8.4 Multiscale Vesselness Filter [19]

```
InputImage=InputImage(:,:,2);
```

```
%Convert original colour image to grayscale image
FilterImageforAllScales=zeros([size(InputImage) length(
    MaximumScale)]);
% Make matrices to store all filterd images in difference
    scales
for CurrentScale = 1:MaximumScale,
    % Frangi filter for all scales
    % First, make 2D Hessian matrix
    [X,Y]    = ndgrid(-round(3*CurrentScale):round(3*
        CurrentScale));
    % Make kernel coordinates
    DGaussxx = 1/(2*pi*CurrentScale^4) * (X.^2/
        CurrentScale^2 - 1) .* exp(-(X.^2 + Y.^2)/(2*
        CurrentScale^2));
    DGaussxy = 1/(2*pi*CurrentScale^6) * (X .* Y) .* exp
        (-(X.^2 + Y.^2)/(2*CurrentScale^2));
    DGaussyy = DGaussxx';
    % Build the gaussian 2nd derivatives filters
    Dxx = imfilter(InputImage,DGaussxx,'conv');
    Dxy = imfilter(InputImage,DGaussxy,'conv');
    Dyy = imfilter(InputImage,DGaussyy,'conv');
    % Filters the image with 2nd derivatives of a Gaussian
    Dxx = (CurrentScale^2)*Dxx;
    Dxy = (CurrentScale^2)*Dxy;
    Dyy = (CurrentScale^2)*Dyy;
```

```
21      % Correct for scale
22      tmp = sqrt((Dxx - Dyy).^2 + 4*Dxy.^2);
23      mu1 = 0.5*(Dxx + Dyy + tmp);
24      mu2 = 0.5*(Dxx + Dyy - tmp);
25      % Compute the eigenvalues
26      check=abs(mu1)>abs(mu2);
27      Lambda1=mu1; Lambda1(check)=mu2(check);
28      Lambda2=mu2; Lambda2(check)=mu1(check);
29      % Sort eigen values
30      Lambda1(Lambda1==0) = eps;
31      Rb = (Lambda2./Lambda1).^2;
32      S2 = Lambda1.^2 + Lambda2.^2;
33      FilteredImage = exp(-Rb/beta^2) .*(ones(size(
            InputImage))-exp(-S2/c^2));
34      % Compute the vesselness measures, beta and c are
            constant
35      FilteredImage(Lambda1<0)=0;
36      % Compute the output image, nagative = background
37      FilterImageforAllScales(:,:,CurrentScale) =
            FilteredImage;
38      % store the results in 3D matrices
39  end
40  OutputImage = max(FilterImageforAllScales,[],3);
41  % For every pixel the value of the scale with the maximum
42  % output pixel value is retained
```

8.5 Wavelet Transform Modulus Maxima (WTMM) [91]

```
InputImage=InputImage(:,:,2);
%Convert original colour image to grayscale image
[a,b]=size(InputImage);
A=-1/sqrt(2*pi);
%Construct the partial derivative of gaussian function
for index_x=1:FilterLength;
    for index_y=1:FilterLength;
        x=index_x-(FilterLength+1)/2;
        y=index_y-(FilterLength+1)/2;
        phi_x(index_x,index_y)=A*(x/delta^2).*exp(-(x.*x+y
            .*y)/(2*delta^2));
        phi_y(index_x,index_y)=A*(y/delta^2).*exp(-(x.*x+y
            .*y)/(2*delta^2));
    end
end;
Gx=conv2(InputImage,phi_x,'same');
Gy=conv2(InputImage,phi_y,'same');
% Convolve the image with the gaussian wavelet
IGrads=sqrt((Gx.*Gx)+(Gy.*Gy));
% get gradient intensity
GradientDirection=zeros(a,b);
% get dradient direction
```

```
21 for i=1:a;
22     for j=1:b
23         if (abs(Gx(i,j))>eps*100)  %  if x is bigger
               enough
24             p=atan(Gy(i,j)/Gx(i,j))*180/pi;  % get angel
                  value
25             if (p<0) % 4 quadrant
26                 p=p+360;
27             end;
28             if (Gx(i,j)<0 & p>180) % 2 quadrant
29                 p=p-180;
30             elseif (Gx(i,j)<0 & p<180) % 3 quadrant
31                 p=p+180;
32             end
33         else  %  90?270?
34             p=90;
35         end
36         GradientDirection(i,j)=p;
37         % store direction information
38     end
39 end;
40 OutputImage=zeros(a,b);
41 dn=22.5;
42 for i=2:a-1
43     for j=2:b-1
```

```
44          if ((GradientDirection(i,j)>=(-dn) &
                GradientDirection(i,j)<=dn) | ...
45                  (GradientDirection(i,j)>=(180-dn) &
                        GradientDirection(i,j)<=(180+dn)))
46              % For direction between 0+22.5 and 0-22.5,
                    180+22.5 and 180-22.5 degree
47              if (IGrads(i,j)>IGrads(i+1,j) & IGrads(i,j)>
                    IGrads(i-1,j))
48                  OutputImage(i,j)=IGrads(i,j);
49              end
50          elseif ((GradientDirection(i,j)>=(90-dn) &
                GradientDirection(i,j)<=(90+dn)) | ...
51                  (GradientDirection(i,j)>=(270-dn) &
                        GradientDirection(i,j)<=(270+dn)))
52              % For direction between 90+22.5 and 90-22.5,
                    270+22.5 and 270-22.5 degree
53              if (IGrads(i,j)>IGrads(i,j+1) & IGrads(i,j)>
                    IGrads(i,j-1))
54                  OutputImage(i,j)=IGrads(i,j);
55              end
56          elseif ((GradientDirection(i,j)>=(45-dn) &
                GradientDirection(i,j)<=(45+dn)) | ...
57                  (GradientDirection(i,j)>=(225-dn) &
                        GradientDirection(i,j)<=(225+dn)))
```

```
58              % For direction between 45+22.5 and 45-22.5,
                    225+22.5 and 225-22.5 degree
59              if (IGrads(i,j)>IGrads(i+1,j+1) & IGrads(i,j)>
                   IGrads(i-1,j-1))
60                  OutputImage(i,j)=IGrads(i,j);
61              end
62          else
63              % For direction between 135+22.5 and
                    135-22.5, 215+22.5 and 215-22.5 degree
64              if (IGrads(i,j)>IGrads(i+1,j-1) & IGrads(i,j)>
                   IGrads(i-1,j+1))
65                  OutputImage(i,j)=IGrads(i,j);
66              end
67          end
68      end
69  end
70  %For any point in the original image, two neighbourhoods
       along the gradient direction are compared.
71  %If the edge intensity IGrads is the local maximum,
72  %it is retained and considered as an edge pixel, otherwise
       the point is deleted.
73  for m=1:a
74      for n=1:b
75          if (OutputImage(m,n)>threshold)
76              OutputImage(m,n)=1;
```

```
77            else
78                OutputImage(m,n)=0;
79            end
80        end
81    end
82    % A threshold value is chosen to filter out the noise,
```

8.6 Level Set Basic

```
1  InputImage=InputImage(:,:,2);
2  % Convert original colour image to grayscale image
3  % Parameters
4  % sigma is gaussian blur, larger means less details
5  % alpha controls normal speed, larger approaches zero
       faster in case of edge
6  % beta controls vector field, smaller preserves more
       detail at cost of more ragged edges
7  % time_step controls scaling for time step (how big the
       speed step)
8  % shrink_grow is region behavious, positive = grow,
       negative = shrink
9  % iterations is number of iterations
10 % u_initial is zero level set
11 G = fspecial('gaussian', 30, sigma);
12 I_G = imfilter(InputImage, G, 'symmetric', 'same', 'conv')
       ;
```

```
% gausian kernel and convolution
[I_Gx, I_Gy] = gradient(I_G);
I_Gxy_norm = (I_Gx.^2 + I_Gy.^2).^(1/2);
% Gradient magnitude
NormalSpeed = exp(-alpha * I_Gxy_norm);
% NormalSpeed V_n
[grad_I_Gxy_norm_x, grad_I_Gxy_norm_y] = gradient(
    I_Gxy_norm);
XGradientImage = beta * grad_I_Gxy_norm_x;
YGradientImage = beta * grad_I_Gxy_norm_y;
Time_t = time_step/(max(max(abs(NormalSpeed))) + max(max(
    abs([XGradientImage YGradientImage]))));
Surface = shrink_grow * u_initial;
for n = 1:iterations
    [XGradientSurface, YGradientSurface] = gradient(
        Surface);
    Gradientmagnitude_CurrentSurface = (XGradientSurface
        .^2 + YGradientSurface.^2).^(1/2);
    % Gradientmagnitude
    Surface = Surface - Time_t * (NormalSpeed .*
        Gradientmagnitude_CurrentSurface + XGradientImage
        .* XGradientSurface + YGradientImage .*
        YGradientSurface);
    % evolution of surface using level set function
end
```

```
31 OutputImage=Surface;
```

8.7 Line Filter [126]

```
1  InputImage=InputImage(:,:,2);
2  %Convert original colour image to grayscale image
3  for Scale = 1:MaximumScale
4      avgmask = fspecial('average', MaximumScale);
5      %create a MaximumScale*MaximumScale window
6      avgresponse = imfilter(InputImage,avgmask,'replicate')
           ;
7      % Process the image with mean filter
8      LineResponseImage = -Inf*ones(size(InputImage));
9      % Create LineResponseImage to store the result
10     for theta = 0:15:165
11         linemask = get_linemask(theta,Scale);
12         linemask = linemask/sum(linemask(:));
13         % Draw a Line in theta degree, with a length of
               Scale, each one
14         % with a intensity of 0.1
15         imglinestrength = imfilter(InputImage,linemask);
16         % filter the input image with the line image
               created, so that
17         % pixels reponse the most to the line mask are
               enhanced
18         imglinestrength = imglinestrength - avgresponse;
```

```
19          % remove the original image so that only the
                enhanced pixels are
20          % displayed
21          LineResponseImage = max(LineResponseImage,
                imglinestrength);
22          % Store the enhanced pixels to LineResponseImage
                but keep the
23          % highest intensity value, then repeat the steps
                by creating a new
24          % line mask in theta+15 degree
25      end
26      InputImage = InputImage+LineResponseImage;
27      % Store the repoinse image and move to next scale
28  end
29  OutputImage = InputImage/MaximumScale;
```

8.8 Microglia Segmentation

```
1  InputImage=InputImage(:,:,2);
2  %Convert original colour image to grayscale image
3
4  ColorMap = rgb2hsv(InputImage);
5  % Convert red-green-blue colors to hue-saturation-value.
6  ColorHigh=ColorMap(:,:,1)>0.2;
7  ColorLow=ColorMap(:,:,1)<0.9;
8  BlueColour=(ColorHigh+ColorLow)>1;
```

```
9  % Create a binary image based on the original image, where
       blue-ish color = 1
10
11 LowStrengthSmooth=splitBregmanGSMSTV(InputImage,10,30);
12 % Apply Mumford-Shah Total Variation to the image with 10
       smoothing
13 % strength, for 30 iteration
14 FilterImage=imfilter(LowStrengthSmooth,fspecial('average',
       ws),'replicate');
15 FilterImage=FilterImage-LowStrengthSmooth-C;
16 SegmentedCell=im2bw(FilterImage,0);
17 % Apply an adaptive thresholding algorithm that seperates
       the
18 % foreground from the background with nonuniform
       illumination.
19 % C = threshold mean, ws is the local window size.
20 SkeletonizedCell=bwmorph(~SegmentedCell,'skel',Inf);
21 % Skeltonize the segmented cell using Morphological
       Operations
22 % The method removes pixels on the boundaries of the cells
       before the cells break apart.
23 CellProcesses=(SkeletonizedCell-BlueColour)>0;
24 % Remove the segmented cells those are in color blue
25 CellProcesses=bwareaopen(CellProcesses,20);
```

```
26 % remove any cells and noise those are smaller than 20
       pixels
27
28 HighStrengthSmooth=splitBregmanGSMSTV(InputImage,150,50);
29 % Apply Mumford-Shah Total Variation to the image with 150
       smoothing
30 % strength, for 50 iteration
31 FilterImage=imfilter(HighStrengthSmooth,fspecial('average'
       ,ws),'replicate');
32 FilterImage=FilterImage-HighStrengthSmooth-C;
33 SegmentedCell=im2bw(FilterImage,0);
34 % Apply an adaptive thresholding algorithm
35 CellBody=(SegmentedCell-BlueColour)>0;
36 CellBody=bwareaopen(CellBody,40);
37 % remove any cells and noise those are smaller than 40
       pixels
38
39 OutputImage=(CellBody+CellProcesses)>0;
40 % Combine the segmented cell body and cell processes to
       form the final
41 % segmentation
```

8.8.1 Mumford-Shah Total Variation [8]

```
1 function OutputImage=splitBregmanGSMSTV(InputImage,alpha,
       steps)
```

```
2  [m n]=size(InputImage);
3  u=InputImage;
4  theta=2; beta=1e-1; esp=1e-5;
5  b1=zeros(m,n);
6  b2=zeros(m,n);
7  w1=zeros(m,n);
8  w2=zeros(m,n);
9  v =zeros(m,n);
10 for step=1:steps
11     %%%%%%%%%% update v %%%%%%%%%%%%%%%%
12     abs_w=sqrt(w1.^2+w2.^2);
13     p1 = 2*alpha*abs_w+0.5*beta/esp;
14     p2 = 0.5*beta/esp;
15     p3 = 2*beta*esp;
16     % Do the central pixels
17     for i = 2:m-1
18         for j = 2:n-1
19             v(i,j) = (p2/p3+v(i,j+1)+v(i,j-1)+v(i+1,j)+v(i
                   -1,j))/((p1(i,j)+4*p3)/p3);
20         end
21     end
22     % Repeat the process for other 8 pixels around the
           central pixel
23     %%%%%%%%%% update u %%%%%%%%%%%%%%%%
24     diverg = Bx(w1-b1)+By(w2-b2);
```

```
25      % Compute divergence using backward derivative
26      % Bx: Backward derivative operator on x with boundary
            condition Bxu(:,1)=u(:,1)
27      %       function Bxu = Bx(u)
28      %       [~,n] = size(u);
29      %       Bxu = u - circshift(u,[0 1]);
30      %       Bxu(:,1) = u(:,1);
31      %       Bxu(:,n) = -u(:,n-1);
32      % By: Backward derivative operator on y with boundary
            condition Bxu(1,:)=u(1,:)
33      % Do the central pixels
34      for i = 2:m-1
35          for j = 2:n-1
36              u(i,j) = (InputImage(i,j)/theta+u(i,j+1)+u(i,j
                    -1)+u(i+1,j)+u(i-1,j)-diverg(i,j))/(4+1/
                    theta);
37          end
38      end
39      % Repeat the process for other 8 pixels around the
            central pixel
40      %%%%%%%%%% update w %%%%%%%%%%%%%%%%
41      ux=Fx(u);
42      % Fx: Forward derivative operator on x with boundary
            condition u(:,:,1)=u(:,:,1)
43      uy=Fy(u);
```

```
44      % Fy: Forward derivative operator on y with boundary
            condition u(1,:,:)=u(m,:,:)
45      c1=ux+b1;
46      c2=uy+b2;
47      abs_c=sqrt(c1.^2+c2.^2+eps);
48      w1=max(abs_c-v.^2.*alpha/theta,0).*c1./abs_c;
49      w2=max(abs_c-v.^2.*alpha/theta,0).*c2./abs_c;
50      %%%%% update Bregman iterative parameters %%%%%%%
51      b1=c1-w1;
52      b2=c2-w2;
53  end
54  OutputImage=u;
```

8.9 Fractal Feature Based Classification

```
1   for ImageNumber=1:HealthyImageFiles
2       InputImage=InputImage(:,:,2);
3       % Convert original colour image to grayscale image
4       FilterImageVessel=MultiscaleVesselnessFilter(
            InputImage);
5       FilterImageLine=LineFilter(FilterImageVessel);
6       % Apply MultiscaleVesselnessFilter followed by
            LineFilter to achieve
7       % the combinatory vessel filter framework
8       FilterImage=imfilter(FilterImageLine,fspecial('average
            ',ws),'replicate');
```

```
9       FilterImage=FilterImage-FilterImageLine-C;
10      SegmentedVessel=im2bw(FilterImage,0);
11      % Apply an adaptive thresholding algorithm that
            seperates the
12      % foreground from the background with nonuniform
            illumination.
13      % C = threshold mean, ws is the local window size.
14      SegmentedVessel=bwareaopen(SegmentedVessel,20);
15      % remove any object and noise those are smaller than
            20 pixels
16      SegmentedVessel=padarray(SegmentedVessel,[48 0],'both'
            );
17      % Pad empty pixel to the image to make it a square
            image
18      Q = [-10 -9 -8 -7 -6 -5 -4 -3 -2 -1 0 0.999 1.001 2 3
            4 5 6 7 8 9 10]
19      [a, f]=MultiFractalSpectrum(SegmentedVessel,Q);
20      % Produce multifractal features a and f using
            multifractal analysis
21      [FFD, FPS] = FourierPowerSpectrum(SegmentedVessel);
22      % Produce Fourier fractal features FFD and FPS using
            Fourier Power
23      % Spectrum analysis
24      HealthySet=[HealthySet;[a(Q==0) - a(end),a(1)-a(Q==0),
            f(Q==0),FFD,FPS(13:15)]];
```

```
25      % Store the extracted features into feature vector
26      % a(Q==0) - a(end), a(1)-a(Q==0) : the symmetry
            features
27      % f(Q==0): the peak of the multifractal spectrum
28      % FFD : Fourier fractal dimension
29      % FPS : Fourier power spectrum magnitude values at
            high frequencies
30  end
31
32  for ImageNumber=1:UnhealthyImageFiles
33      % ...
34      % Repeat the steps for unhealthy dataset
35      UnhealthySet=[UnhealthySet;[a(Q==0) - a(end),a(1)-a(Q
            ==0),f(Q==0),FFD,FPS(13:15)]];
36  end
37
38  % Once the features are stored in the vector, these can be
        used with many
39  % types of 2 classes supervised classifier, such as suppor
        vector machine
40  % For example:
41  % Classes = ones(20,1); % Create a vector to store classes
        information
42  % Classes(1:10) = -1;   % in this case, we name healthy
      patients 1 and -1
```

```
% for unhealthy sets
% TrainingSet=[HealthySet(1:10,:);UnhealthySet(1:10,:)];
% TestSet=[HealthySet(11:20,:);UnhealthySet(11:20,:)];
% Classifier  = svmtrain(TrainingSet, Classes);
% PredictedResults = svmclassify(Classifier, TestSet);
% TestResult= (Classes-PredictedResults)==0;
% Accuracy=sum(TestResult)/(10+10);
```

8.9.1 Multifractal Spectrum [32]

```
function [alpha,falpha] = MultiFractalSpectrum(InputImage,
    Q)
[boxsizes,boxmasses] = BoxCountingMethod(InputImage);
% There are many choices of box counting method, for
    example,
% the simpliest one is implemented as follows:
%
%       for all boxsizes
%          boxmasses(boxsizes) = 0
%          for all box positions
%             for all pixels inside the current box
%                if the pixels is part of the object
%                   boxmasses(boxsizes) = boxmasses(
    boxsizes) + 1
%                   stop searching pixels in the current
    box and move to
```

```
13 %                    the next box location
14 %                end
15 %            end
16 %        end
17 %    end
18 % A box of size boxsizes is placed over a point on the
       structure and
19 % the number of valid pixels contained within the box is
       counted, described as the boxmasses(boxsizes)
20
21 ImageMass = sum(InputImage(:));
22 % Number of pixels with intensity value of 1
23 AverageBoxMasses = zeros(size(Q,2),size(boxsizes,1));
24 for Qvalue = 1:size(Q,2)
25     for BoxSizeValue = 1:size(boxsizes,1)
26         masses = zeros(size(boxmasses,1),1);
27         for j = 1:size(boxmasses,1)
28             mass = boxmasses{j};
29             if size(mass,1) >= BoxSizeValue
30                 masses(j) = (mass(BoxSizeValue,1)./
                       ImageMass).^(Q(Qvalue)-1);
31             end
32         end
33         AverageBoxMasses(Qvalue,BoxSizeValue) = mean(
               masses);
```

```
34          % Store average box masses for each box size, each
                of the values Q
35      end
36  end
37  p = zeros(size(Q,2),2);
38  for Qvalue = 1:size(Q,2)
39      x_log = arrayfun(@log10,(sqrt(size(InputImage,1)*size(
            InputImage,2))).\boxsizes);
40      p(Qvalue,:) = polyfit(x_log,arrayfun(@log10,
            AverageBoxMasses(Qvalue,:)'),1);
41  end
42  tau = reshape(p(:,1),size(Q));
43  alpha = gradient(tau,Q);
44  falpha = alpha.*Q - tau;
45  % Values for f(alpha) are calculated using the Legendre
        transform of alpha(q)
46  end
```

8.9.2 Fourier Power Spectrum [182]

```
1  function [FFD,FPS] = FourierPowerSpectrum(InputImage)
2  [M, N] = size(InputImage);
3  ImageMean = mean(InputImage(:));
4  FourierImage = fftshift(fft2(double(InputImage) -
       ImageMean));
5  % Fourier transform of the original image
```

```
6  PowerMag = log(FourierImage .* conj(FourierImage)+ 10 ^
       (-6));
7  % Power spectrum magnitude
8  MagDirRad = zeros(NumDirection, NumRadius);
9  % MagDirRad stores magnitude for each direction and radius
10 NumMag = zeros(NumDirection, NumRadius);
11 % NumMag stores number MagDirRad
12 MagAllDir = zeros(2 * NumRadius,1);
13 % MagAllDir stores magnitude for all direction and radius
14 NumMagAllDir = zeros(2 * NumRadius,1);
15 % NumMagAllDir stores number of NumMagAllDir
16
17 % NumDirection: number of directions that the frequency
       space is uniformally divided
18 % NumRadius: number of points that the radius is
       uniformally divided
19 MaximumRadius = log(min(M,N)/2);
20 for j = 1:M
21     % Skip this loop if j is the center point in y
           coordinate
22     Yval = CenPntY - j;
23     for i = 1:N
24         % Skip this loop if i is the center point in x
               coordinate
25         XVal = i - CenPntX;
```

```
26          sqrtXY = log(sqrt(Yval * Yval + XVal * XVal));
27          if sqrtXY > 0 && sqrtXY <= MaximumRadius
28              MagValue = PowerMag(j,i);
29              theta = atan(Yval/XVal);
30              if XVal < 0 theta = theta + pi;  end
31              if theta < 0 theta = theta + 2 * pi; end
32              Angle = floor(NumDirection * theta /(2* pi));
33              if Angle > NumDirection - 1 || Angle < 0
34                  Angle = NumDirection - 1;
35              end
36              RadiusAll = floor(2*NumRadius * sqrtXY /
                    MaximumRadius);
37              RadiusEach = floor(RadiusAll/2);
38              if RadiusAll > 2 * NumRadius - 1
39                  RadiusEach = NumRadius - 1;    RadiusAll =
                        2 * NumRadius - 1;
40              end
41              if RadiusEach >= 5
42                  MagDirRad(Angle + 1, RadiusEach + 1) =
                        MagDirRad(Angle + 1, RadiusEach + 1) +
                        MagValue;
43                  NumMag(Angle + 1, RadiusEach + 1) = NumMag
                        (Angle + 1, RadiusEach + 1) + 1;
44              end
45              if RadiusAll >= 5
```

```
46                      MagAllDir(RadiusAll + 1) = MagAllDir(
                            RadiusAll + 1) + MagValue;
47                      NumMagAllDir(RadiusAll + 1) = NumMagAllDir
                            (RadiusAll + 1) + 1;
48                  end
49                  % This step accumulates magnitude for each
                        direction and radius
50              end
51          end
52  end
53
54  for AngleV = 1:NumDirection
55      for RadiusV = 6:NumRadius
56          FPSY = MagDirRad(AngleV, RadiusV)/NumMag(AngleV,
                    RadiusV);
57          % FPSY for each directions and scales
58      end
59  end
60  NumFPSY = 0;
61  for RadiusAll = 6:(2 * NumRadius)
62      NumFPSY = NumFPSY + 1;
63      FPSY(NumFPSY) = MagAllDir(RadiusAll) / NumMagAllDir(
            RadiusAll);
64      PlotX(NumFPSY) = (RadiusAll -1) * MaximumRadius / (2 *
            NumRadius);
```

```
65      % FPSY over all directions and scales
66  end
67  PowerSpectrum = polyfit(PlotX,FPSY,1);
68  FPS=FPSY;
69  FFD=(PowerSpectrum(1)+6)/2;
70  % Compute Fourier fractal dimension based on average slope
        of the power
71  % spectrum
```

Chapter 9

Appendix-Publications Preview

Three-Dimensional Vessel Segmentation Using A Novel Combinatory Filter Framework

Y. Ding[1*] W. O. C. Ward[1] T. Wästerlid[1]
P. A. Gowland[2] A. M. Peters[2] J. Yang[3] L. Bai[1]

[1]School of Computer Science, University of Nottingham, UK

[2]Sir Peter Mansfield Magnetic Resonance Centre, University of Nottingham, UK

[3]School of Electronics and Information, Shanghai Jiaotong University, China

Abstract

Blood vessel segmentation is of great importance in medical diagnostic applications. Filter based methods that make use of Hessian matrices have been found very useful for blood vessel segmentation in both 2D and 3D medical images. However, these methods often fail on images that contain high density microvessels and background noise. The errors in the form of missing, undesired broken or incorrectly merged vessels eventually lead to poor segmentation results. In this paper, we present a novel method for 3D vessel segmentation that is also suitable for segmenting microvessels, incorporating the advantages of a line filter and a Hessian-based vessel filter to overcome the problems. The proposed method is shown to be reliable for noisy and inhomogeneous images. Vessels can also be separated based on their scale/thickness so that the method can be used for different medical applications. Furthermore, a quantitative vessel analysis method based on the multifractal analysis is performed on the segmented vasculature, and fractal properties are found in all images.

1 Introduction

Vascular pathology is present in many human diseases and because of this there has been intense research in the past in vessel imaging for diagnosis and treatment of vascular diseases [1]. In recent years, the role of vascular dysfunction has been implicated in neurological diseases, including Alzheimer's Diseases (AD) [2, 3]. A significant finding is that vascular abnormalities could potentially serve as an early imaging biomarker of the diseases [4]. A sensible way to validate the theory linking the microvasculature to pathologies on large vascular datasets is to use automated computational methods [5]. However, the main weakness in vascular research is considered to

*Corresponding author – yzd@cs.nott.ac.uk

Retinal Vasculature Classification Using Novel Multifractal Features

Y. Ding[1] W. O. C. Ward[1] Jinming Duan[1]
D. P. Auer[2] Penny Gowland[3] L. Bai[1*]

[1]School of Computer Science, University of Nottingham, UK

[2]School of Medical Sciences, University of Nottingham, UK

[3]Sir Peter Mansfield Magnetic Resonance Centre, University of Nottingham, UK

Abstract

Retinal blood vessels have been implicated in a large number of diseases including diabetic retinopathy and cardiovascular diseases, which cause damages to retinal blood vessels. The availability of retinal vessel imaging provides an excellent opportunity for monitoring and diagnosis of retinal diseases, and automatic analysis of retinal vessels will help with the processes. However, state of the art vascular analysis methods such as counting the number of branches or measuring the curvature and diameter of individual vessels are unsuitable for the microvasculature. There has been published research using fractal analysis to calculate fractal dimensions of retinal blood vessels, but so far there has been no systematic research extracting discriminant features from retinal vessels for classifications. This paper introduces new methods for feature extraction from multifractal spectra of retinal vessels for classification. Two public available retinal vascular image databases are used for the experiments, and the proposed methods have produced better classification rates compared with existing methods.

1 Introduction

Vascular pathology is present in many human diseases and because of this there has been intense research in vascular image analysis for diagnosis and treatment of diseases [1, 2, 3, 4]. It has been suggested that vascular anomaly, especially the microvascular anomaly, could potentially serve as an early imaging biomarker of many diseases [5, 6].

A plausible way to analyse microvasculature and link the microvasculature to pathologies is to use computational methods. However, there is currently a lack of computational tools

*Email – bai@cs.nott.ac.uk

Novel Methods for Microglia Segmentation, Feature Extraction and Classification

Yuchun Ding[1], Marie Christine Pardon[2], Alessandra Agostini[2], Henryk Faas[2]
Jinming Duan[1], Wil O C Ward[1], Felicity Easton[2], Dorothee Auer[2], Li Bai[1]
[1]School of Computer Science, University of Nottingham, UK
[2]School of Medicine & Health Sciences, University of Nottingham, UK

***Abstract*—Microglial image segmentation and analysis would provide a valuable tool to gain insight into the biology and function of microglia in health and disease. Common image segmentation methods are not suitable for inhomogeneous histology images and accurate classification of the microglia has not yet been achieved. In this paper, an automated image analysis framework capable of accurately and efficiently segmenting the microglia from histology images and analysing their morphology is introduced. The framework includes the use of the fast split Bregman algorithm for image denoising and segmentation, and multifractal analysis for combinatory fractal feature extraction for support vector machine classification of microglial activation states. Experiments show that the proposed framework is accurate and scalable to large datasets and provides a useful tool for the study of microglial biology.**

***Index Terms*—microglia activation, fast split Bregman, multifractal analysis, support vector machine.**

I. Introduction

MICROGLIA are immune cells exclusive to the central nervous system (CNS) and about 1.5 trillion of them reside in the brain and spinal cord [1], [2]. Microglia present with multiple protective to detrimental phenotypes associated with motility and morphological changes, in response to variety of signals [3]. In the healthy brain, microglia constantly survey the surrounding tissue with extended processes, clear debris from dead cells, or prune and maintain brain synapses. They are also essential to learning and memory [4], [5] and protect neurons from damage and mediating pain [6], [7]. In response to an injury or infection, microglia initiate an early, protective response by moving towards the site of injury, where they release a cascade of chemicals leading to repair of the damaged area. Moreover, microglial activation is a hallmark of chronic neuroinflammation, which is believed to play an important, but incompletely understood, damaging role in a range of brain disorders, including stroke, multiple sclerosis, Parkinsons, Huntingtons and Alzheimer's disease [8], [9], [10], but can also reflect a neuroprotective behaviour in these chronic conditions [3].

The heterogeneity of microglia functions is in part linked to their shape and activation state, and much information can be obtained from their morphological characteristics [11]. Microglial cell shape evolves from resting fully ramified with extending tortuous processes and smaller soma, to the fully activated amoeboid shape with a larger soma and shorter or no processes by de-ramifying and re-ramifies upon deactivation [12], [13]. To date, microglia activation has been linked to three distinct functions: a classical pro-inflammatory activation state, an alternatively activated anti-inflammatory state and its overlapping and complementary acquired deactivation state associated with the anti-inflammatory and functional repair phenotype [3]. Classifying microglia activation states when analysing histological images can help pathologists with disease diagnosis [14], provides essential information for understanding diseases of the central nervous system and other detrimental or beneficial effects of microglial activation [15] and is essential to validating in vivo biomarkers [16] for more effective longitudinal monitoring of patients and populations at risk of diseases associated with neuroinflammation [17].

One of the major challenges in quantitative microglial analysis from immunohistological images is the development of automated microglial segmentation methods. Manual or semi-automated segmentation methods are time consuming and require user intervention [18], [19] with an element of subjectivity and inter-observer variability. Image analysis approaches commonly used for quantifying histology that rely on thresholding, such as ImageJ [20], struggle with inhomogenous immunohistochemistry images, where even staining over a single brain slice and across different slices from subsequent preparations can be challenging.

Another key challenge is the classification of distinct morphological states from resting-ramified to activated amoeboid, particularly the intermediate states, which is intimately linked to the multiple phenotypes of microglia [11]. Recent work has considered microglia as monofractals, and used a single fractal dimension value to describe the entire microglial structure [21], [11]. However, fractal dimension alone is not enough to discriminate microglia activation states as it only measures the dimension of the space that the data fills but not how the data fills the space. Fractal analysis methods have the potential to classify microglia morphology across the range of shapes from ramified and activated microglia, however, a systematic review has indicated that there is little research in classification of microglia activation states. [11], [21], [22].

In this paper, new methods are proposed for the quantitative analysis of microglial morphology. Cells are segmented using the Mumford-Shah Total Variation [23], [24], [25] and fast split Bregman [26] methods followed by multifractal analysis of the segmented structures. The proposed analysis method considers microglia as multifractals, and uses a multifractal spectrum to

Email – bai@cs.nott.ac.uk

Experimental Comparison of Vasculature Segmentation Methods

Yuchun Ding[1], Li Bai[1]
[1]*School of Computer Science, Nottingham University, Wollaton Road, Nottingham, UK*
{psxyd1, itzbl}@exmail.nottingham.ac.uk

Keywords: Vascular segmentation, retinal vasculature, Micro-CT.

Abstract: Vessel segmentation algorithms play a very important role in vascular disease diagnosis and prediction. Current vessel segmentation research uses mostly images of large vessels, which are relatively easy to extract, but segmenting microvasculature is more challenging and very important for analysing vascular disease such as Alzheimer's Diseases. The aim of this paper is to report experimental results of several common vessel image segmentation methods. Retinal vessel image database DRIVE is used for 2D experiments and a micro-CT image is used for 3D experiments.

1. INTRODUCTION

Vascular pathology is present in most human diseases, so there has been intense research in the past in Magnetic Resonance Imaging (MRI) for diagnosis and treatment of vascular diseases. Recently the role of neurovascular dysfunction has been identified, including Alzheimer's Diseases (AD). A significant finding is that vascular abnormalities and angiogenesis could potentially serve as an early biomarker of the diseases. But the lack of computational tools is becoming increasingly apparent. A feasible way to validate the theory linking microvasculature to pathology of neurodegenerative conditions on large datasets is to develop an automated computational analysis method. However, existing algorithms for image analysis have mostly been developed for segmenting large vessels, and analysis of these vessels has been limited to measuring curvature and diameter of individual vessels, which are unsuitable for microvasculature. Imaging devices such as micro-CT can achieve resolutions on the order of several μm, allowing imaging the three dimensional (3D) microvasculature down to the capillary level. The main weakness of using micro-CT for vascular research is considered to be the lack of software for 3D quantification of microvasculature. Four well-known segmentation methods were investigated, which include local entropy thresholding (LET), level set methods, vesselness filter, and wavelet transform modulus maxima (WTMM). All of these are well-performed on 2D retinal images and the aim of this paper is to review, analyse and compare the vessel segmentation methods in both 2D and 3D vessel images and to show the microvasculature detection performance of each method.

2. METHODS

2.1 Image Databases

We have chosen the retinal vessel image from a publicly available database DRIVE (Staal et al., 2004) for our 2D experiments because it is a commonly used database for previous research on vessel segmentation. The database is made up of 40 images that have been randomly selected from a diabetic retinopathy (DR)-screening program. Each image has a dimension of 565 by 584 pixels. For each image in the test set, two manual segmentations of blood vessels are available. The second set of manual segmented image will be used in this investigation because is it the observer results most commonly used when comparing effectiveness of method.

As the existing publicly available brain vasculature dataset such as MRI, CTA or MRA images only contain large vessels, which is not possible for analysing the microvasculature, a corrosion casting method was used to prepare 3-D

Bibliography

[1] Y. Ding, W. Ward, W. T, P. Gowland, A. Peters, J. Yang, and L. Bai, "Three-dimensional vessel segmentation using a novel combinatory filter framework," *Physics in Medicine and Biology*, 2014.

[2] Y. Ding, W. Ward, J. Duan, D. Auer, P. Gowland, and L. Bai, "Retinal vasculature classification using novel multifractal features," *Physics in Medicine and Biology*, 2015.

[3] M.-C. Pardon, M. Y. Lopez, D. Yuchun, M. Marjańska, M. Prior, C. Brignell, S. Parhizkar, A. Agostini, L. Bai, D. P. Auer, *et al.*, "Magnetic resonance spectroscopy discriminates the response to microglial stimulation of wild type and alzheimers disease models," *Scientific reports*, vol. 6, 2016.

[4] Y. Ding, H. Faas, M. C. Pardon, W. O. Ward, J. Duan, F. Easton, D. Auer, and L. Bai, "A novel framework for microglia extraction, morphological analysis and classification," *Transactions on Computational Biology and Bioinformatics*, Under Revision.

[5] Y. Ding and L. Bai, "Experimental comparison of vasculature segmentation methods," in *9th International Conference on Computer Vision Theory and Applications*, pp. 425–432, 2014.

[6] Y. Ding, W. O. C. Ward, T. Parker, S. Nakagawa, L. Buttery, L. White, and L. Bai, "Segmentation of mouse brain microvasculature from Micro-CT images using Gabor filter and local entropy thresholding," in *11th International Conference on Quantification of Brain Function with PET*, p. 136, 2013.

[7] W. O. Ward, Y. Ding, and L. Bai, "Analysis of three-dimensional vasculature using multifractal theory," in *Computational Intelligence in Healthcare and e-health (CICARE), 2014 IEEE Symposium on*, pp. 64–68, IEEE, 2014.

[8] J. Duan, Y. Ding, Z. Pan, J. Yang, and L. Bai, "Second order Mumford-Shah model for image denoising," in *International Conference on Image Processing*, 2015.

[9] A. Agostini, Y. Ding, L. Bai, and M. C. Pardon, "Unaltered susceptibility to neuroinflammation in pre-symptomatic appswe/ps1e9 mice, focus on genotype and sex differences," in *Meeting of the British Association for Psychopharmacology*, 2015.

[10] P. Scheltens, F. Barkhof, J. Valk, P. Algra, R. G. Van Der Hoop, J. Nauta, and E. C. Wolters, "White matter lesions on magnetic resonance imaging in clinically diagnosed Alzheimer's disease: evidence for heterogeneity," *Brain*, vol. 115, no. 3, pp. 735–748, 1992.

[11] V. T. Marchesi, "Alzheimer's dementia begins as a disease of small blood vessels, damaged by oxidative-induced inflammation and dysregulated amyloid metabolism: implications for early detection and therapy," *The FASEB Journal*, vol. 25, no. 1, pp. 5–13, 2011.

[12] T. Hashimura, T. Kimura, and T. Miyakawa, "Morphological changes of blood vessels in the brain with Alzheimer's disease," *Psychiatry and Clinical Neurosciences*, vol. 45, no. 3, pp. 661–665, 1991.

[13] W. Henneman, J. Sluimer, J. Barnes, W. Van Der Flier, I. Sluimer, N. Fox, P. Scheltens, H. Vrenken, and F. Barkhof, "Hippocampal atrophy rates in Alzheimer disease added value over whole brain volume measures," *Neurology*, vol. 72, no. 11, pp. 999–1007, 2009.

[14] D. J. Selkoe, "Resolving controversies on the path to Alzheimer's therapeutics," *Nature Medicine*, vol. 17, no. 9, pp. 1060–1065, 2011.

[15] D. Babin, A. Pižurica, J. De Vylder, E. Vansteenkiste, and W. Philips, "Brain blood vessel segmentation using line-shaped profiles," *Physics in Medicine and Biology*, vol. 58, no. 22, p. 8041, 2013.

[16] D. L. Wilson and J. A. Noble, "An adaptive segmentation algorithm for time-of-flight MRA data," *IEEE Transactions on Medical Imaging*, vol. 18, no. 10, pp. 938–945, 1999.

[17] T. Chanwimaluang and G. Fan, "An efficient blood vessel detection algorithm for retinal images using local entropy thresholding," in *Proceedings of International Symposium of the IEEE on Circuits and Systems*, vol. 5, pp. V–21, 2003.

[18] S. Mallat and S. Zhong, "Characterization of signals from multiscale edges," *IEEE Transactions on Pattern Analysis and Machine Intelligence*, vol. 14, no. 7, pp. 710–732, 1992.

[19] A. F. Frangi, W. J. Niessen, K. L. Vincken, and M. A. Viergever, "Multiscale vessel enhancement filtering," in *Medical Image Computing and Computer-Assisted Intervention*, pp. 130–137, Springer, 1998.

[20] P. T. Truc, M. A. Khan, Y.-K. Lee, S. Lee, and T.-S. Kim, "Vessel enhancement filter using directional filter bank," *Computer Vision and Image Understanding*, vol. 113, no. 1, pp. 101–112, 2009.

[21] P. Tomlins and S. Shah, "Clinical ophthalmology: a self-sssessment companion," *British Journal of Ophthalmology*, vol. 92, no. 3, pp. 441–441, 2008.

[22] L. G. Lundberg, R. Lerner, P. Sundelin, R. Rogers, J. Folkman, and J. Palmblad, "Bone marrow in polycythemia vera, chronic myelocytic leukemia, and myelofibrosis has an increased vascularity," *The American Journal of Pathology*, vol. 157, no. 1, pp. 15–19, 2000.

[23] A. J. Foss, R. A. Alexander, L. W. Jefferies, J. L. Hungerford, A. L. Harris, and S. Lightman, "Microvessel count predicts survival in uveal melanoma," *Cancer Research*, vol. 56, no. 13, pp. 2900–2903, 1996.

[24] E. P. Meyer, A. Ulmann-Schuler, M. Staufenbiel, and T. Krucker, "Altered morphology and 3d architecture of brain vasculature in a mouse model for alzheimer's disease," *Proceedings of the National Academy of Sciences*, vol. 105, no. 9, pp. 3587–3592, 2008.

[25] L. Risser, F. Plouraboué, A. Steyer, P. Cloetens, G. Le Duc, and C. Fonta, "From homogeneous to fractal normal and tumorous microvascular networks in the brain," *Journal of Cerebral Blood Flow & Metabolism*, vol. 27, no. 2, pp. 293–303, 2006.

[26] G. Liew, J. J. Wang, N. Cheung, Y. P. Zhang, W. Hsu, M. L. Lee, P. Mitchell, G. Tikellis, B. Taylor, and T. Y. Wong, "The retinal vasculature as a fractal: methodology, reliability, and relationship to blood pressure," *Ophthalmology*, vol. 115, no. 11, pp. 1951–1956, 2008.

[27] J. Grauslund, A. Green, R. Kawasaki, L. Hodgson, A. K. Sjølie, and T. Y. Wong, "Retinal vascular fractals and microvascular and macrovascular complications in type 1 diabetes," *Ophthalmology*, vol. 117, no. 7, pp. 1400–1405, 2010.

[28] T. Tél, Á. Fülöp, and T. Vicsek, "Determination of fractal dimensions for geometrical multifractals," *Physica A: Statistical Mechanics and its Applications*, vol. 159, no. 2, pp. 155–166, 1989.

[29] H. Stanley, L. N. Amaral, A. Goldberger, S. Havlin, P. C. Ivanov, and C.-K. Peng, "Statistical physics and physiology: monofractal and multifractal approaches," *Physica A: Statistical Mechanics and its Applications*, vol. 270, no. 1, pp. 309–324, 1999.

[30] G. A. Losa, *Fractals in Biology and Medicine*. Wiley Online Library, 2005.

[31] T. Stosic and B. D. Stosic, "Multifractal analysis of human retinal vessels," *IEEE Transactions on Medical Imaging*, vol. 25, no. 8, pp. 1101–1107, 2006.

[32] W. O. C. Ward and L. Bai, "Multifractal analysis of microvasculature in health and disease," in *35th Annual International Conference of the IEEE on Engineering in Medicine and Biology Society*, pp. 2336–2339, 2013.

[33] L. Lawson, V. Perry, and S. Gordon, "Turnover of resident microglia in the normal adult mouse brain," *Neuroscience*, vol. 48, no. 2, pp. 405–415, 1992.

[34] A. J. Dowding, A. Maggs, and J. Scholes, "Diversity amongst the microglia in growing and regenerating fish cns: Immunohistochemical characterization using fl. 1, an anti-macrophage monoclonal antibody," *Glia*, vol. 4, no. 4, pp. 345–364, 1991.

[35] D. Checchin, F. Sennlaub, E. Levavasseur, M. Leduc, and S. Chemtob, "Potential role of microglia in retinal blood vessel formation.," *Investigative ophthalmology & visual science*, vol. 47, no. 8, pp. 3595–3602, 2006.

[36] X.-G. Luo and S.-D. Chen, "The changing phenotype of microglia from homeostasis to disease," *Transl Neurodegener*, vol. 1, no. 9, 2012.

[37] B. Faith, "Microglia: A standing ovation, please!," *Brain Sense*, 2011.

[38] L. R. Frick, K. Williams, and C. Pittenger, "Microglial dysregulation in psychiatric disease," *Journal of Immunology Research*, vol. 2013, 2013.

[39] J. Vinet, H. Weering, A. Heinrich, R. E. Kälin, A. Wegner, N. Brouwer, F. L. Heppner, N. v. Rooijen, H. Boddeke, and K. Biber, "Neuroprotective function for ramified microglia in hippocampal excitotoxicity," *J Neuroinflammation*, vol. 9, no. 1, p. 27, 2012.

[40] L. R. Watkins, E. D. Milligan, and S. F. Maier, "Glial activation: a driving force for pathological pain," *Trends in neurosciences*, vol. 24, no. 8, pp. 450–455, 2001.

[41] P. Kapeller, S. Ropele, C. Enzinger, T. Lahousen, S. Strasser-Fuchs, R. Schmidt, and F. Fazekas, "Discrimination of white matter lesions and multiple sclerosis plaques by short echo quantitative 1hmagnetic resonance spectroscopy," *Journal of neurology*, vol. 252, no. 10, pp. 1229–1234, 2005.

[42] D. Zádori, G. Nyiri, A. Szőnyi, I. Szatmári, F. Fülöp, J. Toldi, T. F. Freund, L. Vécsei, and P. Klivényi, "Neuroprotective effects of a novel kynurenic acid analogue in a transgenic mouse model of huntingtons disease," *Journal of neural transmission*, vol. 118, no. 6, pp. 865–875, 2011.

[43] H. Akiyama, S. Barger, S. Barnum, B. Bradt, J. Bauer, G. M. Cole, N. R. Cooper, P. Eikelenboom, M. Emmerling, B. L. Fiebich, *et al.*, "Inflammation and alzheimers disease," *Neurobiology of aging*, vol. 21, no. 3, pp. 383–421, 2000.

[44] A. Karperien, H. Ahammer, and H. F. Jelinek, "Quantitating the subtleties of microglial morphology with fractal analysis," *Frontiers in cellular neuroscience*, vol. 7, 2013.

[45] J. S. Henkel, D. R. Beers, W. Zhao, and S. H. Appel, "Microglia in als: the good, the bad, and the resting," *Journal of Neuroimmune Pharmacology*, vol. 4, no. 4, pp. 389–398, 2009.

[46] G. Kreutzberg, "Microglia, the first line of defence in brain pathologies.," *Arzneimittel-Forschung*, vol. 45, no. 3A, pp. 357–360, 1995.

[47] A. Karperien, H. Ahammer, and H. F. Jelinek, "Quantitating the subtleties of microglial morphology with fractal analysis," *Never-resting microglia: physiological roles in the healthy brain and pathological implications*, 2015.

[48] W. J. Streit, "Microglial response to brain injury: a brief synopsis," *Toxicologic pathology*, vol. 28, no. 1, pp. 28–30, 2000.

[49] N. A. Valous, B. Lahrmann, W. Zhou, R. Veltkamp, and N. Grabe, "Multistage histopathological image segmentation of iba1-stained murine

microglias in a focal ischemia model: Methodological workflow and expert validation," *Journal of neuroscience methods*, vol. 213, no. 2, pp. 250–262, 2013.

[50] L. A. Cysique, K. Moffat, D. M. Moore, T. A. Lane, N. W. Davies, A. Carr, B. J. Brew, and C. Rae, "Hiv, vascular and aging injuries in the brain of clinically stable hiv-infected adults: a 1h mrs study," *PloS one*, vol. 8, no. 4, p. e61738, 2013.

[51] H. Jelinek, A. Karperien, A. Buchan, and T. Bossomaier, "Differentiating grades of microglia activation with fractal analysis," *Complexity International*, vol. 12, 2008.

[52] D. J. Donnelly, J. C. Gensel, D. P. Ankeny, N. van Rooijen, and P. G. Popovich, "An efficient and reproducible method for quantifying macrophages in different experimental models of central nervous system pathology," *Journal of neuroscience methods*, vol. 181, no. 1, pp. 36–44, 2009.

[53] C. A. Schneider, W. S. Rasband, and K. W. Eliceiri, "Nih image to imagej: 25 years of image analysis," *Nature methods*, vol. 9, no. 7, pp. 671–675, 2012.

[54] C. Kozlowski and R. M. Weimer, "An automated method to quantify microglia morphology and application to monitor activation state longitudinally in vivo," *PloS one*, vol. 7, no. 2, p. e31814, 2012.

[55] I. B. Hovens, C. Nyakas, R. G. Schoemaker, *et al.*, "A novel method for evaluating microglial activation using ionized calcium-binding adaptor protein-1 staining: cell body to cell size ratio," *Neuroimmunology and Neuroinflammation*, vol. 1, no. 2, p. 82, 2014.

[56] D. Mumford and J. Shah, "Optimal approximations by piecewise smooth functions and associated variational problems," *Communications on pure and applied mathematics*, vol. 42, no. 5, pp. 577–685, 1989.

[57] L. I. Rudin, S. Osher, and E. Fatemi, "Nonlinear total variation based noise removal algorithms," *Physica D: Nonlinear Phenomena*, vol. 60, no. 1, pp. 259–268, 1992.

[58] T. Goldstein and S. Osher, "The split bregman method for l1-regularized problems," *SIAM Journal on Imaging Sciences*, vol. 2, no. 2, pp. 323–343, 2009.

[59] Y. Yang, S. Huang, and N. Rao, "An automatic hybrid method for retinal blood vessel extraction," *International Journal of Applied Mathematics and Computer Science*, vol. 18, no. 3, pp. 399–407, 2008.

[60] N. Otsu, "A threshold selection method from gray-level histograms," *Automatica*, vol. 11, no. 285-296, pp. 23–27, 1975.

[61] Q. Li, J. You, L. Zhang, and P. Bhattacharya, "Automated retinal vessel segmentation using multiscale analysis and adaptive thresholding," in *Image Analysis and Interpretation, 2006 IEEE Southwest Symposium on*, pp. 139–143, IEEE, 2006.

[62] X. Jiang and D. Mojon, "Adaptive local thresholding by verification-based multithreshold probing with application to vessel detection in retinal images," *Pattern Analysis and Machine Intelligence, IEEE Transactions on*, vol. 25, no. 1, pp. 131–137, 2003.

[63] N. P. Singh, R. Kumar, and R. Srivastava, "Local entropy thresholding based fast retinal vessels segmentation by modifying matched filter," in *Computing, Communication & Automation (ICCCA), 2015 International Conference on*, pp. 1166–1170, IEEE, 2015.

[64] J. Kaur and H. Sinha, "An efficient blood vessel detection algorithm for retinal images using local entropy thresholding," in *International Journal of Engineering Research and Technology*, vol. 1, ESRSA Publications, 2012.

[65] Y. Cheng *et al.*, "Automatic extraction of retinal blood vessel based on matched filtering and local entropy thresholding," in *2015 8th International Conference on Biomedical Engineering and Informatics (BMEI)*, pp. 62–67, IEEE, 2015.

[66] S. K. Kuri, S. S. Patankar, and J. V. Kulkarni, "Optimized mfr & automated local entropy thresholding for retinal blood vessel extraction," in *Electrical & Computer Engineering (ICECE), 2012 7th International Conference on*, pp. 141–144, IEEE, 2012.

[67] N. R. Pal and S. K. Pal, "Entropic thresholding," *Signal processing*, vol. 16, no. 2, pp. 97–108, 1989.

[68] T. Pun, "A new method for grey-level picture thresholding using the entropy of the histogram," *Signal processing*, vol. 2, no. 3, pp. 223–237, 1980.

[69] T. Pun, "Entropic thresholding, a new approach," *Computer Graphics and Image Processing*, vol. 16, no. 3, pp. 210–239, 1981.

[70] X. Zhang and G. Fan, "Retinal spot lesion detection using adaptive multiscale morphological processing," in *Advances in Visual Computing*, pp. 490–501, Springer, 2006.

[71] Y. Sato, S. Nakajima, H. Atsumi, T. Koller, G. Gerig, S. Yoshida, and R. Kikinis, "3d multi-scale line filter for segmentation and visualization of curvilinear structures in medical images," in *CVRMed-MRCAS'97*, pp. 213–222, Springer, 1997.

[72] C. Lorenz, I.-C. Carlsen, T. M. Buzug, C. Fassnacht, and J. Weese, "Multi-scale line segmentation with automatic estimation of width, contrast and tangential direction in 2d and 3d medical images," in *CVRMed-MRCAS'97*, pp. 233–242, Springer, 1997.

[73] K. Poon, G. Hamarneh, and R. Abugharbieh, "Live-vessel: Extending livewire for simultaneous extraction of optimal medial and boundary paths in vascular images," in *Medical Image Computing and Computer-Assisted Intervention–MICCAI 2007*, pp. 444–451, Springer, 2007.

[74] K. Krissian, G. Malandain, N. Ayache, R. Vaillant, and Y. Trousset, "Model-based detection of tubular structures in 3d images," *Computer vision and image understanding*, vol. 80, no. 2, pp. 130–171, 2000.

[75] S. D. Olabarriaga, M. Breeuwer, and W. Niessen, "Evaluation of hessian-based filters to enhance the axis of coronary arteries in ct images," in *International Congress Series*, vol. 1256, pp. 1191–1196, Elsevier, 2003.

[76] O. Wink, W. J. Niessen, and M. A. Viergever, "Multiscale vessel tracking," *Medical Imaging, IEEE Transactions on*, vol. 23, no. 1, pp. 130–133, 2004.

[77] A. Enquobahrie, L. Ibanez, E. Bullitt, and S. Aylward, "Vessel enhancing diffusion filter," *The Insight Journal*, vol. 1, pp. 1–14, 2007.

[78] S. I. De Zanet, C. Ciller, P. Maeder, F. L. Munier, and J. H. Kowal, "Fusion of fundus images and mri data of the human eye," *Investigative Ophthalmology & Visual Science*, vol. 55, no. 13, pp. 5846–5846, 2014.

[79] R. Srivastava, D. W. Wong, L. Duan, J. Liu, and T. Y. Wong, "Red lesion detection in retinal fundus images using frangi-based filters," in *Engineering in Medicine and Biology Society (EMBC), 2015 37th Annual International Conference of the IEEE*, pp. 5663–5666, IEEE, 2015.

[80] I. C. Campbell, B. Coudrillier, J. Mensah, R. L. Abel, and C. R. Ethier, "Automated segmentation of the lamina cribrosa using frangi's filter: a novel approach for rapid identification of tissue volume fraction and beam orientation in a trabeculated structure in the eye," *Journal of The Royal Society Interface*, vol. 12, no. 104, p. 20141009, 2015.

[81] P. Perona and J. Malik, "Scale-space and edge detection using anisotropic diffusion," *Pattern Analysis and Machine Intelligence, IEEE Transactions on*, vol. 12, no. 7, pp. 629–639, 1990.

[82] R. P. Kumar, F. Albregtsen, M. Reimers, B. Edwin, T. Langø, and O. J. Elle, "Three-dimensional blood vessel segmentation and centerline extraction based on two-dimensional cross-section analysis," *Annals of biomedical engineering*, vol. 43, no. 5, pp. 1223–1234, 2015.

[83] W. He, Y. Cao, Y. Li, Y. Miao, W. Shi, F. He, F. Yan, Z. Jiang, and H. Zhang, "A study on ct aorta segmentation using vessel enhancement

diffusion filter and region growing," in *Natural Computation (ICNC), 2015 11th International Conference on*, pp. 939–943, IEEE, 2015.

[84] R. Manniesing, M. A. Viergever, and W. J. Niessen, "Vessel enhancing diffusion: A scale space representation of vessel structures," *Medical Image Analysis*, vol. 10, no. 6, pp. 815–825, 2006.

[85] T. El-Arwadi and A. El-Zaart, "A novel 5x5 edge detection operator for blood vessel images," *British Journal of Applied Science & Technology, accepted August*, 2015.

[86] S. Sarangi, A. Mohapatra, and S. K. Sabut, "A comparative evaluation of diabetic retinal vascular structures using edge detection techniques," *International Journal of Telemedicine and Clinical Practices*, vol. 1, no. 1, pp. 111–120, 2015.

[87] M. Saha, M. K. Naskar, and B. Chatterji, "Detection of diabetic retinopathy using the wavelet transform and feedforward neural network," in *Advanced Computing and Systems for Security*, pp. 101–109, Springer, 2016.

[88] R. C. Gonzalez, R. E. Woods, and S. L. Eddins, *Digital image processing using MATLAB*. Pearson Education India, 2004.

[89] A. Chakraborty, L. H. Staib, and J. S. Duncan, "Deformable boundary finding in medical images by integrating gradient and region information," *Medical Imaging, IEEE Transactions on*, vol. 15, no. 6, pp. 859–870, 1996.

[90] S. Mallat, *A wavelet tour of signal processing*. Academic press, 1999.

[91] H. Tiankai and H. Shengzhong, "Based on wavelet transformation mold maximum value edge examination research," in *Proceedings of the 2012*

International Conference on Communication, Electronics and Automation Engineering, pp. 619–626, Springer, 2013.

[92] Z. He and A. C. Chung, "3-d b-spline wavelet-based local standard deviation (bwlsd): Its application to edge detection and vascular segmentation in magnetic resonance angiography," *International journal of computer vision*, vol. 87, no. 3, pp. 235–265, 2010.

[93] M. M. Fraz, P. Remagnino, A. Hoppe, B. Uyyanonvara, A. R. Rudnicka, C. G. Owen, and S. A. Barman, "Blood vessel segmentation methodologies in retinal images–a survey," *Computer methods and programs in biomedicine*, vol. 108, no. 1, pp. 407–433, 2012.

[94] T. Wozniak and M. Strzelecki, "Segmentation of 3d magnetic resonance brain vessel images based on level set approaches," in *Signal Processing: Algorithms, Architectures, Arrangements, and Applications (SPA), 2015*, pp. 56–61, IEEE, 2015.

[95] H. Min, W. Jia, X.-F. Wang, Y. Zhao, R.-X. Hu, Y.-T. Luo, F. Xue, and J.-T. Lu, "An intensity-texture model based level set method for image segmentation," *Pattern Recognition*, vol. 48, no. 4, pp. 1543–1558, 2015.

[96] Z. Guo, P. Lin, G. Ji, and Y. Wang, "Retinal vessel segmentation using a finite element based binary level set method," *Inverse Problems and Imaging*, vol. 8, no. 2, pp. 459–473, 2014.

[97] R. Malladi, J. A. Sethian, and B. C. Vemuri, "Shape modeling with front propagation: A level set approach," *Pattern Analysis and Machine Intelligence, IEEE Transactions on*, vol. 17, no. 2, pp. 158–175, 1995.

[98] D. Adalsteinsson and J. Sethian, "A level set approach to a unified model for etching, deposition, and lithography i: algorithms and two-dimensional simulations," *Journal of Computational Physics*, vol. 120, no. 1, pp. 128–144, 1995.

[99] K. Siddiqi, Y. B. Lauziere, A. Tannenbaum, and S. W. Zucker, "Area and length minimizing flows for shape segmentation," *Image Processing, IEEE Transactions on*, vol. 7, no. 3, pp. 433–443, 1998.

[100] J. S. Suri, D. Wu, J. Gao, S. Singh, and S. Laxminarayan, "A comparison of state-of-the-art diffusion imaging techniques for smoothing medical/non-medical image data," in *Pattern Recognition, 2002. Proceedings. 16th International Conference on*, vol. 1, pp. 508–511, IEEE, 2002.

[101] G. Lathen, J. Jonasson, and M. Borga, "Phase based level set segmentation of blood vessels," in *19th International Conference of the IEEE on Pattern Recognition*, pp. 1–4, 2008.

[102] G. Läthén, J. Jonasson, and M. Borga, "Blood vessel segmentation using multi-scale quadrature filtering," *Pattern Recognition Letters*, vol. 31, no. 8, pp. 762–767, 2010.

[103] Y. Zhao, Y. Liu, X. Wu, S. P. Harding, and Y. Zheng, "Retinal vessel segmentation: An efficient graph cut approach with retinex and local phase," *PloS one*, vol. 10, no. 4, p. e0122332, 2015.

[104] G. H. Granlund and H. Knutsson, *Signal processing for computer vision*, vol. 2. Springer, 1995.

[105] W. C. Wong and A. C. Chung, "Bayesian image segmentation using local iso-intensity structural orientation," *Image Processing, IEEE Transactions on*, vol. 14, no. 10, pp. 1512–1523, 2005.

[106] S. Osher and J. A. Sethian, "Fronts propagating with curvature-dependent speed: algorithms based on hamilton-jacobi formulations," *Journal of computational physics*, vol. 79, no. 1, pp. 12–49, 1988.

[107] V. Caselles, F. Catté, T. Coll, and F. Dibos, "A geometric model for active contours in image processing," *Numerische mathematik*, vol. 66, no. 1, pp. 1–31, 1993.

[108] L. Xu and S. Luo, "A novel method for blood vessel detection from retinal images," *Biomedical engineering online*, vol. 9, no. 1, p. 14, 2010.

[109] E. Ricci and R. Perfetti, "Retinal blood vessel segmentation using line operators and support vector classification," *IEEE Transactions on Medical Imaging*, vol. 26, no. 10, pp. 1357–1365, 2007.

[110] L. Shen, L. Bai, and M. Fairhurst, "Gabor wavelets and general discriminant analysis for face identification and verification," *Image and Vision Computing*, vol. 25, no. 5, pp. 553–563, 2007.

[111] S. Tălu, C. Vlăduţiu, and C. A. Lupaşcu, "Characterization of human retinal vessel arborisation in normal and amblyopic eyes using multifractal analysis," *International journal of ophthalmology*, vol. 8, no. 5, p. 996, 2015.

[112] B. B. Mandelbrot, *The fractal geometry of nature*. 1982.

[113] A. Arneodo, B. Audit, N. Decoster, J.-F. Muzy, and V. C, *The Science of Disasters - Wavelet based multifractal formalism: Applications to DNA*

sequences, satellite images of the cloud structure and stock market data. Springer, 2002.

[114] A. Arneodo, E. Bacryb, and J. F. Muzya, *The thermodynamics of fractals revisted with wavelets.* Cambridge University Press, 2004.

[115] C. Los, *Financial market risk: measurement and analysis.* Routledge, 2006.

[116] C. A. Los and B. Yu, "Persistence characteristics of the chinese stock markets," *International Review of Financial Analysis*, vol. 17, no. 1, pp. 64–82, 2008.

[117] M. Barni, *Document and image compression.* CRC press, 2006.

[118] T. Q. Nguyen, "A tutorial on filter banks and wavelets1," 1995.

[119] J. A. Suykens and J. Vandewalle, "Least squares support vector machine classifiers," *Neural processing letters*, vol. 9, no. 3, pp. 293–300, 1999.

[120] G. Strang and T. Nguyen, *Wavelets and filter banks.* SIAM, 1996.

[121] H. V. Nguyen and L. Bai, "Cosine similarity metric learning for face verification," in *Computer Vision*, pp. 709–720, Springer, 2011.

[122] T. S. Furey, N. Cristianini, N. Duffy, D. W. Bednarski, M. Schummer, and D. Haussler, "Support vector machine classification and validation of cancer tissue samples using microarray expression data," *Bioinformatics*, vol. 16, no. 10, pp. 906–914, 2000.

[123] R. Rollins, A. H. Marshall, E. McLoone, and S. Chamney, "Discrete conditional phase-type model utilising a multiclass support vector machine for the

prediction of retinopathy of prematurity," in *Computer-Based Medical Systems (CBMS), 2015 IEEE 28th International Symposium on*, pp. 250–255, IEEE, 2015.

[124] V. Vapnik, "Pattern recognition using generalized portrait method," *Automation and remote control*, vol. 24, pp. 774–780, 1963.

[125] B. E. Boser, I. M. Guyon, and V. N. Vapnik, "A training algorithm for optimal margin classifiers," in *Proceedings of the fifth annual workshop on Computational learning theory*, pp. 144–152, ACM, 1992.

[126] U. T. Nguyen, A. Bhuiyan, L. A. Park, and K. Ramamohanarao, "An effective retinal blood vessel segmentation method using multi-scale line detection," *Pattern Recognition*, 2012.

[127] Z. Sołtys, M. Ziaja, R. Pawliński, Z. Setkowicz, and K. Janeczko, "Morphology of reactive microglia in the injured cerebral cortex. fractal analysis and complementary quantitative methods," *Journal of neuroscience research*, vol. 63, no. 1, pp. 90–97, 2001.

[128] T. Wyss-Coray and J. Rogers, "Inflammation in alzheimer diseasea brief review of the basic science and clinical literature," *Cold Spring Harbor perspectives in medicine*, vol. 2, no. 1, p. a006346, 2012.

[129] J. Duan, Z. Pan, B. Zhang, W. Liu, and X.-C. Tai, "Fast algorithm for color texture image inpainting using the non-local ctv model," *Journal of Global Optimization*, pp. 1–24, 2015.

[130] J. Shah, "A common framework for curve evolution, segmentation and anisotropic diffusion," in *Computer Vision and Pattern Recognition*, pp. 136–142, IEEE, 1996.

[131] J. C. Russ, *Fractal surfaces*. Springer, 1994.

[132] T. Melmer, S. A. Amirshahi, M. Koch, J. Denzler, and C. Redies, "From regular text to artistic writing and artworks: Fourier statistics of images with low and high aesthetic appeal," *Frontiers in human neuroscience*, vol. 7, 2013.

[133] E. Haacke, S. Mittal, Z. Wu, J. Neelavalli, and Y.-C. Cheng, "Susceptibility-weighted imaging: technical aspects and clinical applications, part 1," *American Journal of Neuroradiology*, vol. 30, no. 1, pp. 19–30, 2009.

[134] J. Schindelin, I. Arganda-Carreras, E. Frise, V. Kaynig, M. Longair, T. Pietzsch, S. Preibisch, C. Rueden, S. Saalfeld, B. Schmid, *et al.*, "Fiji: an open-source platform for biological-image analysis," *Nature Methods*, vol. 9, no. 7, pp. 676–682, 2012.

[135] J. G. Sled, A. P. Zijdenbos, and A. C. Evans, "A nonparametric method for automatic correction of intensity nonuniformity in MRI data," *IEEE Transactions on Medical Imaging*, vol. 17, no. 1, pp. 87–97, 1998.

[136] D. J. Gould, T. J. Vadakkan, R. A. Poché, and M. E. Dickinson, "Multifractal and lacunarity analysis of microvascular morphology and remodeling," *Microcirculation*, vol. 18, no. 2, pp. 136–151, 2011.

[137] J. Staal, M. D. Abràmoff, M. Niemeijer, M. A. Viergever, and B. van Ginneken, "Ridge-based vessel segmentation in color images of the retina," *IEEE Transactions on Medical Imaging*, vol. 23, no. 4, pp. 501–509, 2004.

[138] A. Hoover, V. Kouznetsova, and M. Goldbaum, "Locating blood vessels in retinal images by piecewise threshold probing of a matched filter response," *IEEE Transactions on Medical Imaging*, vol. 19, no. 3, pp. 203–210, 2000.

[139] T. Kauppi, V. Kalesnykiene, J.-K. Kamarainen, L. Lensu, I. Sorri, A. Raninen, R. Voutilainen, H. Uusitalo, H. Kälviäinen, and J. Pietilä, "The diaretdb1 diabetic retinopathy database and evaluation protocol.," in *BMVC*, pp. 1–10, 2007.

[140] R. Pajak, "Use of two-dimensional matched filters for estimating a length of blood vessels newly created in angiogenesis process," *Opto-Electronics Review*, vol. 11, no. 3, pp. 237–241, 2003.

[141] J. V. Soares, J. J. Leandro, R. M. Cesar, H. F. Jelinek, and M. J. Cree, "Retinal vessel segmentation using the 2-D Gabor wavelet and supervised classification," *IEEE Transactions on Medical Imaging*, vol. 25, no. 9, pp. 1214–1222, 2006.

[142] D. Gabor, "Theory of communication. part 1: The analysis of information," *Electrical Engineers-Part III: Radio and Communication Engineering, Journal of the Institution of*, vol. 93, no. 26, pp. 429–441, 1946.

[143] J. G. Daugman, "Uncertainty relation for resolution in space, spatial frequency, and orientation optimized by two-dimensional visual cortical filters," *JOSA A*, vol. 2, no. 7, pp. 1160–1169, 1985.

[144] P. Siddalingaswamy and K. G. Prabhu, "Automatic detection of multiple oriented blood vessels in retinal images," *Journal of Biomedical Science and Engineering*, vol. 3, no. 01, p. 101, 2010.

[145] D. Zhang and M. Sonka, *Medical Biometrics: Second International Conference, ICMB 2010, Hong Kong, China, June 28-30, 2010. Proceedings*, vol. 6165. Springer Science & Business Media, 2010.

[146] Q. Li, J. You, L. Zhang, D. Zhang, and P. Bhattacharya, "A new approach to automated retinal vessel segmentation using multiscale analysis," in *Pattern Recognition, 2006. ICPR 2006. 18th International Conference on*, vol. 4, pp. 77–80, IEEE, 2006.

[147] D. Wu, M. Zhang, J.-C. Liu, and W. Bauman, "On the adaptive detection of blood vessels in retinal images," *Biomedical Engineering, IEEE Transactions on*, vol. 53, no. 2, pp. 341–343, 2006.

[148] F. M. Villalobos-Castaldi, E. M. Felipe-Riverón, and L. P. Sánchez-Fernández, "A fast, efficient and automated method to extract vessels from fundus images," *Journal of Visualization*, vol. 13, no. 3, pp. 263–270, 2010.

[149] D. A. Clausi and M. E. Jernigan, "Designing gabor filters for optimal texture separability," *Pattern Recognition*, vol. 33, no. 11, pp. 1835–1849, 2000.

[150] Z.-Q. Liu, J.-H. Cai, and R. Buse, *Handwriting recognition: soft computing and probabilistic approaches*, vol. 133. Springer Science & Business Media, 2003.

[151] M. Al-Rawi, M. Qutaishat, and M. Arrar, "An improved matched filter for blood vessel detection of digital retinal images," *Computers in Biology and Medicine*, vol. 37, no. 2, pp. 262–267, 2007.

[152] J. H. Holland, *Adaptation in natural and artificial systems: An introductory analysis with applications to biology, control, and artificial intelligence*. U Michigan Press, 1975.

[153] A. Chipperfield and P. Fleming, "The matlab genetic algorithm toolbox," in *IEEE Colloquium on Applied Control Techniques Using MATLAB*, pp. 10–1, IET, 1995.

[154] A. Chipperfield, P. Fleming, and C. Fonseca, "Genetic algorithm tools for control systems engineering," in *Proceedings of Adaptive Computing in Engineering Design and Control*, pp. 128–133, Citeseer, 1994.

[155] S. Mallat, *A wavelet tour of signal processing: the sparse way*. Academic press, 2008.

[156] G. Turin, "An introduction to matched filters," *IRE transactions on Information theory*, vol. 3, no. 6, pp. 311–329, 1960.

[157] S. Chaudhuri, S. Chatterjee, N. Katz, M. Nelson, and M. Goldbaum, "Detection of blood vessels in retinal images using two-dimensional matched filters," *IEEE Transactions on medical imaging*, vol. 8, no. 3, pp. 263–269, 1989.

[158] D. Marín, A. Aquino, M. E. Gegúndez-Arias, and J. M. Bravo, "A new supervised method for blood vessel segmentation in retinal images by using

gray-level and moment invariants-based features," *Medical Imaging, IEEE Transactions on*, vol. 30, no. 1, pp. 146–158, 2011.

[159] B. Zhang, L. Zhang, L. Zhang, and F. Karray, "Retinal vessel extraction by matched filter with first-order derivative of gaussian," *Computers in biology and medicine*, vol. 40, no. 4, pp. 438–445, 2010.

[160] M. S. Miri and A. Mahloojifar, "Retinal image analysis using curvelet transform and multistructure elements morphology by reconstruction," *Biomedical Engineering, IEEE Transactions on*, vol. 58, no. 5, pp. 1183–1192, 2011.

[161] M. Vlachos and E. Dermatas, "Multi-scale retinal vessel segmentation using line tracking," *Computerized Medical Imaging and Graphics*, vol. 34, no. 3, pp. 213–227, 2010.

[162] L. Espona, M. J. Carreira, M. Penedo, and M. Ortega, "Retinal vessel tree segmentation using a deformable contour model," in *Pattern Recognition, 2008. ICPR 2008. 19th International Conference on*, pp. 1–4, IEEE, 2008.

[163] P. Bankhead, C. N. Scholfield, J. G. McGeown, and T. M. Curtis, "Fast retinal vessel detection and measurement using wavelets and edge location refinement," *PloS one*, vol. 7, no. 3, p. e32435, 2012.

[164] E. P. Meyer, A. Ulmann-Schuler, M. Staufenbiel, and T. Krucker, "Altered morphology and 3D architecture of brain vasculature in a mouse model for alzheimer's disease," *Proceedings of the National Academy of Sciences*, vol. 105, no. 9, pp. 3587–3592, 2008.

[165] T. T. Nguyen and T. Y. Wong, "Retinal vascular changes and diabetic retinopathy," *Current diabetes reports*, vol. 9, no. 4, pp. 277–283, 2009.

[166] M. J. van Grinsven, Y. T. Lechanteur, J. P. van de Ven, B. van Ginneken, C. B. Hoyng, T. Theelen, and C. I. Sánchez, "Automatic drusen quantification and risk assessment of age-related macular degeneration on color fundus imagesautomatic drusen quantification on color fundus images," *Investigative ophthalmology & visual science*, vol. 54, no. 4, pp. 3019–3027, 2013.

[167] P. Parsons-Wingerter, K. Radhakrishnan, M. B. Vickerman, and P. K. Kaiser, "Oscillation of angiogenesis with vascular dropout in diabetic retinopathy by vessel generation analysis (vesgen)," *Investigative ophthalmology & visual science*, vol. 51, no. 1, pp. 498–507, 2010.

[168] W. L. Yun, U. R. Acharya, Y. Venkatesh, C. Chee, L. C. Min, and E. Ng, "Identification of different stages of diabetic retinopathy using retinal optical images," *Information Sciences*, vol. 178, no. 1, pp. 106–121, 2008.

[169] Y. Ding, W. Ward, W. T, P. Gowland, A. Peters, J. Yang, and L. Bai, "Three-dimensional vessel segmentation using a novel combinatory filter framework," *Physics in Medicine and Biology*, vol. 59, no. 22, pp. 7013–7029, 2014.

[170] C. Wilkinson, F. L. Ferris, R. E. Klein, P. P. Lee, C. D. Agardh, M. Davis, D. Dills, A. Kampik, R. Pararajasegaram, J. T. Verdaguer, *et al.*, "Proposed international clinical diabetic retinopathy and diabetic macular edema disease severity scales," *Ophthalmology*, vol. 110, no. 9, pp. 1677–1682, 2003.

[171] J. W. Baish and R. K. Jain, "Fractals and cancer," *Cancer research*, vol. 60, no. 14, pp. 3683–3688, 2000.

[172] T. T. Nguyen, J. J. Wang, and T. Y. Wong, "Retinal vascular changes in pre-diabetes and prehypertension new findings and their research and clinical implications," *Diabetes Care*, vol. 30, no. 10, pp. 2708–2715, 2007.

[173] K. Miyamoto, S. Khosrof, S.-E. Bursell, Y. Moromizato, L. P. Aiello, Y. Ogura, and A. P. Adamis, "Vascular endothelial growth factor (vegf)-induced retinal vascular permeability is mediated by intercellular adhesion molecule-1 (icam-1)," *The American journal of pathology*, vol. 156, no. 5, pp. 1733–1739, 2000.

[174] B. Scholkopf, K.-K. Sung, C. J. Burges, F. Girosi, P. Niyogi, T. Poggio, and V. Vapnik, "Comparing support vector machines with gaussian kernels to radial basis function classifiers," *IEEE Transactions on Signal Processing*, vol. 45, no. 11, pp. 2758–2765, 1997.

[175] T. Kauppi, V. Kalesnykiene, J.-K. Kamarainen, L. Lensu, I. Sorri, H. Uusitalo, H. Kälviäinen, and J. Pietilä, "Diaretdb0: Evaluation database and methodology for diabetic retinopathy algorithms," *Machine Vision and Pattern Recognition Research Group, Lappeenranta University of Technology, Finland*, 2006.

[176] M. U. Akram, A. Tariq, M. A. Anjum, and M. Y. Javed, "Automated detection of exudates in colored retinal images for diagnosis of diabetic retinopathy," *Applied optics*, vol. 51, no. 20, pp. 4858–4866, 2012.

[177] K. B. Franklin, G. Paxinos, *et al.*, *Mouse brain in stereotaxic coordinates*. Academic press, 1997.

[178] C. R. Tolle, T. R. McJunkin, and D. J. Gorsich, "An efficient implementation of the gliding box lacunarity algorithm," *Physica D: Nonlinear Phenomena*, vol. 237, no. 3, pp. 306–315, 2008.

[179] R. J. Zawadzki, A. R. Fuller, S. S. Choi, J. S. Werner, D. F. Wiley, and B. Hamann, "Adaptation of a support vector machine algorithm for segmentation and visualization of retinal structures in volumetric optical coherence tomography data sets," *Journal of Biomedical Optics*, vol. 12, no. 4, pp. 041206–041206, 2007.

[180] L. Parsonson and L. Bai, "Three dimensional angiogenesis modelling on the gpu," in *7th International Conference on BioMedical Engineering and Informatics*, 2014.

[181] M. Haghighat, S. Zonouz, and M. Abdel-Mottaleb, "Cloudid: Trustworthy cloud-based and cross-enterprise biometric identification," *Expert Systems with Applications*, vol. 42, no. 21, pp. 7905–7916, 2015.

[182] J. Zhang, *Detection and monitoring of wear using imaging methods*. University of Twente, 2006.